

UNCLASSIFIED

AD NUMBER
ADB004548
NEW LIMITATION CHANGE
TO Approved for public release, distribution unlimited
FROM Distribution authorized to U.S. Gov't. agencies only; Test and evaluation; Aug 1974. Other requests shall be referred to Air Force Materials Laboratory, Physics Division [AFML/LP], Wright-Patterson AFB, OH, 45433.
AUTHORITY
WL-DORT ltr, 12 Jul 1995

THIS PAGE IS UNCLASSIFIED

DISCLAIMER NOTICE



THIS DOCUMENT IS BEST QUALITY AVAILABLE. THE COPY FURNISHED TO DTIC CONTAINED A SIGNIFICANT NUMBER OF PAGES WHICH DO NOT REPRODUCE LEGIBLY.

L

AFML-TR-75-28

L

ADB004548

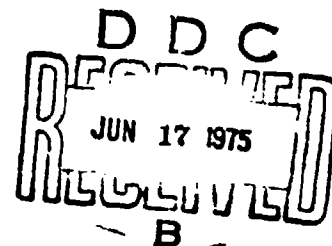
**THERMAL, ELECTRICAL AND PHYSICAL PROPERTY
MEASUREMENTS OF LASER WINDOW MATERIALS**

UNIVERSITY OF DAYTON
RESEARCH INSTITUTE
DAYTON, OHIO 45469

TECHNICAL REPORT AFML-TR-75-28

APRIL 1975

Distribution limited to U.S. Government agencies only; test and evaluation;
August 1974. Other requests for this document must be referred to the Air
Force Materials Laboratory, Physics Division (AFML/LP), Wright-Patterson
Air Force Base, Ohio 45433.



AIR FORCE MATERIALS LABORATORY
AIR FORCE SYSTEMS COMMAND
WRIGHT-PATTERSON AIR FORCE BASE, OHIO 45433

NOTICE

When Government drawings, specifications, or other data are used for any purpose other than in connection with a definitely related Government procurement operation, the United States Government hereby incurs no responsibility nor any obligation whatsoever; and the fact that the government may have formulated, furnished, or in any way supplied the said drawings, specifications, or other data, is not to be regarded by implication or otherwise as in any manner licensing the holder or any other person or corporation, or conveying any rights or permission to manufacture, use, or sell any patented invention that may in any way be related thereto.

UNCLASSIFIED

SECURITY CLASSIFICATION OF THIS PAGE (When Data Entered)

REPORT DOCUMENTATION PAGE		READ INSTRUCTIONS BEFORE COMPLETING FORM
1. REPORT NUMBER AFML-TR-75-28	2. GOVT ACCESSION NO.	3. RECIPIENT'S CATALOG NUMBER
4. TITLE (and Subtitle) THERMAL, ELECTRICAL, AND PHYSICAL MEASUREMENTS OF LASER WINDOW MATERIALS	5. TYPE OF REPORT & PERIOD COVERED Final Report (1972-1974)	
	6. PERFORMING ORG. REPORT NUMBER UDRI-TR-75-06	
7. AUTHOR(s) John C. Wurst and Thomas P. Graham	8. CONTRACT OR GRANT NUMBER(s) F33615-72-C-1257	
9. PERFORMING ORGANIZATION NAME AND ADDRESS University of Dayton Research Institute 300 College Park, Dayton, Ohio 45409	10. PROGRAM ELEMENT PROJECT, TASK AREA & WORK UNIT NUMBERS F33615-72-C-1257	
11. CONTROLLING OFFICE NAME AND ADDRESS ONRRR The Ohio State University Res. Center 1314 Kinnear Rd, Columbus, Ohio 43212	12. REPORT DATE April 1975	
	13. NUMBER OF PAGES 171	
14. MONITORING AGENCY NAME & ADDRESS (if different from Controlling Office) Air Force Materials Laboratory Air Force Systems Command Wright-Patterson Air Force Base, Ohio 45433	15. SECURITY CLASS. (of this report) Unclassified	
	15a. DECLASSIFICATION DOWNGRADING SCHEDULE	
16. DISTRIBUTION STATEMENT (of this Report): Distribution Limited to U.S. Government Agencies only; Test and Evaluation; August 1974. Other requests for this document must be referred to the Air Force Materials Laboratory, Physics Division (AFML/LP), Wright-Patterson Air Force Base, Ohio 45433.		
17. DISTRIBUTION STATEMENT (of the abstract entered in Block 20, if different from Report)		
18. SUPPLEMENTARY NOTES		
19. KEY WORDS (Continue on reverse side if necessary and identify by block number) laser windows KCl Weibull statistics chalcogenides KBr Thermal, electrical, mechanical, ZnSe NaCl microstructural CdTe Alkali halides Strength Fracture energy		
20. ABSTRACT (Continue on reverse side if necessary and identify by block number) <p>Various II-VI and alkali halide compounds were subjected to a comprehensive evaluation to determine their relative effectiveness in a CO₂ laser window application. All of the materials evaluated had the requisite infrared transparency and low absorptance; this program concentrated therefore on the thermal, electrical, mechanical, and physical properties which must be considered in the design of a practical window configuration</p>		

DD FORM 1473
1 JAN 73

EDITION OF 1 NOV 68 IS OBSOLETE

UNCLASSIFIED

SECURITY CLASSIFICATION OF THIS PAGE (When Data Entered)

UNCLASSIFIED

SECURITY CLASSIFICATION OF THIS PAGE (When Data Entered)

Primary emphasis was directed towards mechanical properties and more than 600 flexural test specimens were evaluated in the course of this 20-month effort.

Initially, research quantities of CdTe and ZnSe from several suppliers were evaluated. Eventually, the evaluation concentrated on ZnSe produced by Raytheon Corporation using chemical vapor deposition to obtain large flat plates (nominally 35 cm x 60 cm) of fine grained polycrystalline material.

Evaluation of the alkali halides KCl, KBr, NaCl, and their alloys was initiated midway through the program. KCl alloyed with KBr, RbCl or Eu^{+2} and hot forged to produce a fine-grained microstructure was the most promising of the alkali halides. Best results were obtained with alloys grown as single crystals by Harshaw and subsequently hot forged by Honeywell Corporation.


UNCLASSIFIED

SECURITY CLASSIFICATION OF THIS PAGE (When Data Entered)

FOREWORD

The work described herein was performed by the University of Dayton Research Institute under Contract F33615-72-C-1257, during the period from 1 February 1972 to 31 August 1974. Sgt. Charles L. Strecker AFML/LP, Wright-Patterson Air Force Base, Ohio 45433 was the Project Engineer. The University of Dayton internal report number is UDRI-TR-75-06.

This technical report has been reviewed and is approved.



William G. D. Frederick, Acting Chief
Laser and Optical Materials Branch
Electromagnetic Materials Division
Air Force Materials Laboratory

TABLE OF CONTENTS

	Page
1. INTRODUCTION	1
2. EXPERIMENTAL METHODS	5
2.1 Specimen Preparation and Pretest Inspection	5
2.2 Microstructural Analysis	6
2.3 Flexural Strength	7
2.4 Hardness	9
2.5 Ccoefficient of Thermal Expansion	9
2.6 Density	10
2.7 Specific Heat	10
2.8 Thermal Diffusivity-Thermal Conductivity	12
2.9 Electrical Properties	17
3. RESULTS	
3.1 II-VI Compounds	23
3.1.1 Raytheon ZnSe	23
3.1.1.1 Background	23
3.1.1.2 Microstructural Analysis	24
3.1.1.3 General Specimen Appearance	26
3.1.1.4 Thermal Properties	27
3.1.1.5 Electrical Resistivity	29
3.1.1.6 Flexural Strength	33
3.1.1.7 Weibull Analysis of Flexural Strength Data	46
3.1.1.8 Evaluation of Plate 61C	48
3.1.1.9 Proof and Fatigue Testing of ZnSe Bars ..	56
3.1.1.10 Static Fatigue	63
3.1.1.11 Fracture Toughness of ZnSe	64
3.1.1.12 Design of a Proof Test For ZnSe	69
3.1.2 Gould ZnSe	80
3.1.3 Coors ZnSe	84
3.1.4 Gould CdTe	87
3.1.5 Tyco CdTe	92
3.1.6 Hughes CdTe	95

v

PRECEDING PAGE BLANK NOT FILMED

TABLE OF CONTENTS (cont'd)

	Page
3. 1. 7 Grain Boundary Effects in CdTe	97
3. 1. 8 A Proposed Grain Boundary Model for CdTe	105
3. 1. 9 Summary of the II-VI Compounds	108
3. 1. 9. 1 ZnSe	108
3. 1. 9. 2 CdTe	110
3. 2 Alkali Halides	111
3. 2. 1 Honeywell Alkali Halides	111
3. 2. 1. 1 Potassium Chloride	112
3. 2. 1. 2 Honeywell Press Forged NaCl	136
3. 2. 1. 3 Honeywell Press Forged KBr	139
3. 2. 2 Harshaw Alkali Halides	141
3. 2. 3 ManLabs KCl and KCl Alloys	151
3. 2. 4 Hughes Alkali Halides	165
3. 2. 5 Isomet KCl	165
3. 2. 6 Summary	167

LIST OF ILLUSTRATIONS

Figure	Page
1 Four-Point Bend Test Fixture for Flexural Strength Measurements	8
2 Schematic Diagram of the Isothermal Drop Calorimeter	11
3 Schematic Diagram of the Thermal Diffusivity Facility ...	16
4 Thermal Properties of Armco Iron.....	18
5 Typical I-V Characteristic of an Electrical Resistivity-Hall Coefficient Specimen	20
6 Block Diagram of the Resistivity-Hall Coefficient Facility	20
7 Typical Polished Section and Scanning Electron Micrograph of Raytheon ZnSe.....	25
8 Typical Thermal Expansion Curve for Raytheon ZnSe	28
9 Thermal Properties of CVD ZnSe	30
10 Microstructure of ZnSe Before and After Annealing	31
11 Resistivity versus Reciprocal Temperature of Annealed and Unannealed ZnSe	32
12 Cumulative Failure Distribution of Flexural Strength for Raytheon ZnSe.....	34
13 Cumulative Failure Distribution of ZnSe Fitted with a Weibull Distribution	49
14 Test Specimen Layout	50
15 Cumulative Failure Distribution of ZnSe Proof Tested at 6800 psi	60
16 Cumulative Failure Distribution of ZnSe Proof Tested at 4000 psi	61
17 Flexural Strength of ZnSe as a Function of Critical Flaw Size	67

LIST OF ILLUSTRATIONS (cont'd)

Figure	Page
18 Cumulative Frequency Distribution of the Glass Flexural Test Bars	75
19 Reliability of Two-inch Glass Discs Subjected to Uniform Pressure Loading	75
20 Glass Sector After Test	76
21 Reliability of Large 60° Glass Sectors Subjected to Uniform Pressure Loading	77
22 Cumulative Frequency Distributions for ZnSe Flexural Test Bars	78
23 Reliability of Two-inch ZnSe Discs Subjected to Uniform Pressure Loading	79
24 Representative Microstructure of Gould PVD ZnSe	81
25 Electrical Resistivity of Gould ZnSe	83
26 Typical Polished Section and Scanning Electron Micrograph of Coors ZnSe Sample 105	86
27 Thermal Properties of Gould CdTe	90
28 Electrical Resistivity of Gould CdTe	91
29 Electrical Resistivity of Tyco CdTe	94
30 Electrical Resistivity of Hughes CdTe	95
31 Grain Boundary Resistance Measurements of a Tyco CdTe Bicrystal	98
32 Grain Boundary Resistance Measurements of Tyco 74 and Gould 44 CdTe Samples	99
33 Experiment Arrangement for Photoresponse Measurements of Polycrystalline CdTe	101
34 Photovoltage, Photocurrent, and Resistivity Measurements of a Tyco 75 CdTe Bicrystal	102

LIST OF ILLUSTRATIONS (cont'd)

Figure	Page
35 Photoresponse Scans of Polycrystalline Tyco 74 CdTe ...	104
36 Dislocation Model of a Grain Boundary (after Matari)	106
37 Energy Band Model of a Grain Boundary and its Equivalent Electrical Circuit (after Matari).....	106
38 Honeywell Hot Forged Unalloyed KCl	118
39 Discontinuous Grain Growth in Honeywell Hot Forging Unalloyed KCl	119
40 Honeywell Hot Forged KCl + 5 m/o KBr	120
41 Hot Forged KCl + 5 m/o RbCl.....	122
42 Honeywell Hot Forged KCl + 5 m/o RbCl	122
43 Honeywell Hot Forged KCl + 10 m/o RbCl	124
44 Honeywell Hot Forged KCl:500 ppm Eu^{+2}	125
45 Honeywell Hot Forged KCl + 1 m/o CsCl	125
46 Lattice Constants for Various KCl-RbCl Alloys	127
47 Thermal Properties of Honeywell Press Forged KCl Alloys and "Polytran" KCl	128
48 Cutting Diagram for KCl Alloy Homogeneity Analysis	131
49 Thermal Conductivity of KCl Alloys	135
50 Honeywell Hot Forged Unalloyed NaCl	138
51 Honeywell Hot Forged NaCl + 10 m/o NaBr.....	138
52 Honeywell Hot Forged KBr.....	140
53 Harshaw Hot Extruded KCl:Ba ⁺²	147
54 Harshaw Hot Extruded KCl:500 ppm Eu^{+2}	148
55 Harshaw Hot Extruded KCl:Sr ⁺²	149

LIST OF ILLUSTRATIONS (cont'd)

Figure		Page
56	Harshaw Hot Extruded KCl.....	150
57	ManLabs Hot Forged Unalloyed KCl	155
58	ManLabs Hot Forged KCl:500 ppm Eu^{+2}	157
59	ManLabs Hot Forged KCl:500 ppm Eu^{+2}	157
60	ManLabs Hot Forged KCl + 1 m/o CsCl	158
61	ManLabs Hot Forged KCl + 5 m/o KBr	158
62	ManLabs Hot Forged 10 m/o KBr	159
63	ManLabs Hot Forged 5 m/o RbCl.....	160
64	ManLabs Hot Forged 5 m/o RbCl.....	160
65	ManLabs Hot Forged "Alqloy"	161
66	Representative Microstructure of ManLabs Hot Forged KCl.....	164
67	Representative Microstructure of Hughes Polycrystalline KCl and NaCl	166

LIST OF TABLES

Table	Page
1 Summary of Mean Grain Size Measurements of Raytheon ZnSe	24
2 Results of Flexural Strength Measurement of Raytheon ZnSe	35
3 Experimental Layout of Homogeneity Evaluation	51
4 Summary of Mean Grain Size Measurements of Plate 61C	53
5 Results of Loading Rate, Temperature and Orientation Evaluation	55
6 Summary of Proof Tested ZnSe	58
7 Fatigue Test Results for Raytheon ZnSe (Plate 61C)	62
8 Static Fatigue Tests of ZnSe	63
9 Results of Fracture Toughness Measurements of Raytheon ZnSe	66
10 Effective Grain Size for Twin Boundary Initiated Brittle Fracture in ZnSe	68
11 Summary of Test Results for Gould ZnSe	82
12 Summary of Test Results for Coors ZnSe	85
14 Summary of Property Measurements of TYCO CdTe	93
15 Summary of Property Measurements of Hughes CdTe	96
16 Test Results for Honeywell Press Forged KCl	114
17 Summary of X-ray Diffraction Studies of Honeywell KCl Alloys	127
18 Coefficient of Thermal Expansion of Honeywell KCl and KCl Alloys	130

LIST OF TABLES (cont'd)

Table		Page
19	Summary of X-ray Diffraction Studies of Single Crystal KCl Alloy Ingots	132
20	Computed Alloy Contents of Single Crystal KCl Alloy Ingots	133
21	Thermal Property Variations in the Single Crystal KCl Alloy Ingots at 250°C	135
22	Test Results for Honeywell Press Forged NaCl	137
23	Test Results for Honeywell Press Forged KBr	140
24	Test Results for Harshaw Single and Polycrystalline KCl	142
25	Test Results for ManLabs KCl.....	152
26	Test Results for ManLabs KCl Press Forged Disc	163
27	Coefficient of Thermal Expansion of Various ManLabs KCl Alloys.....	163
28	Test Results for Hughes Alkali Halides	166
29	Highest Strengths Observed for Each Alkali Halide Composition Evaluated.....	170
30	Petch Constants for the Alkali Halides.....	171

SUMMARY

Various II-VI and alkali halide compounds were subjected to a comprehensive evaluation to determine their relative effectiveness in a CO₂ laser window application. All of the materials evaluated had the requisite infrared transparency and low absorptance; this program concentrated therefore on the thermal, electrical, mechanical, and physical properties which must be considered in the design of a practical window configuration.

Primary emphasis was directed towards mechanical properties and more than 600 flexural test specimens were evaluated in the course of this 20-month effort.

Initially, research quantities of CdTe and ZnSe from several suppliers were evaluated. Eventually, the evaluation concentrated on ZnSe produced by Raytheon Corporation using chemical vapor deposition to obtain large flat plates (nominally 35 cm x 60 cm) of fine grained polycrystalline material.

Evaluation of the alkali halides KCl, KBr, NaCl, and their alloys was initiated midway through the program. KCl alloyed with KBr, RbCl or Eu⁺² and hot forged to produce a fine-grained microstructure was the most promising of the alkali halides. Best results were obtained with alloys grown as single crystals by Harshaw and subsequently hot forged by Honeywell Corporation.

Property data for the II-VI and alkali halide compounds are summarized in Tables I and II. The flexural strength data presented in these tabulations represent the largest observed values. Frequently, lower strengths were obtained due to processing flaws associated with specimen preparation. The reported strengths, therefore, represent achievable rather than typical levels. The other property values listed in the tables are those which can be routinely expected for a given composition.

II-VI COMPOUND

Comparisons between ZnSe (these data are primarily for CVD material) and the composite properties of CdTe produced by three different processes reveal that ZnSe has three times the thermal conductivity, nearly twice the coefficient of linear expansion, and twice the elastic stiffness of CdTe. None of the three CdTe fabrication processes produced fine-grained material. Consequently, CdTe was much softer and weaker than the CVD ZnSe.

Low free carrier concentrations as evidenced by large values of electrical resistivity are essential for low-loss infrared transmittance. Various dopants such as Ga and In were employed in conjunction with special heat treatment in an attempt to obtain high-resistivity n-type semi-conducting CdTe. The dopant additions and heat treatments were not always successful and a wide range of resistivity values were obtained for CdTe. In contrast, electrical resistivity values for ZnSe were consistently very large, especially with the CVD material.

Evaluations of a large CVD ZnSe plate and of specimens from several different production runs revealed that the CVD process could produce homogeneous material with reproducible properties from run-to-run.

A sensitivity to environmentally assisted slow crack growth was observed with ZnSe during experiments associated with the design of a proof test for full scale ZnSe hardware. It was not established that slow crack growth presents a definite hazard in the stress-time regime of laser window applications. However, the existence of this environmental sensitivity would indicate the advisability of minimizing the exposure of ZnSe components to heavy loads in moist atmospheres.

ALKALI HALIDES

Alloying additions in combination with thermo-mechanical deformation to induce the formation of a fine-grained microstructure produced significant strengthening of the alkali halides.

The strongest of the KCl alloys were those containing 500 ppm Eu^{+2} , 5 and 10 m/o RbCl, and 5 and 10 m/o KBr. While the alloying addition had no measurable effect on the coefficient of thermal expansion of KCl, a two-fold decrease of thermal conductivity was observed with 5 m/o additions of either RbCl or KBr. Increasing the RbCl or KBr content to 10 m/o lowered the thermal conductivity even further but did not produce additional strengthening. In contrast, a 500 ppm addition of Eu^{+2} was the most effective strengthening addition and there was no measurable decrease of thermal conductivity.

To a lesser extent, a 1 m/o CsCl had a strengthening effect. Alloy, a 33 KCl - 67 KBr alloy, on an equivalent grain size basis was stronger than unalloyed KCl or KBr.

Unalloyed NaCl was quite strong and appeared to be strengthened with the addition of 10 m/o NaBr. However, a direct comparison of strength was not possible because of microstructural differences between the two materials.

TABLE I. SUMMARY OF II-VI COMPOUND PROPERTIES

	ZnSe	CdTe
Specific Heat (cal/gm°C)		
-50°C	0.074	0.048
25°C	0.084	0.054
65°C	0.092	0.057
Thermal Diffusivity (cm ² /sec)		
-50°C	0.137	0.070
25°C	0.100	0.045
65°C	0.072	0.040
Thermal Conductivity (w/cm°C)		
-50°C	0.22	0.082
25°C	0.18	0.062
65°C	0.15	0.056
Coefficient of Thermal Expansion (10 ⁻⁶ /°C)	8.0	4.5
Electrical Resistivity (ohm-cm)		
-50°C	>10 ¹²	6x10 ² -2x10 ⁴
25°C	5x10 ¹⁰ -4x10 ¹²	3x10 ² -2x10 ⁵
65°C	3x10 ¹⁰ -1x10 ¹¹	2x10 ² -5x10 ⁴
Flexural Strength (ksi)		
range	4.0-5.6	2.0-4.7
average	6.7	3.5
Young's Modulus (psi x 10 ⁶)		
-50°C	10.8	--
25°C	10.0	5.4
65°C	9.7	--
Poisson's Ratio (-50°C to +65°C)	0.30	--
Stress Intensity Factor, K _I , (psi√in)	600-1300	--
Fracture Energy (J/m ²)	3-6	--
Density (gm/cc)	5.26	5.86
Knoop Hardness, 200 gm load, (kg/mm ²)	125	65
Mean Grain Size (μm)	50	500-3000

TABLE II. SUMMARY OF ALKALI HALIDE PROPERTIES

	Unalloyed KCl	KCl:100 Ppm Eu ²⁺	KCl:5 m/o		KCl:10 m/o		KCl:5 m/o		KCl:10 m/o		KCl:1 m/o		Alloy 67 KBr		33 KCl		Unalloyed		NaCl:10 m/o	
			RbCl	KBr	RbCl	KBr	RbCl	KBr	RbCl	KBr	CsCl	KBr	KBr	KBr	KBr	KBr	NaCl	NaCl	NaBr	NaBr
Specific Heat (cal/cm ³ °C)																				
-50°C	0.138	0.140	0.140	0.140	---	0.140	---	0.140	---	---	---	---	---	---	---	---	---	---	---	---
25°C	0.154	0.150	0.150	0.150	0.155	0.150	---	0.150	0.140	---	---	---	---	---	---	---	---	---	---	---
65°C	0.160	0.160	0.160	0.160	---	0.160	---	0.160	---	---	---	---	---	---	---	---	---	---	---	---
Thermal Diffusivity (cm ² /sec)																				
-50°C	0.044	0.065	0.029	---	---	0.026	---	0.026	---	---	---	---	---	---	---	---	---	---	---	---
25°C	0.040	0.040	0.020	0.016	---	0.018	---	0.018	0.014	---	---	---	---	---	---	---	---	---	---	---
65°C	0.033	0.033	0.017	---	---	0.015	---	0.015	---	---	---	---	---	---	---	---	---	---	---	---
Thermal Conductivity (w/cm °C)																				
-50°C	0.077	0.077	0.038	---	---	0.031	---	0.031	---	---	---	---	---	---	---	---	---	---	---	---
25°C	0.054	0.054	0.029	0.021	---	0.024	---	0.024	0.019	---	---	---	---	---	---	---	---	---	---	---
65°C	0.047	0.047	0.020	---	---	0.022	---	0.022	---	---	---	---	---	---	---	---	---	---	---	---
Coefficient of Thermal Expansion (10 ⁻⁶ /°C)	36	34-35	35	35	35	35	---	35	---	---	---	---	---	---	---	---	---	---	---	---
Flexural Strength (ksi)																				
Yield	4.7	4.0	5.8	5.9	5.9	5.5	---	5.5	5.3	---	4.3	4.5	3.2	4.6	5.1	---	---	---	---	---
Ultimate	6.6	10.3	7.7	7.2	7.2	7.3	---	7.3	7.3	---	5.4	5.3	4.6	10.2	6.0	---	---	---	---	---
Knoop Hardness (100 gm load/kg/mm ²)	13-26	15-19	16-26	18-29	18-29	18-26	---	18-26	16-23	---	16-19	22	9-13	22-35	36	---	---	---	---	---
Mean Grain Size (μm)	4	4	7	8	8	7	---	7	10	---	11	27	10	7	48	---	---	---	---	---

1. INTRODUCTION

With the development of high energy CO_2 gas lasers, the requirement for solid transparent barrier windows providing physical separation of the lasing gas and/or optical components from their external environments has emerged. To realize the inherent high power capacity of a gas laser, the window must transmit the laser beam with a minimum of energy absorption, otherwise, beam quality will be compromised by thermal lensing or, in extreme cases, the window itself will be destroyed by thermally induced fracture or decomposition.

High energy transparency requires low intrinsic absorption in a material which is free of scattering centers (as free carriers (electrons and holes), pores, cracks, precipitates, localized strain regions, and chemical inhomogeneities. However, purity, microstructural perfection, and homogeneity are not the only requirements which must be satisfied to qualify a material for laser window applications. The windows must be sufficiently strong to withstand mechanical loading of both a static and cyclic nature. Impact resistance and environmental durability are also essential for satisfactory component performance in field service.

The leading candidates for CO_2 laser windows are the II-VI compounds (ZnSe and CdTe) and the alkali halides (KCl, NaCl, and their alloys). All of these materials will require antireflection coatings with sufficient hardness to also impart a measure of scratch and abrasion resistance to the window surfaces. In the case of the alkali halides, the antireflection coating must also serve as a moisture barrier.

The alkali halides exhibit a limited capacity for plastic deformation at room temperature but experience a ductile-to-brittle transition at somewhat lower temperatures. The other candidate materials for CO_2 laser windows are brittle over the entire range of anticipated use temperatures.

The useful strength of a brittle material is controlled by the presence of surface and volume distributed flaws which, when stressed to their limit, extend in a catastrophic fashion. Since the number and severity of flaws varies with specimen size in a statistical fashion, it follows that the strength of a brittle material will diminish with increasing specimen size and will also exhibit a statistical variation.

Proper evaluation of a brittle material must recognize and account for the statistical character of its strength. If guaranteed levels of strength are required with full-size components, proof-testing must be incorporated as part of the component certification. Therefore, maximum utility can be realized from laboratory strength test data for brittle laser window candidates only if these data are generated in statistical quantities and are treated with analyses which ultimately identify suitable proof stress levels for full-size components.

Optical performance and mechanical strength are not the only factors to be considered in selecting a window material. All real materials will absorb a certain amount of infrared radiation which can generate thermal gradients within the material. These thermal gradients will be realized both as sensible heating and as a buildup of stored elastic energy. Microcracking or even catastrophic fracture can result.

Materials with low values of thermal expansion and Young's modulus and large values of fracture strength, thermal diffusivity, and fracture toughness will exhibit good thermal shock resistance. A comprehensive window materials evaluation program should, therefore, include the measurement of these properties.

Thermal runaway, a catastrophic rise of window temperature resulting from energy being absorbed faster than it can be dissipated, is another mechanism of window failure. This can occur if the thermal conductivity (or thermal diffusivity) of the material decreases with temperature or if the absorption increases with temperature. The latter phenomenon is more

prevalent in the semiconductor class of window materials where energy is absorbed by thermally generated free carriers, and an avalanche effect leading to thermal failure can thereby be initiated.

Electrical resistivity and Hall coefficient measurements over a range of temperatures provide an excellent means of characterizing defects, free carriers, and impurity states which could contribute to energy absorption.

Microstructural defects such as inclusions, pores, chemical inhomogeneities, and microcracks can act as radiation scattering sites and increase the amount of absorbed energy. Scanning electron microscopy and conventional optical microscopy (including differential interferometry) are invaluable in characterizing such potentially limiting microstructural defects. Other properties such as hardness, bulk density, melting point, water solubility, and fatigue resistance may play a role in the selection of a material and should be part of an overall characterization plan.

Finally, the successful transition from laboratory sized test specimens to full-scale components must be carefully evaluated in terms of the materials supplier's ability to retain the quality, homogeneity, and reproducibility of a product when it is scaled-up in size.

The objective of the program described herein was to perform thermal, electrical, mechanical, microstructural, and physical characterization of materials with potential for high energy infrared laser window applications. The evaluation procedures, for the most part, were well-defined techniques, thereby assuring rapid processing of samples and a quick response to the Air Force Materials Laboratory information needs.

The bulk property determinations which constituted the basic evaluation were: flexural strength, Young's modulus, Poisson's ratio, fracture toughness, low cycle fatigue, static fatigue, hardness, thermal diffusivity, thermal conductivity, heat capacity, coefficient of thermal expansion, electrical resistivity, Hall coefficient, density, and microstructural characteristics.

The measurement procedures were designed to accommodate research quantities of material. Not all of the material submitted for evaluation was subjected to the entire array of property measurements. Frequently, testing was discontinued when it became apparent that a material had failed to satisfy one or more minimum performance specifications.

Initially, this effort centered on the evaluation of CdTe produced by physical vapor deposition, sonic casting, and a modified Bridgeman process. ZnSe fabricated by hot pressing, chemical vapor deposition, and physical vapor deposition were also evaluated in the early stages of this program. Chemical vapor deposited ZnSe emerged from these studies as a superior material-process combination and emphasis shifted to a more comprehensive evaluation of this material with respect to process variability and scale-up homogeneity.

Alkali halide materials were not evaluated to a large extent until midway through the program. Single crystal and polycrystalline samples of KCl, NaCl, and KBr were tested as were numerous alloys of these compounds.

The test results indicated that the strength of alkali halides could be improved by hot working processes which form a fine-grained polycrystalline microstructure. Further improvements could be realized through alloying additions.

2. EXPERIMENTAL METHODS

2.1 SPECIMEN PREPARATION AND PRETEST INSPECTION

The majority of the materials evaluated in this program were provided by the Air Force Materials Laboratory in the form of mechanical test bars, usually ground and polished by the material producer to a relatively flawless condition.

In a few instances, test bars were cut from bulk material by University of Dayton Research Institute (UDRI) personnel. A wire saw^{*} equipped with a 30 μm diameter diamond impregnated cutting wire was employed in the preparation of these specimens. Water was used as a cutting lubricant in the machining of CdTe and ZnSe; the alkali halide specimens were lubricated with fresh mineral spirits.

The saw-cut surfaces of the test bars were then hand-polished to a smooth, scratch-free condition. All sharp edges and corners were rounded and polished to remove chips and scratches. The CdTe and ZnSe were satisfactorily polished with either 0.3 μm Al_2O_3 or 1.0 μm diamond paste. However, Al_2O_3 abrasives tended to gouge and imbed in the relatively soft CdTe and ZnSe and best results were obtained with diamond polishing media. The alkali halides were satisfactorily polished with methanol moistened jewelers' rouge.

The prepared test specimens were stored in individual soft wrapping to prevent accidental contact damage during normal handling prior to test. The alkali halide specimens were stored in vacuum desiccators prior to testing, thereby minimizing their exposure to the 50% relative humidity of the laboratory.

* Laser Technology, Inc., Wire Saw Model 200 GM, Los Angeles, Calif.

Ordinarily, the "as received" condition of the specimens was evaluated by microscopic inspection at 10 to 50X magnification. Inspections of the alkali halide specimens were conducted in a nitrogen filled dry box maintained at 35% relative humidity.

2.2 MICROSTRUCTURAL ANALYSIS

The microstructural characteristics of the test specimens, especially those which were polycrystalline, were routinely evaluated from examination of optical polished sections and by scanning electron microscopy of fracture surfaces. As required, electron microprobe analysis was conducted on specimens believed to contain major impurity phases or large deviations from stoichiometry.

Both CdTe and ZnSe required special care to obtain smooth scratch-free polished surfaces. Specimens of either compound were mounted in lucite and ground flat on 4-0 SiC paper. This was followed by a rough polish with $1.0\text{ }\mu\text{m Al}_2\text{O}_3$ and then with $0.3\text{ }\mu\text{m Al}_2\text{O}_3$ on silk cloth. Final polishing to a scratch-free condition was accomplished with $0.05\text{ }\mu\text{m Al}_2\text{O}_3$ on microcloth using an automatic vibratory polisher.

The ZnSe specimens were etched for 90 seconds at room temperature in a mixture of 200 gms chromic acid, 15 gms of Na_2SO_4 , 50 ml of HNO_3 , and 900 ml of H_2O . The CdTe specimens were first chemically polished for 90 seconds in a room temperature mixture of 10 ml HNO_3 , 20 ml H_2O , and 4 gms of $\text{K}_2\text{Cr}_2\text{O}_7$ and then etched at room temperature for 20-30 seconds in a mixture of 150 gms chromic acid, 4 gms H_2SO_4 and 1000 ml of H_2O .

The alkali halides were ground flat on 4-0 SiC paper; rough polished on red felt with a slurry of jewelers' rouge and methanol; and, then final polished on microcloth dampened with a mixture of jewelers' rouge and methanol. The polished samples were etched at room temperature for approximately three seconds in a very dilute aqueous solution of NaOH.

The lineal intercept technique was employed to evaluate the mean grain size of the polycrystalline samples evaluated. This procedure involved the random placement of a transparent overlay containing test lines of known length over a photomicrograph of a polished and etched section. By counting the number of intercepts between the test lines and grain boundaries, the mean grain size was determined from

$$\bar{D} = 1.56 \frac{C}{MN} \quad (1)$$

where \bar{D} is the mean grain size; C is the length of test line employed, M is the magnification of the photomicrograph; and N is the number of intercepts.

The underlying assumptions in the derivation of Equation (1) should restrict its use to the analysis of equiaxed, single phase microstructures. However, even with highly oriented microstructures, the equivalent equiaxed grain size values are useful for comparative purposes.

Scanning electron microscopy samples were usually prepared from the remains of mechanical test bars by coating the surface of interest with a thin layer of Au-Pd to prevent an image distorting charge buildup on the specimen surface. The SEM is equipped with an energy dispersive x-ray analyzer for evaluation of gross compositional inhomogeneities and to detect the presence of multiple phases.

Electron microprobe samples were prepared as polished sections; usually unetched to avoid unintentional removal of phases by preferential chemical attack. A thin layer of carbon was evaporated on the samples to eliminate surface charging.

2.3 FLEXURAL STRENGTH

Flexural strength was evaluated by testing prismatic beam specimens in four-point bending using special kinematically designed fixtures to minimize errors arising from misalignment, friction effects, specimen twist and taper, and contact point wedging.

Two test fixtures were employed in these evaluations. The smaller of the two, shown in Figure 1, accommodated specimens 2.5 cm long and 0.6 cm wide and was used in the majority of the CdTe and alkali halide strength measurements. Larger specimens, primarily those of ZnSe, were tested using a similar, but larger, fixture designed for bars up to 7.5 cm in length.

A universal testing machine was employed to load specimens at a rate which produced a failure in no less than two minutes. An LVDT deflectometer was used in conjunction with these measurements to obtain the center-point specimen deflection as a function of applied load. The yield point of the flexural test specimens was defined as the applied stress associated with the deviation from linear elastic response at zero off-set.

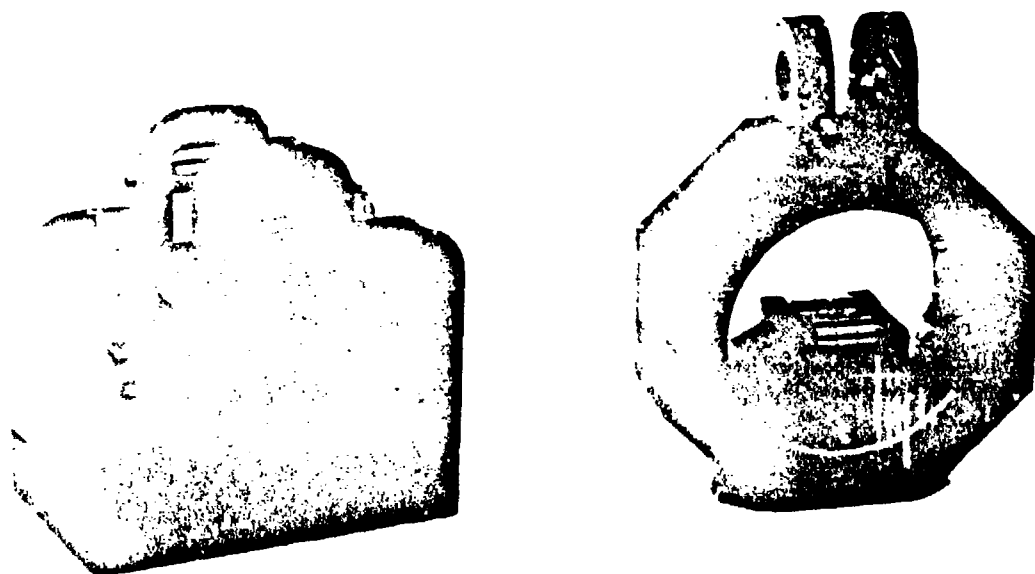


Figure 1. Four-Point Bend Test Fixture for Flexural Strength Measurements.

• Because of potential deleterious effects from handling and prolonged exposure to the laboratory environment (relative humidity of 50%), the alkali halide specimens were kept in sealed plastic envelopes until just prior to testing. White-glove handling procedures were followed and physical contact with the gage section of the specimens was avoided.

Mild cracking and slight plastic deformation of the specimens under the load points provided visible reference points for locating the fracture origin with respect to the imposed bending moment. Only those failures which occurred well within the inner load points were accepted as valid tests.

2.4 HARDNESS

Room temperature Knoop hardness measurements were routinely performed on all specimens at loads ranging from 50 to 200 gms. A minimum of five measurements were taken at each load.

2.5 COEFFICIENT OF THERMAL EXPANSION

A quartz-tube dilatometer was employed for thermal expansion measurements over the temperature range from -40° to $+100^{\circ}\text{C}$. A prismatic bar-shaped specimen ($0.3 \times 0.3 \times 2.5$ cm) was supported in a quartz tray with quartz push rods lightly spring-loaded against its ends. Thermal expansion of the specimen was translated through the push rods and detected by an LVDT unit. Specimen temperature and displacement were simultaneously plotted on an x-y recorder.

Low temperature measurements were performed by cooling the specimen to -40°C in an insulated liquid nitrogen chamber and then allowing the system to warm to room temperature at a rate controlled by an electric resistance heater. Elevated temperature measurements were accomplished by slowly heating the specimen-push rod assembly with a wire-wound tube furnace.

2.6 DENSITY

The Archimedes method of liquid immersion was used to make bulk density measurements. Water or a nonreactive liquid with a well-defined specific gravity was used as the immersion medium. An analytical balance was used in this measurement to obtain accuracies of better than $\pm 2\%$.

2.7 SPECIFIC HEAT

Isothermal drop calorimetry was employed for specific heat measurements at a reference temperature of 10°C . This is a relatively simple procedure in which a sample is equilibrated at a specified temperature and then transferred adiabatically to a receiver at a different temperature. A measure of the heat content of the sample is then obtained as a function of the corresponding temperature change of the receiver as it comes to thermal equilibrium with the sample.

For initial temperature differences between the sample and the receiver on the order of 20°C , the heat capacity at constant pressure can be obtained to a good approximation from

$$C_p \doteq \frac{\Delta H}{m\Delta T} \quad (2)$$

where ΔH is the thermal energy exchanged with the receiver, m is the mass of the sample, and ΔT is the initial temperature difference between the sample and receiver.

A schematic diagram of the drop calorimeter is shown in Figure 2. A 90 gm copper cup serves as the sample receiver. This cup is housed in a brass container and is surrounded with rigid foam insulation to thermally isolate it and to eliminate convective cooling currents within the brass container. The brass container is immersed in an isothermal bath. A tube, thermally isolated from the brass container by a phenolic-nylon spacer, is located directly over the receiver cup and contains an aluminum specimen platform.

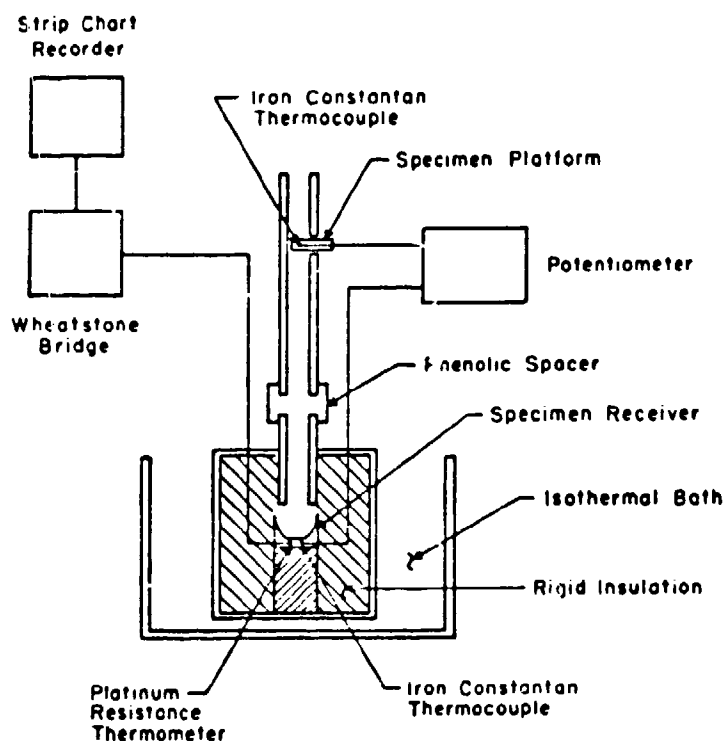


Figure 2. Schematic Diagram of the Isothermal Drop Calorimeter.

The measurement procedure is quite simple. The specimen is placed on the aluminum platform, the receiver assembly is immersed in the isothermal bath and the system is brought to thermal equilibrium. When a stable condition is reached, the sample is dropped into the receiver cup and the subsequent temperature change of the receiver measured. The receiver cup has been calibrated with standards of known specific heat to obtain a relationship between the receiver cup temperature and its heat content.

The initial temperature difference between the sample and receiver is measured with a pair of iron-constantan thermocouples located in the specimen platform and in the receiver. The receiver also contains a precision platinum resistance thermometer for measurement of the thermal energy exchange between the sample and the receiver.

A wheatstone bridge circuit with the platinum thermometer as one leg of the bridge is employed in conjunction with a constant current power supply to obtain a stable and reproducible output signal which is proportional to the receiver temperature. The bridge output signal is recorded as a function of time with a strip chart recorder.

The attainment of near thermal equilibrium is rather rapid and as many as six measurements have been taken in a single eight-hour working day. It is not necessary to establish and maintain absolutely perfect thermal equilibrium prior to each test as there are several techniques for treating raw calorimetry data to account for the influence on nonadiabatic conditions. The precision of the data obtained with the apparatus has been quite satisfactory. Consecutive measurements with a given sample will be consistently reproduced to within $\pm 3\%$.

2.8 THERMAL DIFFUSIVITY-THERMAL CONDUCTIVITY

Thermal diffusivity was measured by the so-called flash technique developed by Parker and co-workers.⁽¹⁾ A value of thermal diffusivity is obtained as a function of the transit time of a short duration (essentially instantaneous) heat pulse through a slab-shaped specimen. In contrast to the more cumbersome methods of steady state measurements, the flash method is relatively insensitive to specimen geometry and heat source characteristics and does not require elaborate instrumentation. The method is applicable over a wide range of temperatures and the data reduction is trivial.

The working equation for the flash method is

$$\alpha = \frac{k}{\rho C} = \frac{0.139l^2}{t_{1/2}} \quad (3)$$

(1) W. J. Parker, et al., "Flash Method of Determining Thermal Diffusivity, Heat Capacity, and Thermal Conductivity," J. Appl. Phys., 32 (9) 1679-1687 (1961).

where k is thermal conductivity, ρ is density, C is specific heat, l is the sample thickness, and $t_{1/2}$ is the time required for the back surface of the sample to reach half of its maximum value.

Equation (3) was derived from the one-dimensional heat flow equation for temperature, T , in an insulated solid of thickness, l , defined by Carslaw and Jaeger⁽²⁾ as

$$T_{(x,t)} = \frac{1}{l} \int_0^l T_{(x,0)} dx + \frac{2}{l} \sum_{n=1}^{\infty} \exp\left(\frac{-n^2 \pi^2 \alpha t}{l^2}\right) \cdot x \cos \frac{n\pi x}{l} \int_0^l T_{(x,0)} \cos \frac{n\pi x}{l} dx \quad (4)$$

Applying the conditions that a heat pulse Q is absorbed uniformly to a depth g on the surface of an opaque insulated solid of uniform thickness where the time of heat pulse deposition is small compared to the transit time of the pulse, Equation (4) can be solved for the following boundary conditions:

$$T_{(x,0)} = \frac{Q}{\rho C g} \quad \text{for } 0 < x < g \quad (5)$$

$$T_{(x,0)} = 0 \quad \text{for } g < x < l \quad (6)$$

For $g \ll l$ and $x = l$ (at the back surface of the specimen), this solution is given by:

$$\frac{T(l,t)}{T_{\max}} = 1 + 2 \sum_{n=1}^{\infty} (-1)^n \exp\left(\frac{-n^2 \pi^2 \alpha t}{l^2}\right) \quad (7)$$

(2) W. S. Carslaw and J. C. Jaeger, Condition of Heat in Solids, 2nd Edition, Oxford Press, New York, N. Y., 1959.

The solution of Equation (7) for $T_{(t,t)}/T_{\max} = 1/2$ yields Equation (3). Implied in this derivation are the assumptions that radiative losses are negligible and that the temperature excursion produced by the heat pulse is sufficiently small that the thermal diffusivity and specific heat of the sample remain constant.

Under certain conditions, the assumptions that the heat pulse deposition is essentially instantaneous and the heat losses from the sample are negligible are inapplicable. Heckman⁽³⁾ has addressed the problem of finite pulse time and heat loss effects. This analysis resulted in a very useful set of tables which, in conjunction with measured values of the heat source pulse width and an evaluation of the experimentally measured temperature response of a test specimen, can be employed to adjust Equation (3) to account for these deviations from ideality.

The specific heat of a sample can be obtained simultaneously with the measurement of thermal diffusivity from the relationship

$$C = \frac{Q}{\rho l \Delta T_m} \quad (8)$$

where Q is the input heat flux and ΔT_m is the peak temperature rise. The value of the input heat flux is an elusive parameter dependent not only upon the operating characteristics of the pulse source but also upon the size of the specimen, its surface emittance, and its proximity to the heat source. If the output of the heat source is reproducible, a value of the input heat flux can be obtained for given experimental configuration by independently measuring the specific heat at a known temperature and inserting this value in Equation (8) along with an experimental measurement of ΔT_m obtained with the thermal diffusivity apparatus at the same reference temperature.

(3) R. C. Heckman, "Finite Pulse-Time and Heat-Loss Effects in Pulse Thermal Diffusivity Measurements," J. Appl. Phys. 44 (4) 1455-1460 (1973).

A schematic diagram of the thermal diffusivity facility is shown in Figure 5. The heat pulse source consists of the power supply and Xenon flash tube from a ruby rod laser system.^{*} The laser rod was replaced with a 2.0 cm diameter quartz rod which serves as a light pipe for transferring energy from the Xenon flash discharge to the sample. The samples are mounted in a spring-loaded fixture which is thermally insulated to minimize heat losses. The back surface temperature response of the samples is sensed with an open junction chromel constantan contact thermocouple. With this arrangement, the electrical circuit of the thermocouple is completed through the sample itself; an arrangement which has low thermal mass and exceptional response time. The output of this thermocouple is employed both for steady state sample temperature measurements and for dynamic measurements in response to the heat pulse input. The dynamic signal is amplified and displayed on a monitor oscilloscope and channeled to a waveform recorder. The waveform recorder^{**} is a solid state electronic device which provides digital storage of high speed transient electrical signals for subsequent playback at a rate compatible with the writing speed of a conventional x-time recorder. A photodiode device activated by radiation from the light pipe provides a means for triggering the sweep mode of the monitor oscilloscope and for marking the initiation of the heat pulse on the waveform recorder trace.

The facility is equipped with a cooling chamber and a furnace for measurements over the temperature range of -65° to $+500^{\circ}\text{C}$. Low temperature data are obtained by first cooling the test specimen with a flow of liquid nitrogen cooled gaseous nitrogen. The cooled specimen is then allowed to warm slowly to room temperature at a rate regulated by the flow of nitrogen through the cooling chamber. Data are taken at periodic temperature intervals as the specimen warms.

^{*} Trion Instruments, Inc., Model LS1.

^{**} Transient Recorder Model 802, Biomation, Cupertino, Calif.

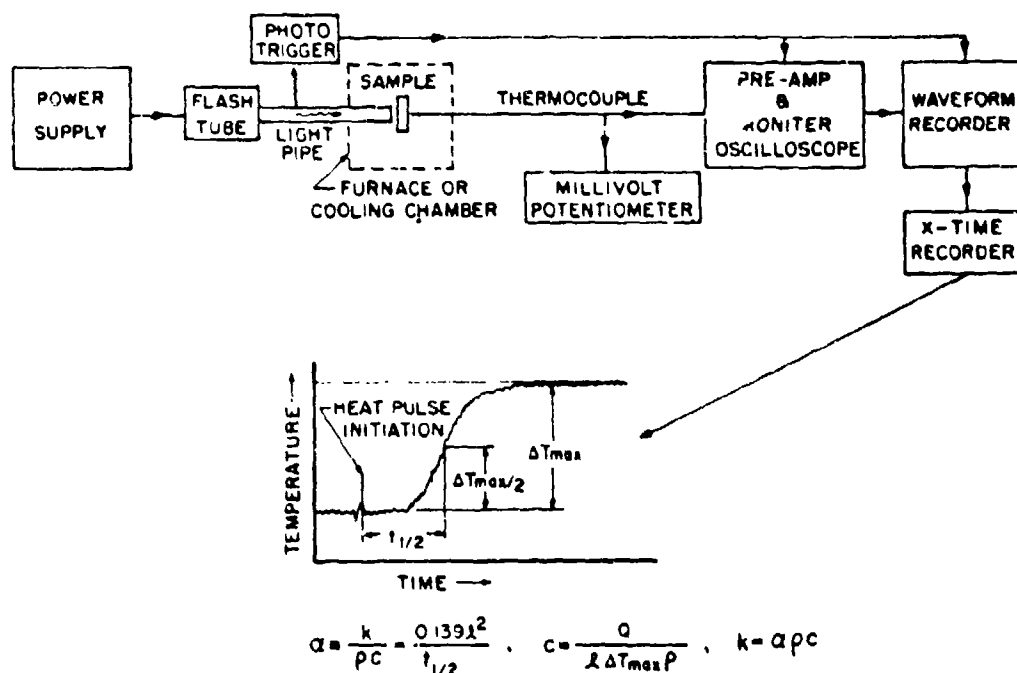


Figure 3. Schematic Diagram of the Thermal Diffusivity Facility.

Elevated temperature data are obtained in a similar fashion, i. e., the specimen is heated to a predetermined temperature in a wire-wound resistance furnace and then allowed to cool slowly while thermal diffusivity measurements are being taken. Generally, several room temperature measurements are made prior to heating or cooling the sample.

With high resistivity materials such as the alkali halides and the II-VI compounds, a thin silver film is vacuum deposited on the back surface of the sample to provide a conductive path for the open-junction thermocouple. Since this coating is very thin, is in intimate contact with the sample, and is a high thermal diffusivity material, its presence has no measurable influence on the heat pulse transit time.

The transparency of these laser window materials to the Xenon flash tube radiation required a thin, opaque front surface coating to prevent

radiative coupling between the heat pulse source and the back surface thermocouple. Several different types of coating, including flat-black lacquer, vacuum evaporated silver, colloidal graphite (aqueous suspension), and dry film-graphite lubricant were evaluated for this purpose. The best pinhole-free thin films were obtained with dry film graphite lubricant.*

As part of the overall calibration and evaluation of this test technique, thermal diffusivity and specific heat data were obtained for Armco iron over the temperature range of -65° to 220°C . These data are summarized in Figure 4 and are in excellent agreement with those compiled by TPRC.⁽⁴⁾ The maximum difference between the two sets of thermal diffusivity and specific heat data was less than 5%. Similar agreement was obtained with thermal conductivity values derived from graphically smoothed values of $t_{1/2}$ and ΔT_m .

2.9 ELECTRICAL PROPERTIES

Electrical resistivity and Hall coefficient measurements were conducted on CdTe and ZnSe materials over the temperature range of 4.2° to 420°K .

All of the specimens involved in these electrical property measurements were chemically treated to remove any surface impurities and mechanical damage which could introduce surface conduction effects or result in non-ohmic contacts. The treatment of CdTe followed the procedure of Lorentz, et al.⁽⁵⁾ and consisted of degreasing with acetone or trichloroethylene and etching in a mixture of $\text{HF}:\text{HNO}_3:2\text{H}_2\text{O}$, followed by immersion in a 50% solution of boiling NaOH. The specimens were then washed in dilute HCl and

* Miracle dgf 125, Dry Graphite Film Lubricant, Miracle Power Products, Corp., Cleveland, Ohio 44109.

(4) Thermophysical Properties Research Center Data Book. Purdue University.

(5) M. R. Lorentz, et al., "Some Properties of a Double Acceptor Center in CdTe," Phys. Rev. 134, p. 751 (1961).

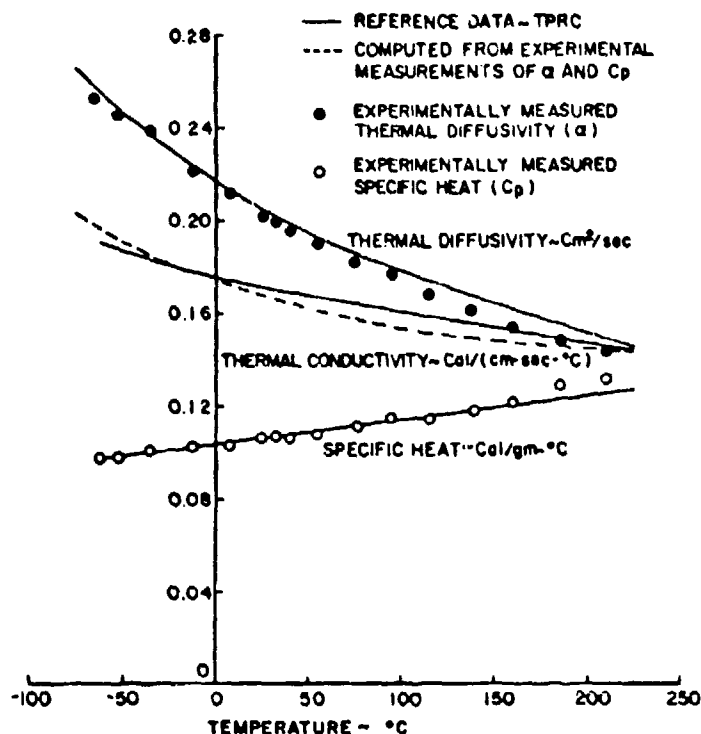


Figure 4. Thermal Properties of Armco Iron.

rinsed with deionized water. The NaOH treatment, which was intended to remove any free Te and its oxides, produced a red reaction on the surface of the samples. Frequently, plumes of this reaction product were ejected from grain boundary regions and several samples split along grain boundaries during this step of the cleaning process. It is believed that the two phenomena were related; the specimen damage being produced by the penetration of NaOH into grain boundaries and the subsequent wedging action produced by the reaction product which formed.

The ZnSe samples were degreased and cleaned in a 50% NaOH solution following the procedure of Aven and Segall.⁽⁶⁾

(6) M. Aven and B. Segall, "Carrier Mobility and Shallow Impurity States in ZnSe and ZnTe," Phys. Rev. 130, p. 21, (1963).

Both materials were electroded by heating the entire sample on a hot plate and applying solder connections ultrasonically through a mask. Initially, both In and Pb-In solder were used. Indium solder proved to be mechanically and electrically superior and ultimately most measurements were made with indium soldered connections.

The ohmic character of the soldered contacts on the CdTe samples was evaluated by measuring their I-V and transfer characteristics. Plots of the I-V characteristics were obtained by recording the current through the sample as an imposed voltage was varied ± 10 volts. As shown in Figure 5, some departure from ohmic behavior was observed. For the most part, however, the I-V characteristics were considered satisfactory. Transfer characteristics were measured by varying the voltage across one pair of leads while monitoring the voltage across another pair. Plots of these transfer voltages for a span of ± 10 volts exhibited varying degrees of nonlinearity. Some samples, especially those with Pb-In contacts, exhibited a double-valued character when the current and Hall leads were used. While this behavior is not understood, it could be due to space charge effects around the contacts or the influence of grain boundaries which in many instances separated the contacts from each other. The anomalous transfer characteristics cause the Hall measurements of these samples to be suspect. Conversely, the I-V characteristics would indicate that reliable resistivity measurements were obtained.

A block diagram of the facility used in the measurement of resistivity and Hall coefficient is shown in Figure 6.

A variable temperature dewar capable of operating from 4.2° K up to 450° K was used. Specific sample temperatures were achieved by simultaneously electrically warming the sample holder with a resistance heater and cooling it with a flow of vapor produced by boiling the liquid cryogen with a second heater located in the base of the dewar. Individual voltage-regulated power supplies provided a capability for precise regulation of input

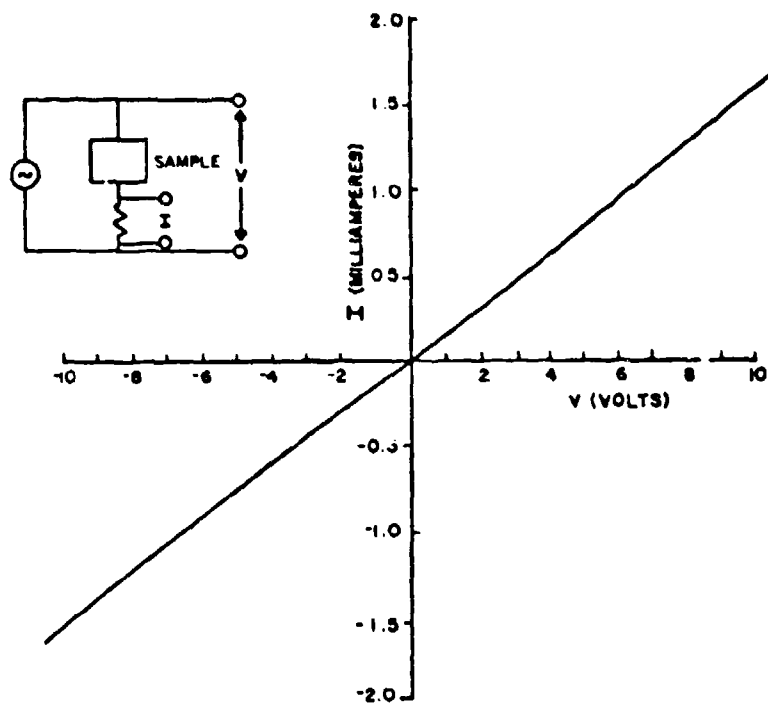


Figure 5. Typical I-V Characteristic of an Electrical Resistivity-Hall Coefficient Specimen.

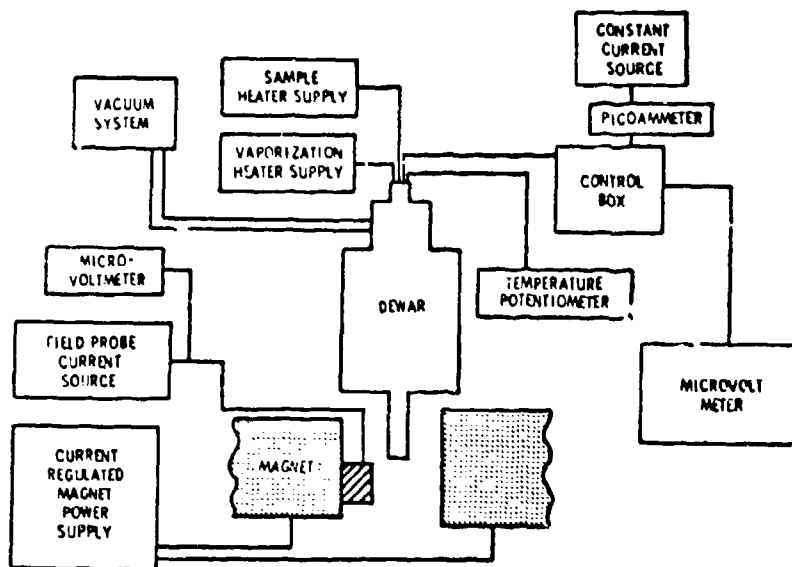


Figure 6. Block Diagram of the Resistivity-Hall Coefficient Facility.

power to each heater. Sample temperature was measured with a commercial copper-constantan thermocouple. A conventional vacuum system consisting of a mechanical forepump and an oil diffusion pump was used to evacuate sections of the dewar during the initial cool-down.

The magnetic field required for the Hall measurements was provided by an electromagnet with 18 cm diameter poles tapering to 10 cm at a gap of 4.1 cm. With this pole piece configuration, the maximum attainable field was 12 kOe. A switching arrangement was incorporated in the 5 Kw power supply of the magnet so that the magnetic field direction could be easily reversed.

Hall measurements were made at a field strength of 10 kOe. An In-As Hall probe powered by a constant current source was used in conjunction with a microvolt-ammeter to monitor the magnetic field. This probe was calibrated using nuclear magnetic resonance techniques.

Precise resistivity measurements require a stable current flow through the sample. A constant current power supply patterned after that described by Eden and Zakrzewski⁽⁷⁾ was used. This power supply provided current regulation to better than 0.1% and was suitable for resistance measurements over the range of a few ohms to approximately 50×10^6 ohms. A voltage-regulated power supply was used with samples having a resistance greater than 50×10^6 ohms.

A switching circuit provided the means for measuring test voltages and voltage across the resistivity and Hall leads with either a potentiometer or an electrometer. Current was monitored in this circuit with a microvolt ammeter. When sample resistance exceeded 10^{10} ohms, the ohmmeter mode of the electrometer was used.

(7) E. C. Eden and W. H. Zakrzewski, "Semi-Automatic Hall Effect Measurement System," RSI 41, p. 1030, 1970.

At specified temperatures, measurements of the sample current and the voltage across the resistivity leads for both forward and reverse current were made with the magnetic field turned off. The magnetic field was then applied to the sample and Hall voltages measured for the four permutations of current and magnetic field direction. Reversing the current subtracted out the offset voltage. These measurements yielded the resistivity and Hall coefficient, which in turn were used to calculate the sign, mobility, and concentration of charge carriers.

The sign of the charge carrier was also determined using a hot probe technique. This is a simple procedure in which one of the two current leads was heated with a soldering iron to thermally induce a potential across the leads. The sign of the induced charges was determined with a microvoltmeter. Since mobile charges will tend to migrate to the cold lead, this lead will develop a positive potential if the sample is p-type and conversely, if the cold lead becomes negative with respect to the hot lead, the sample is n-type. This technique is most effective with semiconductors have a noncomplex free-carrier population.

3. RESULTS

3.1 II-VI COMPOUNDS

3.1.1 Raytheon ZnSe

3.1.1.1 Background

Zinc selenide produced by Raytheon by chemical vapor deposition (CVD) was the most extensively evaluated of the II-VI compounds. The CVD process involves a high temperature reaction between Zn vapor and H_2Se gas to produce a ZnSe deposit on a suitably inert substrate. Ordinarily, a large rectangular graphite block served as the substrate with the ZnSe deposit forming on four sides of the block. Upon completion of a process run, the ZnSe is removed from the substrate in the form of two small slabs (Plates B and D) and two larger slabs (Plates A and C).

Specimens from 13 different process runs were evaluated in this study. Primary emphasis was placed upon the mechanical properties of ZnSe and more than 300 test bars of the nominal dimensions, 1.0 x 1.0 x 7.6 cm, were evaluated for flexural strength or a related property. The remnants of these test bars served as a source of test specimens for measurements of thermal diffusivity, thermal conductivity, specific heat, electrical resistivity, and coefficient of thermal expansion and for the microstructural characterization of this material. Measurements of fracture toughness, fatigue behavior were also conducted. The statistics of brittle fracture were investigated using a Weibull-based model to account for the influence of specimen size. This analysis was eventually employed to establish a proof-test for full-sized ZnSe components.

The homogeneity of a large ZnSe plate with respect to spatial variation of strength, Young's modulus, Poisson's ratio, and microstructure was evaluated. As part of this study, the influence of loading rate and temperature upon strength, Young's modulus, and Poisson's ratio was also determined.

3.1.1.2 Microstructural Analysis

The microstructure of the Raytheon ZnSe was typical of that shown in Figure 7. Individual grains were heavily twinned and somewhat elongated. Microscopic examination of the substrate and deposition surfaces and the cross section of the samples revealed no significant differences in appearance. As indicated in the summary of mean grain size measurements of Table 1, there was a modest variation of mean grain size from run to run but for any given run, the grain size values were relatively consistent among the three surfaces analyzed. Examination of fracture surfaces at low power magnification revealed a columnar structure perpendicular to the growth direction.

TABLE 1. SUMMARY OF MEAN GRAIN SIZE MEASUREMENTS
OF RAYTHEON ZnSe

Run Number	Substrate Surface	Mean Grain Size (μm)	
		Cross Section	Deposition Surface
58	50	57	45
59	59	70	71
60	66	65	67
61	40	45	43
62	57	49	42
63	--	--	--
69	55	48	53
76	43	53	46
82	47	51	51
92	36	40	31
94	38	33	40
96	43	45	43
113	24	27	25
Average		47	46



Polished Section, Sample 114

250X



SEM, Sample 96

250X

Figure 7. Typical Polished Section and Scanning Electron Micrograph of Raytheon ZnSe.

3.1.1.3 General Specimen Appearance

Distinct run-to-run color variations were noted among the sample sets evaluated. Coloration ranged from light lemon-yellow to a dark orange. All of the specimens contained alternating bands of clear and hazy material, 0.5 to 5.0 mm in thickness, oriented parallel to the deposition plane. The banding was very prominent in some specimens and barely visible in others. The number of bands also varied from run-to-run from as few as two bands in the Run 62 specimens to as many as ten bands in the specimens from Run 63.

This haziness may have been due to H_2Se gas entrapped in microscopic pores. Raytheon has reportedly discovered micron-sized triangular smooth-walled pits when hazy samples were carefully polished and etched.

The characteristic garlic-like odor of H_2Se has been observed when hazy specimens are crushed or broken in flexural testing. Perkin-Elmer personnel have also noticed this odor when grinding large ZnSe plates.

Many of the specimens, especially those from earlier process runs, contained 2 to 5 black spherical inclusions per cubic centimeter of material. These inclusions were approximately 50 μm in diameter and were identified by energy dispersive analysis as slag-covered zinc particles probably carried over with the zinc vapor in the CVD process. In later runs, Raytheon installed filters in their CVD apparatus and the incidence of metallic inclusions was markedly reduced. Occasional irregularly shaped yellow inclusions were also observed in the ZnSe specimens. These were believed to be ZnSe dust particles which dropped on the deposition surface and were subsequently encapsulated by CVD ZnSe.

The first group of specimens prepared by Raytheon (Runs 58, 59, 60, 61, and 62) had well polished, nearly scratch-free surfaces. The edges and corners of these specimens were beveled by diamond grinding, an operation which left a string of small chips at the intersection of the bevel and

polished sides of the specimens. Most beveled surfaces were grooved by the grinding medium and there were occasional gouges and chips 1.0 to 2.0 mm wide. These specimens contained curved orange striations visible only when viewing the specimens from the side perpendicular to their growth direction. Microscopic examination revealed that these striations were shallow fissures produced by a diamond saw cutting operation.

It was suspected that the residual surface flaws associated with edge beveling and diamond sawing would seriously compromise the strength of these specimens. This was subsequently confirmed in a series of tests which demonstrated that strength increases exceeding 30% could be realized with the elimination of surface finishing flaws.

Edge beveling was eliminated in favor of full rounding and polishing of edges to achieve a flaw-free, curved surface with a smooth transition to the sides of the specimen. It was specified that the specimens would be free of visible chips and fissures at 30X magnification. However, this was rarely, if ever, achieved and most specimens contained a few surface pits and small chips. Experiments with carefully prepared flawless test bars proved that residual finishing artifacts in the form of minor pits and chips were not detrimental with respect to strength.

During this evaluation of finishing procedures, a simple technique for edge finishing was developed by the University of Dayton Research Institute (UDRI) personnel which was quite satisfactory. Rough saw-cut edges were reduced to a smooth well-rounded and microscopically flawless condition in a matter of minutes by hand polishing, using a Pellon paper backing and diamond paste in progressively finer grit sizes of 15, 9, and 1 μm .

3.1.1.4 Thermal Properties

Coefficient of thermal expansion measurements were obtained with four specimens from Run 61 (Plate 61C) over the temperature range of -80° to $+200^{\circ}\text{C}$. From -80° to $+120^{\circ}\text{C}$, linear expansion curves with a

coefficient of 7.0×10^{-6} cm/cm $^{\circ}$ C were obtained. At higher temperatures, there was a slight upward curvature of the expansion trace which increased the coefficient to 8.0×10^{-6} cm/cm $^{\circ}$ C (see Figure 8). These results are consistent with the observations of Zhdanova and Sergeev,⁽⁸⁾ who reported a similar increase of expansion coefficient with temperature.

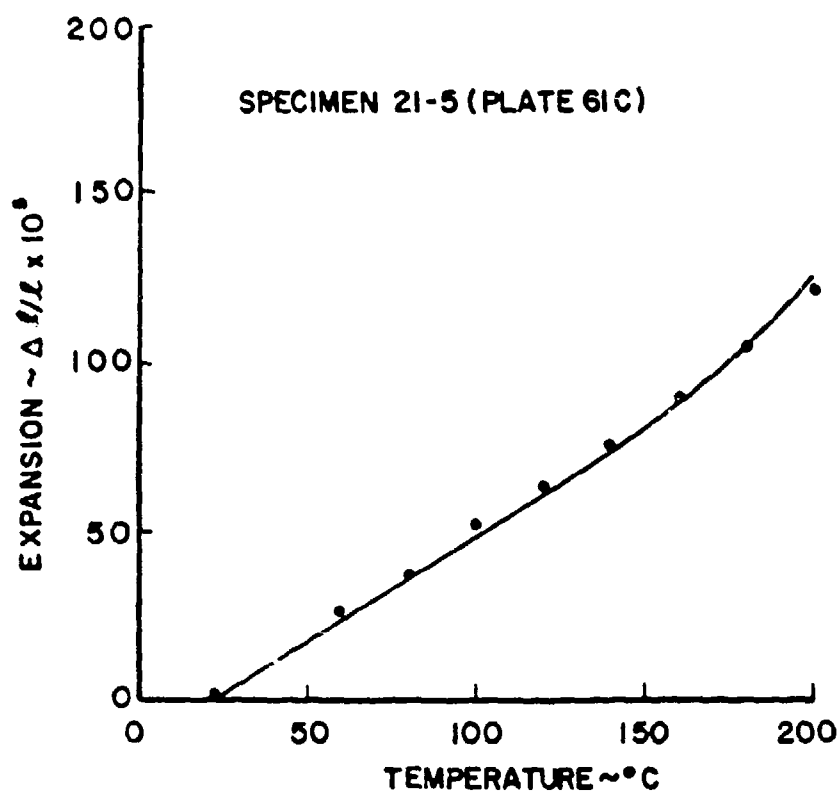


Figure 8. Typical Thermal Expansion Curve for Raytheon ZnSe.

(8) V. V. Zhdanova and V. P. Sergeev, "Thermal Expansion of ZnSe in the Temperature Range 100-600 $^{\circ}$ K," Soviet Physics-Solid State, Vol. 14, No. 7, January 1973.

The thermal diffusivity and specific heat of ZnSe from Run 61 was measured over the temperature range of -65° to $+200^{\circ}\text{C}$. These measurements were performed on two specimens; one 0.180 cm thick, the other 0.360 cm thick. As shown in Figure 9, both specimens exhibited the expected monotonic decrease of thermal diffusivity with increasing temperature. The thicker specimens consistently exhibited higher values of thermal diffusivity. The 0.184 cm thick specimen displayed a smooth linear increase of specific heat with increasing temperature whereas the specific heat of the 0.360 cm specimen was more erratic, especially below room temperature.

Thermal conductivity values were derived from graphically smoothed values of specific heat and thermal diffusivity and are shown in Figure 9 as a range of values encompassing the extremes represented by both specimens. Included with these data, are values independently obtained for CVD ZnSe by Dynatech Corporation and Haury of the Air Force Materials Laboratory using conventional steady-state thermal conductivity measurement techniques. The three sets of thermal conductivity data were in excellent agreement except in the range of 0° to 20°C where the steady-state data fell slightly above the range defined by the pulse method.

3.1.1.5 Electrical Resistivity

The Raytheon ZnSe consistently exhibited high electrical resistivity with typical values of 10^{12} ohm-cm at 4.2°K diminishing to 10^{10} ohm-cm at room temperature. Most of these measurements were performed on fine grained polycrystalline specimens. The role of grain boundaries relative to bulk resistivity was clearly illustrated by a series of electrical resistivity measurements with ZnSe which had been annealed for 28 hours at 930°C . As is apparent in Figure 10, the heat treatment induced significant grain growth. From an initial grain size of $54\text{ }\mu\text{m}$, large equiaxed grains 1.0 mm in diameter were found; many of these grains contained massive lath-like twin bands.

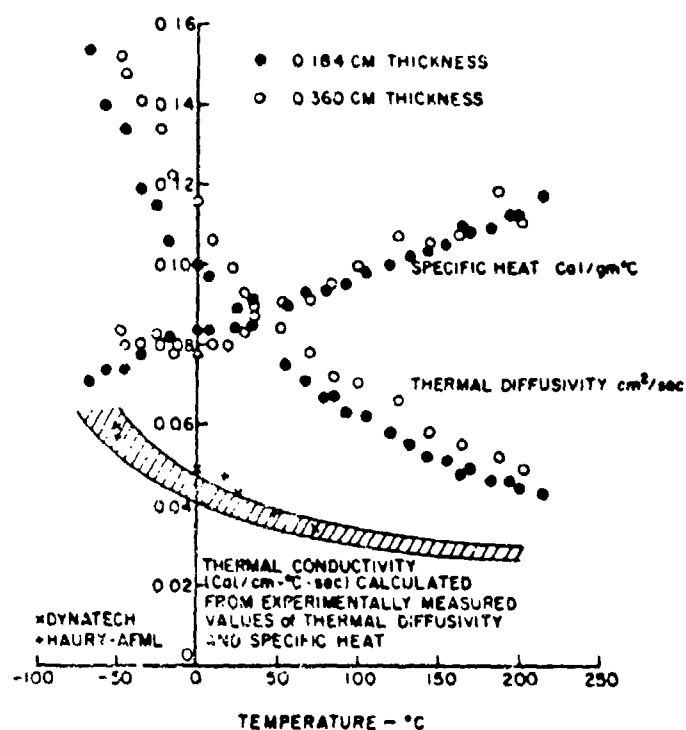


Figure 9. Thermal Properties of CVD ZnSe.

Plots of log resistivity against inverse temperature for as-deposited and annealed ZnSe were linear over the range of 10^6 to 10^{12} ohm-cm (Figure 11). At all temperatures, the annealed material had a lower resistivity. Both sets of data could be fitted with a straight line having a slope equivalent to an activation energy of 2.7 eV; a value quite close to the reported band gap for ZnSe.⁽⁹⁾ Nonlinearity was observed at resistivities above 10^{12} ohm-cm which is not surprising since the equipment had not been designed for extremely high resistivity measurements. Furthermore, surface conduction effects would be anticipated at these high levels of resistivity. Thus, only those measurements below 10^{12} ohm-cm are considered valid and higher values should be disregarded because of equipment limitations and probable surface conduction effects.

(9) F. A. Horrigan and R. I. Rudco, "Materials for High Power CO₂ Lasers," Raytheon Company Final Report on Contract DA-AH01-69-C-0038, Sept. 1969.



Before



After

Figure 10. Microstructure of ZnSe Before and After Annealing. (75X)

The offset in the resistivity curve of annealed ZnSe is believed due to a reduction in the number of high resistance grain boundaries. Earlier studies had shown that grain boundaries dominate the bulk resistivity of polycrystalline CdTe (see Section 3.1.7). It was suspected that similar behavior might prevail in ZnSe. Laser probe measurements similar to those performed on polycrystalline CdTe were attempted with the annealed ZnSe. Electrodes were placed on either end of the sample and photovoltage was monitored as a focused He-Ne laser beam traversed along the length of the sample. Unlike CdTe, which is opaque to a He-Ne laser, ZnSe is transparent at this wavelength. Consequently, laser beam penetration to subsurface grain boundaries and internal scattering complicated the experiment. However, it was possible to obtain strong photovoltage signals from several well defined grain boundaries lying on the sample surface which qualitatively resembled the photosignals obtained with CdTe.

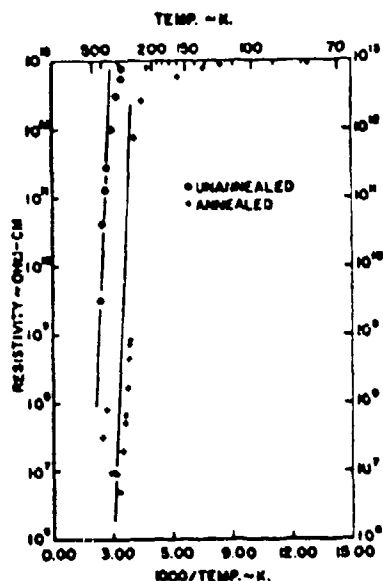


Figure 11. Resistivity versus Reciprocal Temperature of Annealed and Unannealed ZnSe.

3.1.1.6 Flexural Strength

Initial measurements of flexural strength were performed on test bars measuring 0.2 x 0.3 x 3.0 cm. A total of eleven such specimens; eight with beveled and polished edges and three with rough sawn edges, were evaluated. The results of these tests, combined with similar data obtained by AFWL, are summarized in the cumulative distribution plot of Figure 12. The resulting smooth distribution curve would indicate an apparent insensitivity of the ZnSe to potentially influential factors such as specimen finish and origin of test data. Subsequent testing of larger specimens in greater quantity revealed these and other factors to be statistically significant.

The first set of large specimens evaluated (0.75 x 1.0 x 7.6 cm) were from Process Runs 60, 61, 62, and 63. The results are summarized in Table 2. As indicated in a previous section, these specimens were rather poorly finished, especially on their edges which were covered with potentially weakening chips, pullouts, and microfissures. The flexural strength data for the specimens of Runs 60, 61, and 62 would indicate that their poor edge condition had weakened the material. Average strength ranged from 3.97 to 4.55 ksi with coefficients of variation of 10.8 to 12.7%. An analysis of variance applied to these data indicated no statistical significance with respect to strength for the variables of process run or specimen location within a given plate. The specimens from Plate 61C designated by the five-digit numbers (61-21-4, 61-21-5, etc.) were honed by Raytheon to partially finish the ground edges. This produced a slight improvement in strength and a slight reduction in the coefficient of variation.

The specimens from Run 63 were prepared by Raytheon with ground bevels of uniform width. These specimens were free of microfissures. The Run 63 specimens were stronger than the others but the coefficient of variation was nearly doubled. It would appear that, in the absence of microfissures, the strength of these specimens was controlled by the presence of stronger, but more variable, grinding defects.

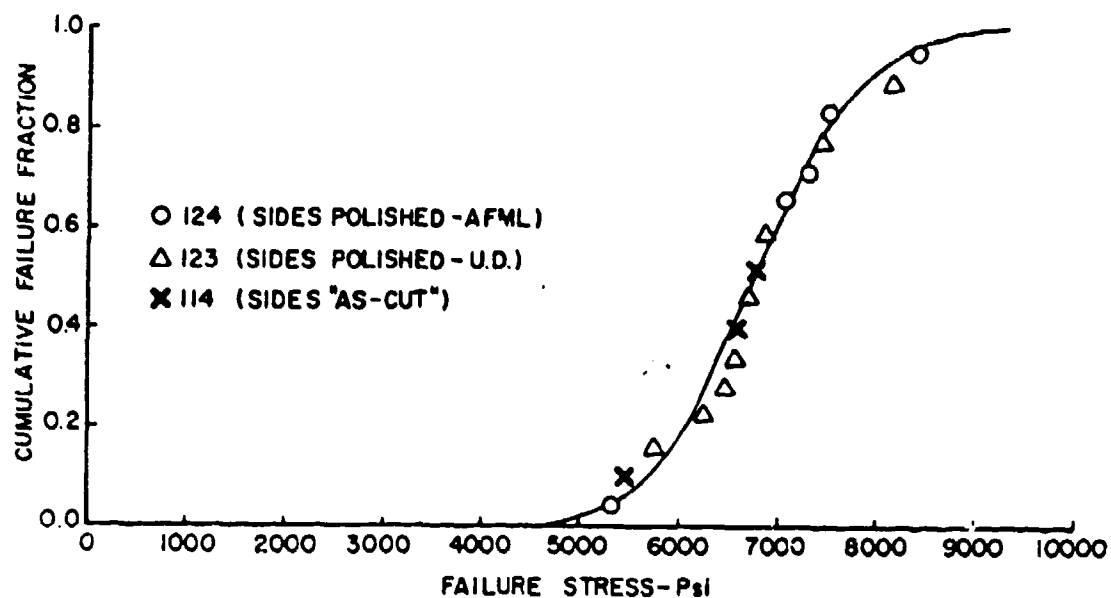


Figure 12. Cumulative Failure Distribution of Flexural Strength for Raytheon ZnSe.

TABLE 2. RESULTS OF FLEXURAL STRENGTH MEASUREMENT
OF RAYTHEON ZnSe

Process Run and Sample Number	Ultimate Strength (ksi)	Remarks
60-1	4.42	Prepared by a Raytheon sub- contractor; edges badly damaged, sharply beveled with numerous chips and scratches, and non- uniform radii. Pressure cracks on sides of samples. Samples contained a heavy concentration (20/cc) of bulk inclusions 0.1 to 0.5 mm in diameter.
-3	4.20	
-5	3.92	
-6	3.57	
-8	4.90	
-10	3.31	
-11	3.63	
-13	3.52	
-15	3.75	
Average	3.97	
Std. Deviation	0.43	
Coef. of Variation	10.8%	
62-1	4.92	Prepared by Raytheon sub- contractor; edges badly damaged, sharply beveled with numerous chips and scratches, and non- uniform radii. Pressure cracks on sides of samples. Samples contained bulk inclusions 50 μ m at a frequency of 2-5 per cc.
-3	4.18	
-5	4.83	
-6	3.92	
-8	4.16	
-10	3.81	
-11	5.03	
-13	4.73	
-15	5.41	
Average	4.55	
Std. Deviation	0.52	
Coef. of Variation	11.4%	
61-1	5.57	Prepared by Raytheon sub- contractor; edges badly damaged, sharply beveled with numerous chips and scratches, and non- uniform radii. Pressure cracks on sides of samples. Samples contained bulk inclusions 50 μ m at a frequency of 2-5 per cc.
-3	3.99	
-5	4.49	
-6	5.15	
-8	4.29	
-10	4.02	
-11	4.28	
-13	3.64	
-15	4.35	
Average	4.42	
Std. Deviation	0.56	
Coef. of Variation	12.7%	

TABLE 2 RESULTS OF FLEXURAL STRENGTH MEASUREMENT
OF RAYTHEON ZnSe (continued)

Process Run and Sample Number	Ultimate Strength (ksi)	Remarks
61-21-4	4.84	Edges honed after grinding to partially remove flaws. Samples from Run 61, Plate C.
-21-5	5.04	
-21-6	5.60	
-41-4	6.13	
-41-5	4.96	
-41-6	4.75	
Average	5.22	
Std. Deviation	0.49	
Coef. of Variation	9.4%	
63-1	7.36	Sample edges diamond ground by Raytheon to produce bevels of uniform width with sharp corners. Grinding marks were visible at low power magnifica- tion and occasional chips were present.
-2	4.73	
-5	5.03	
-6	6.08	
-7	7.62	
-8	8.23	
-9	7.85	
-10	4.81	
-11	7.68	
-14	7.58	
Average	6.70	
Std. Deviation	1.32	
Coef. of Variation	19.7%	
61-2	6.61	Refinished by Raytheon to obtain crack-free sides, uniformly rounded smooth, moderately defect-free edges.
-4	7.60	
-7	6.98	
-9	7.41	
-12	7.56	
-14	7.02	
Average	7.28	
Std. Deviation	0.36	
Coef. of Variation	4.9%	

TABLE 2. RESULTS OF FLEXURAL STRENGTH MEASUREMENT
OF RAYTHEON ZnSe (continued)

Process Run and Sample Number	Ultimate Strength (ksi)	Remarks
64-1	5.64	Edges hand polished to remove all defects except for a scatter- ing of 40 μ m edge pits.
-2	5.19	
-3	6.82	
-4	5.15	
-5	7.96	
-6	4.91	
-8	6.34	
-11	7.27	
-13	6.80	
-15	6.81	
Average	6.29	
Std. Deviation	0.47	
Coef. of Variation	7.5%	
64-9	4.61	Beveled sides removed; edges and sawn sides repolished to a flawless condition at 30X magnification.
64-12	6.74	
69A-1	6.49*	These samples from Plate A. Samples were moderately well finished with a few polishing pull-outs and remnants of cracks in regions where defects were repaired.
-2	6.38	
-3	7.40	
-4	6.88	
-5	7.19	
-6	7.40	
-7	8.32	
-8	7.65	
-9	6.52	
-10	6.98	
Average	7.12	
Std. Deviation	0.57	
Coef. of Variation	8.0%	

* Failed at a repaired defect.

TABLE 2. RESULTS OF FLEXURAL STRENGTH MEASUREMENT
OF RAYTHEON ZnSe (continued)

Process Run and Sample Number	Ultimate Strength (ksi)	Remarks
82-1	--	Samples were from an unspecified side plate (B or D) from Run 82. Samples were moderately well finished.
-2	7.64	
-3	7.48	
-4	6.97	
-5	8.17	
-6	8.41	
-7	6.09	
-8	7.55	
-10	7.10	
-11	6.98	
Average	7.38	
Std. Deviation	0.66	
Coef. of Variation	8.9%	
92-1B	7.06	Tests performed by Raytheon. Samples from Run 92; Plate B.
-4B	7.56	
-5B	6.85	
-9B	6.55	
Average	6.99	
Std. Deviation	0.35	
Coef. of Variation	5.0%	
92-2B	5.21	Tests performed by UDRI. Samples from Run 92; Plate B. Samples were moderately well finished.
-3B	6.12	
-6B	6.77	
-7B	7.12	
-8B	5.82	
-10B	6.00	
Average	6.17	
Std. Deviation	0.62	
Coef. of Variation	10.0%	
92-17D	8.98	Tests performed by Raytheon. Samples were from Run 92; Plate D.
-18D	8.33	
-19D	8.18	
-20D	7.62	
Average	8.28	
Std. Deviation	0.48	
Coef. of Variation	5.8%	

TABLE 2. RESULTS OF FLEXURAL STRENGTH MEASUREMENT
OF RAYTHEON ZnSe (continued)

Process Run and Sample Number	Ultimate Strength (ksi)	Remarks
92-11D	8.27	Tests performed by UDRI. Samples were from Run 92; Plate D. Samples were moderately well finished.
-12D	7.93	
-13D	7.95	
-14D	7.20	
-15D	7.13	
-16D	8.60	
Average	7.85	
Std. Deviation	0.53	
Coef. of Variation	6.8%	
94-B	6.65	Tests performed by Raytheon. Samples were from Run 94; Plate B.
	7.59	
	5.24	
	6.16	
Average	6.41	
Std. Deviation	0.85	
Coef. of Variation	13.2%	
94-3B	7.09	Tests performed by UDRI. Samples were from Run 94; Plate B. Samples were moderately well finished.
-6B	7.20	
-8B	5.34	
-9B	7.65*	
-11B	6.86*	
-12B	6.81*	
Average	6.83	
Std. Deviation	0.72	
Coef. of Variation	10.5%	
94-D	7.26	Tests performed by Raytheon. Samples from Run 94; Plate D.
	6.97	
	6.16	
	7.88	
Average	7.07	
Std. Deviation	0.62	
Coef. of Variation	8.8%	

* Tested with an Instron Testing Machine.

TABLE 2. RESULTS OF FLEXURAL STRENGTH MEASUREMENT
OF RAYTHEON ZnSe (continued)

Process Run and Sample Number	Ultimate Strength (ksi)	Remarks
94-2D	7.43	Tests performed by UDRI. Samples from Run 94; Plate D. Samples were moderately well finished.
-3D	6.37	
-5D	7.15	
-6D	7.20*	
-8D	8.48*	
-9D	6.87*	
Average	7.25	
Std. Deviation	0.64	
Coef. of Variation	8.8%	
96-B	6.25	Tested by Raytheon. Samples from Run 96; Plate B.
	5.48	
	5.17	
	5.49	
Average	5.60	
Std. Deviation	0.40	
Coef. of Variation	7.1%	
96-2B	3.51	Tested by UDRI. Samples from Run 96; Plate B. Samples were moderately well finished but were very hazy and heavily banded.
-3B	4.16	
-5B	3.76	
-6B	6.13	
-8B	7.01	
-9B	7.10	
Average	5.28	
Std. Deviation	1.51	
Coef. of Variation	28.9%	
96-D	5.93	Tested by Raytheon. Samples were from Run 96; Plate D.
	7.52	
	7.36	
	6.05	
Average	6.72	
Std. Deviation	0.73	
Coef. of Variation	10.9%	

* Tested with an Instron Testing Machine.

TABLE 2. RESULTS OF FLEXURAL STRENGTH MEASUREMENT
OF RAYTHEON ZnSe (continued)

Process Run and Sample Number	Ultimate Strength (ksi)	Remarks
96-12D	6.71	Tested by UDRI. Samples were from Run 96; Plate D. Samples were moderately well finished but were very hazy and heavily banded.
-13D	7.19	
-15D	6.29	
-16D	6.27	
-18D	7.87	
-19D	6.68	
Average	6.84	
Std. Deviation	0.56	
Coef. of Variation	8.2%	
96B(position 16-24)-1	4.53	Specimens were from Run 96; Plate D and were taken from a region of clear ZnSe. Specimens were not well finished. Edges were poorly rounded with numerous pullouts and chips. Several samples contained pressure cracks.
-2	5.84	
-3	7.20	
-4	6.49	
-5	7.28	
-6	5.81	
-7	6.74	
-8	6.33	
-9	7.06	
-10	6.16	
Average	6.34	
Std. Deviation	0.79	
Coef. of Variation	12.4%	
113-A-1	3.74	Samples from Run 113; Plate A. Samples had exceptionally well finished edges; surfaces contained only minor scratches; some samples contained bulk inclusions and hazy regions.
-2	3.68	
-3	3.80	
-4	3.83	
-5	3.38	
-6	3.99	
-7	5.00	
-8	4.07	
-9	5.00	
-10	4.15	
-11	5.91	
-12	3.82	
Average	4.03	
Std. Deviation	0.72	
Coef. of Variation	17.9%	

TABLE 2. RESULTS OF FLEXURAL STRENGTH MEASUREMENT
OF RAYTHEON ZnSe (continued)

Process Run and Sample Number	Ultimate Strength (ksi)	Remarks
113-C-1	2.81	Samples from Run 113; Plate C. Sample condition was the same as those from Run 113; Plate A.
-2	4.54	
-3	3.83	
-4	4.49	
-5	4.03	
-6	2.79	
-7	5.53	
-8	4.50	
-9	5.00	
-10	6.07	
-11	5.96	
-12	8.01	
Average	4.80	
Std. Deviation	1.39	
Coef. of Variation	29.0%	
113-D-1	5.80	Samples from Run 113; Plate D. In general these samples were not well finished. Edges were rough and poorly rounded. This group of samples were from the upper or deposition side of the plate.
-3	5.08	
-5	4.44*	
-7	6.50	
-9	6.60	
-11	6.92	
-13	6.98	
-15	6.54	
-17	6.26	
-19	7.91	
Average	6.08	
Std. Deviation	0.79	
Coef. of Variation	13.0%	

* Pressure cracks and large chips in the gage section.

TABLE 2. RESULTS OF FLEXURAL STRENGTH MEASUREMENT
OF RAYTHEON ZnSe (concluded)

Process Run and Sample Number	Ultimate Strength (ksi)	Remarks
113-C-2	6.59	Samples from Run 113; Plate I.
-4	6.12	In general these samples were not well finished. Edges were rough and poorly rounded.
-6	6.01	
-8	6.99	
-10	6.53	This group of samples were from the lower or substrate side of the plate.
-12	4.95	
-14	4.51	
-16	5.00*	
-18	6.52	
-20	5.24*	
Average	5.84	
Std. Deviation	0.84	
Coef. of Variation	14.4%	

* Pressure cracks and large chips in the gage section.

The benefits of careful edge and surface finishing were clearly demonstrated by the performance of six specimens from Run 61 which were re-worked by Raytheon. The edges of these specimens had a uniform radius and were polished smooth with just a moderate amount of fine pitting. All microfissure damage was removed and the sides were polished to optical smoothness. With this improved surface finish, the average strength of the Run 61 specimens increased from 4.42 to 7.28 ksi and the coefficient of variation dropped from 12.7% to 4.9%.

Ten test bars from Run 64 were hand polished by UDRI personnel in an attempt to obtain samples with flawless edges. Despite a determined effort, small pits approximately 40 μ m in diameter remained on the edges even though polishing times were substantially in excess of what is normally required to finish a rough diamond sawn edge. The strength of these bars ranged from 4.91 to 7.96 ksi and averaged 6.29 ksi. These values were for "as received" test bars with moderately well finished edges.

The edge pits, which would not polish away, might have been the result of subsurface damage caused by Raytheon's chamfering operation. To evaluate this possibility, the sides of two Run 64 specimens were trimmed to a depth of approximately 0.8 mm. The sides and edges were then polished to a defect-free condition (no visible flaws at 30X magnification). The strength of these two specimens was an unimpressive 4.61 and 6.74 ksi.

It would, therefore, appear that the strength of these samples, in the absence of edge flaws, was controlled by critical flaws distributed in the bulk of the material.

Fabrication specifications were modified as a result of this study. Edge bevels were eliminated in favor of fully rounded and polished edges. Subsequent experience with moderately well finished specimens revealed that while edge-located microfissures would cause serious degradation of strength, small edge chips and pits could be tolerated.

Quality control specimens from Runs 69 and 82 were prepared with fully rounded and polished edges. Ten specimens from each run yielded nearly identical results; i. e., an average strength of 7.1 to 7.4 ksi and coefficients of variation of 8.0 to 8.9%.

Runs 92, 94, and 96 were represented by ten-specimen sets from Plates B and D of each run. Four specimens of each set were tested by Raytheon; the remainder by UDRI.

The material from these three runs was inclusion-free, but there were marked differences in optical clarity. The Run 92 samples were slightly hazy and banded; the Run 94 samples were exceptionally clear; and, the Run 96 materials was heavily banded and quite hazy.

The strength data for the three runs was treated with an analysis of variance to determine the statistical significance of the independent variables: testing laboratory (Raytheon or UDRI), Run number (62, 94, or 96), plate identity (B or D), and the paired interactions of these variables. Two of the

independent variables, plate identity and run number, proved to be statistically significant and both were significant at the 99% confidence level. Plate differences accounted for 70% of the observed variance of strength, 25% was attributed to differences among process runs and 5% was due to uncontrolled experimental factors.

In every specimen set, the material from Plate B was stronger than that from Plate D. Optical clarity and strength appeared to be related. The very hazy Run 96 ZnSe was significantly weaker than the clear material from Runs 92 and 94. The observation was reinforced by a ten-specimen evaluation of Run 96 material taken from a clear region of Plate B. Despite a relatively poor edge finish, the average strength of the clear specimens was 6.34 ksi as compared with an average of 5.41 ksi for cloudy material.

Run 113 represented an unsuccessful attempt to produce an optically clear, 2.5 cm thick ZnSe deposit. This material was nonuniformly hazy with regions of heavy inclusion content. A total of 44 test specimens; 12 each from Plates A and C and 20 from Plate D, were evaluated.

The Plate A and C specimens were unusually weak with average strength 4.0 and 4.8 ksi respectively. In contrast, the Plate D material had an average strength of 5.96 ksi. The strength difference between Plate D and Plates A and C was statistically significant.

3.1.1.7 Weibull Analysis of Flexural Strength Data

Brittle materials such as ZnSe will exhibit a statistical distribution of strength with structural failure initiating at the largest preexisting flaw when the stress on this flaw reaches a critical value. The frequency and size of flaws in a material will increase with specimen size and, therefore, an inverse relationship between the size of a brittle component and its strength can be anticipated.

The results of simple laboratory flexural strength tests can be employed in the analysis of more complicated load bearing structures through the use of a suitable mathematical model which accounts for the statistical behavior and size dependence of brittle materials. One such model is the Weibull distribution-function.

The basic Weibull equation for an isotropic material containing volume-distributed flaws and loaded uniaxially is given by

$$F(n) \begin{cases} = 1 - \exp - \int_V \left(\frac{\sigma_n - \sigma_u}{\sigma_o} \right)^m dV & \text{for } \sigma_n > \sigma_u, \text{ otherwise} \\ = 0 \end{cases} \quad (9)$$

where

$F(n)$ is the cumulative fraction of failed items at imposed stresses up to and including the level σ_n .

σ_u is the location parameter or the zero probability strength; i.e., the stress level below which no failures will occur.

σ_o is the scale parameter.

m is the shape parameter or the flaw density exponent.

The parameters σ_u , σ_o , and m are parameters uniquely related to the material and its process history and independent of test bar geometry or stress distribution.

Evaluation of the integral in Equation (9) for use with flexural strength data must include consideration of the tensile stress gradient within the bulk of a prismatic bar subjected to four-point bending. Weil and Daniel⁽¹⁰⁾ derived the appropriate equation for this situation and presented it in the following form:

$$F(b) = 1 - \exp - \frac{V}{2(m+1)} \left(\frac{\sigma_b - \sigma_u}{\sigma_o} \right)^m \left(1 - \frac{\sigma_u}{\sigma_b} \right) \quad (10)$$

where

V is the volume of material between the two inner load points of the fixture.

σ_b is the maximum tensile stress in the bar.

Evaluation of the Weibull parameters, σ_u , σ_o , and m, from experimental data can be accomplished by either graphical or numerical techniques. A numerical analysis written in a statistical format for processing by digital computer is preferable to graphical analysis when large quantities of data are involved, i.e., more than 100 data points. Numerical analysis is less effective with small sample lots of 20-30 and in such cases, graphical analysis may be more appropriate.

A three-parameter numerical analysis based upon the simple Weibull expression,

$$F(x) = 1 - \exp - K \left(\frac{\sigma - \sigma_u}{\sigma_o} \right)^m \quad (11)$$

has been developed by Harter and Moore⁽¹¹⁾ using a maximum likelihood technique to obtain unbiased parameter estimates.

(10) N.A. Weil and I.M. Daniel, "Analysis of Fracture Probabilities in Nonuniformly Stressed Brittle Materials," J. Am. Cer. Soc., 47(6)268, June 1964.

(11) L.H. Harter and A.H. Moore, "Maximum Likelihood Estimation of the Parameters of Gamma and Weibull Populations from Complete and Censored Samples," Technometrics (7), 639-643, (1965).

Attempts to adapt the Harter-Moore analysis to the modified Weibull expression of Equation (1) have been unsuccessful to date. However, a similar treatment of Equation 2 using a two-parameter model (by assigning a value of zero to σ_u) has provided excellent results.

The assumption of a zero value for σ_u is not totally unrealistic in the case of ZnSe. Graphical analysis of flexural strength data has indicated that while the σ_u parameter for ZnSe has a finite value, its magnitude is probably on the order of 500 psi. The assignment of a zero value to σ_u would, therefore, lead to somewhat conservative but useful predictions of the strength capabilities of ZnSe.

Flexural strength data for ZnSe were compiled and evaluated using the two-parameter numerical analysis. This compilation of data included the test results for 89 samples from Runs 61, 64, 69, 82, 92, and 94. These were moderately well-finished specimens from normal CVD process runs.

The Weibull parameters derived from this analysis were as follows:

$$\begin{aligned}n &= 7.97 \pm 0.43 \\ \sigma_o &= 2.763 \text{ ksi} \\ \sigma_u &= 0 \text{ (assumed)}\end{aligned}$$

The cumulative distribution function associated with these Weibull parameters is shown in Figure 13 with the experimental data employed in this analysis.

3.1.1.8 Evaluation of Plate 61C

Background

A large ZnSe plate from Run 61 (designated Plate 61C) was inadvertently broken during removal from its graphite substrate and thereby became available as a source of test specimens for a detailed evaluation of a typical plate of CVD ZnSe. A schematic diagram of the plate with

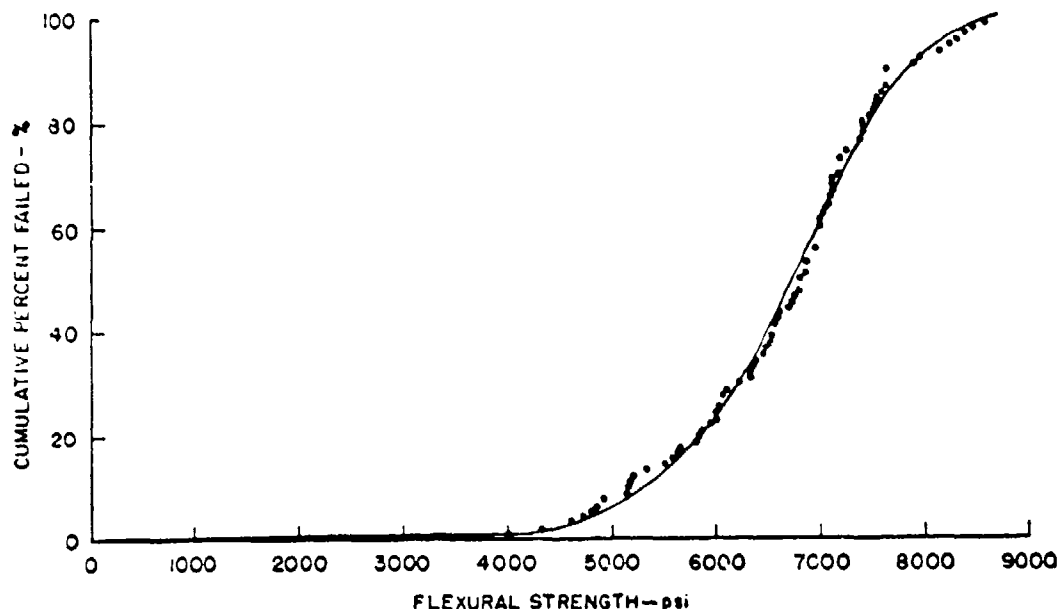


Figure 13. Cumulative Failure Distribution of ZnSe
Fitted with a Weibull Distribution.

a layout of the test specimens obtained from it is shown in Figure 14. Where possible, the plate was subdivided into 3.0 x 3.0 inch modules which could yield up to six test bars nominally 0.3 x 0.4 x 3.0 inches. These modules were numbered 1 through 8 along the X-axis (the direction of the reactant gas flow). The direction transverse to the reactant gas flow (the Y-axis) was divided into five modules. Each test bar location within a module was numbered. Thus, with a three-digit notation, the module location and the position within that module were specified.

Two separate evaluations were conducted on the specimens from Plate 61C. The homogeneity of the plate with respect to the X and Y coordinates of the plate and the orientation of the test bar was evaluated. A second set of experiments determined the influence of loading rate, temperature and orientation upon the flexural strength, elastic modulus, and Poisson's ratio of ZnSe.

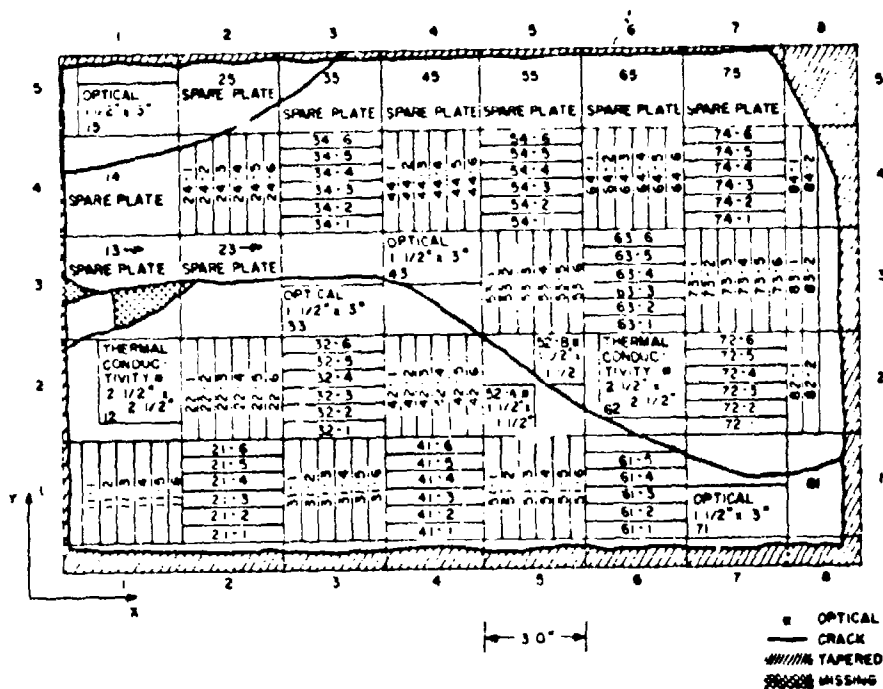


Figure 14. Test Specimen Layout.

Homogeneity Evaluation of Plate 61C

Measurements of thermal expansion and microstructural evaluations were performed on selected samples from Plate 61C. Room temperature flexural strength, however, was the principal criterion for evaluating the homogeneity of this plate. Sets of six test bars from modules 21, 24, 41, 44, 61, and 64 were evaluated in four-point bending at a loading rate of 0.02 inches/min. Pairs of test bars from each module were tested in each of three orientations; with the deposition surface, substrate surface, or cross section in tension.

The experimental plan employed in this evaluation and the strength values obtained are given in Table 3. The interpretation of the results of such an experiment involves a standard statistical procedure termed an analysis of variance. With this technique, the variances of a

TABLE 3. EXPERIMENTAL LAYOUT OF HOMOGENEITY EVALUATION

Y-Location	<u>X-Location</u>								
	2			4			6		
	Orientation			Orientation			Orientation		
	I	II	III	I	II	III	I	II	III
1	21-1 *	21-2	21-3	41-1	41-2	41-3	61-1	61-2	61-3
	21-4	21-5	21-6	41-4	41-5	41-6	61-4	61-5	61-6
4	24-1	24-2	24-3	44-1	44-2	44-3	64-1	64-2	64-3
	24-4	24-5	24-6	44-4	44-5	44-6	64-4	64-5	64-6

* Specimen Number

Flexural Strength Values (ksi)

Y-Location	<u>X-Location</u>								
	2			4			6		
	Orientation			Orientation			Orientation		
	I	II	III	I	II	III	I	II	III
1	6.70	5.51	5.87	5.58	6.46	7.08	6.96	6.56	7.00
	--	--	--	--	--	--	6.04	6.56	--
4	5.66	5.17	6.21	7.52	5.95	6.06	6.04	--	4.33
	4.86	4.77	4.00	6.59	7.42	6.33	4.74	5.85	6.53

I = Substrate Side in Tension
 II = Cross section in Tension
 III = Deposition Side in Tension

measured output parameter (in this case, flexural strength) associated with each of the independent variables (X-location, Y-location, and orientation) are compared with the random variance due to all uncontrolled factors to determine which, if any, of the independent variables exert a statistically significant influence upon the output parameter. The same procedure can be applied to paired combinations of independent variables (two-factor interactions) to test for synergistic effects.

The test was originally designed as a replicated experiment; that is, each combination of independent variables was represented twice, thereby increasing the sensitivity of the analysis.

Initial flexure tests with specimens 21-4, 21-5, 21-6, 41-4, 41-5, and 41-6 yielded unexpectedly low strengths. The entire lot of test specimens at this time had sharply beveled edges. The remaining specimens were returned to Raytheon for edge-rounding before further tests were conducted.

The presence of a crack prevented the fabrication of a complete set of specimens from module No. 61 and, therefore, specimen 61-6, even though part of the experiment, was never available for testing. Specimen 64-2 was accidentally broken during test.

Despite these specimen losses, every combination of independent variable was tested at least once. The analysis of variance was performed by treating the data as an unreplicated experiment, ignoring those data where test conditions were duplicated. The analysis was then repeated as a replicated experiment using statistical procedures to generate the missing data. The results of these two analyses were virtually identical. The overall average strength of the test bars was 6.1 ksi with a standard deviation of 0.77 ksi. None of the independent variables (X-location, Y-location, or orientation) either individually or in paired combination with one another had a statistically significant influence upon the strength of the test bars; or at least no significant effects could be

separated from the "scatter" of the data due to uncontrolled variables (such as edge finish variations). It was, therefore, concluded that within the precision of this evaluation, the plate could be regarded as being homogeneous with respect to flexural strength.

Microstructural evaluation of specimens selected from six representative regions of the plate did not exhibit significant differences in appearance or mean grain size. These data are summarized in Table 4.

Thermal expansion measurements of specimens taken from three of the four plate corners were, within the precision of this measurement, identical.

Therefore, with respect to strength, microstructure, and thermal expansion, Plate 61C was found to be homogeneous.

TABLE 4. SUMMARY OF MEAN GRAIN SIZE MEASUREMENTS
OF PLATE 61C

Specimen Number	Deposition Surface (μm)	Cross Section (μm)	Substrate Surface (μm)
21-1	36	46	37
24-4	48	47	44
41-1	41	47	44
44-1	42	41	33
61-4	41	47	41
64-4	52	45	45
Average	43	45	40

The six specimens of module 64 were instrumented with T-type strain gages on their tension and compression faces. Elastic deformation under load in the transverse and longitudinal direction was used to determine elastic modulus and Poisson's ratio in both compression and tension. Virtually identical results were obtained in compression and tension, the elastic modulus averaging 10.5×10^6 psi and the Poisson's ratio 0.30.

Loading Rate, Temperature, and Orientation Effects

A statistically designed experiment similar to that employed in the homogeneity evaluation was used to evaluate the influence of temperature, loading rate, and orientation upon the strength of ZnSe.

A total of 24 test bars from Plate 61C were evaluated in four-point bending at temperatures of -55° and $+65^\circ$ C, loading rates of 0.2 and 0.002 inches/min,* at the three orientations (substrate surface, deposition surface, and cross section in tension). Half of these specimens were instrumented with T-type strain gages for measurement of elastic modulus and Poisson's ratio.

The results of this evaluation, which are summarized in Table 5, were treated with several analyses of variance. The flexural strength results for all 24 specimens were analyzed and then separate analyses were performed on the 12 instrumented specimens to determine the effects of temperature, loading rate, and orientation upon the elastic modulus and Poisson's ratio.

The strength analysis clearly indicated that the presence of the strain gages lowered the strength of the test bars by more than 1.0 ksi. This is believed to be the consequence of the surface abrasion required to secure a good strain gage bond. No decrease in strength had been noted in the earlier instrumented tests of the homogeneity evaluation.

* This corresponded to approximate stress rates of 24 and 2400 psi/sec.

Two different technicians were involved in the instrumentation of test bars and it is possible that the weakening effect of the strain gages was due to differences in specimen preparation. It is also possible that with the fewer specimens involved in the homogeneity evaluation, the sensitivity of the analysis was insufficient to detect strain-gage effects.

TABLE 5. RESULTS OF LOADING RATE, TEMPERATURE AND ORIENTATION EVALUATION

			-55°C			+65°C		
			Orientation			Orientation		
			II	III	I	II	III	
Win out	Strain Gage	0.2	--	7.56	7.13	6.69	6.73	8.13
		0.002	6.52	6.95	7.49	7.43	--	8.23
With	Strain Gage	0.2	7.11 ^a	6.93	7.09	4.47	3.88	6.48
			10.8	10.8	10.5	10.3	10.2	9.9
			0.29	0.28	0.29	0.30	0.29	0.30
		0.002	4.01	6.41	3.39	5.33	6.74	6.06
			11.3	10.9	10.6	9.9	8.0	9.7
			0.34	0.33	0.29	0.33	0.34	0.31

*These values are flexural strength (ksi), elastic modulus (10^6 psi), and Poisson's ratio.

I = Substrate side in tension.

II = Cross section in tension.

III = Deposition side in tension.

Neither temperature, orientation, or loading rate nor their interactions exerted a statistically detectable influence upon the strength of the ZnSe. The mean strength of the uninstrumented test bars was 6.7 ksi with a standard deviation of 0.90 ksi.

The elastic modulus of ZnSe was sensitive only to temperature and exhibited a statistically significant decrease from a mean value of 10.82×10^6 psi at -55°C to a mean value of 9.67×10^6 psi at $+65^\circ\text{C}$. The standard deviation of these values was approximately 0.51×10^6 psi.

Poisson's ratio values were unaffected by temperature but were significantly influenced by orientation and loading rate and the interaction of these two independent variables. The mean values of all these measurements was 0.31 with a standard deviation of 0.02.

The observed dependence of Poisson's ratio on loading rate and orientation is believed to be due to instrumental factors rather than to variations in the response of the material. The strain gages employed in these measurements were relatively large with respect to the sample dimensions. The side mounted gages extended almost to the edges of the specimens and in general these measurements exhibited the largest variations. Oscillographic techniques were used to measure the strain gage response and frequently these traces were difficult to read. Nevertheless, the absolute magnitude of the statistically significant variations induced by the loading rate and orientation were small and are not regarded as particularly important.

3.1.1.9 Proof and Fatigue Testing of ZnSe Bars

Mechanical test bars from Runs 58, 59, 60, and 62 were refinished by Raytheon after preliminary tests (Table 2) had indicated a problem with defective edges. These specimens and a set from Runs 69 and 76 were evaluated in a modified procedure which incorporated a proof test. The proof test consisted of loading the bars at a normal cross head rate

of 0.02 in/min to a proof stress of 6.8 ksi. The load on those specimens which survived the initial proof stress was relaxed to an equivalent stress of 200 psi (to prevent displacement of the specimen in the fixture); the load was then reapplied at a cross head rate of 0.02 in/min to specimen failure.

The proof stress of 6.8 ksi was expected to fail 40 to 60% of the specimens. While this was unrealistically severe in the usual sense of proof testing, it served the two-fold purpose of accentuating any susceptibility of ZnSe to proof test damage and provided ample statistics above and below the proof stress level.

The results of these tests are compiled in Table 6. Prior to pooling these data for an evaluation of proof stress effects, the data for each process run were compared using a one-way analysis of variance to determine if any of the groups were statistically different from the others. It was assumed in these analyses that the two-step loading cycle had no significant effect upon the test results. This assumption was justified in subsequent analyses.

The analyses of variance indicated that all of the strength data except that of Run 60 could be treated as a homogeneous statistical population. All of the Run 60 specimens failed below the proof stress level. These specimens contained an unusually high concentration of massive inclusions which are believed to have weakened the material.

Approximately half of the remaining specimens failed below the proof stress. The weaker of these specimens had an average strength of 6.03 ksi with a standard deviation of 0.80 ksi. The retested survivors of the proof test had an average strength of 7.15 ksi and a standard deviation of 0.40 ksi. Four of the proof test survivors failed below the proof stress level, the weakest of these at 6.6 ksi, thereby providing evidence that the proof test had induced slight damage.

TABLE 6. SUMMARY OF PROOF TESTED ZnSe

Process Run and Sample Number	Ultimate Strength (ksi)	Process Run and Sample Number	Ultimate Strength (ksi)
58-2	5.43*	59-1	6.33*
-4	6.62*	-2	7.33
-5	4.34*	-7	6.60
-6	6.47*	-8	5.60*
-7	6.31*	-10	3.89*
-9	7.30	-11	5.89
-10	6.73	-12	6.66*
-12	7.46		
-14	7.15		
Average	6.42	Average	6.18
Std. deviation	0.93	Std. deviation	1.06
Coef. of variation	14.5 %	Coef. of variation	17.1 %
60-2	5.98*	62-2	7.65
-4	3.90*	-4	6.59*
-7	4.31*	-7	6.67*
-9	4.33*	-9	6.57*
-12	5.24*	-12	6.74
-14	5.15*	-14	5.82*
Average	4.82	Average	6.67
Std. deviation	0.70	Std. deviation	0.53
Coef. of variation	14.6 %	Coef. of variation	8.0 %
69-3	7.31	76-2	6.59*
-5	7.37	-3	7.65
-6	7.06	-4	7.68
-7	5.54*	-5	7.93
-8	6.28*	-8	6.67
-9	6.80	-10	5.78*
-11	6.65	-12	7.00
-12	7.22	-13	6.53*
-13	6.60*	-15	6.05*
-15	7.10		
Average	6.79	Average	6.88
Std. deviation	0.53	Std. deviation	0.71
Coef. of variation	7.8 %	Coef. of variation	10.3 %

* Failed on initial loading below the proof stress level.

The virgin test data fell within a 90% confidence interval about the cumulative distribution curve for a Weibull function with the parameters $m = 7.97$, $\sigma_0 = 3.763$ ksi, and $\sigma_u = 0$ (see Figure 15). Therefore, the proof test specimens were assumed to be part of the same statistical population employed in the derivation of the Weibull parameters for ZnSe (Section 3.1.1.6).

Equation (2) was modified to account for the truncation of strength imposed by the proof test. With this modification, the predicted distribution of the proof test survivors took the form:

$$F(b) = \begin{cases} 1 - \exp - \frac{V\sigma_0^{-m}}{2(m+1)} \left[\frac{1}{\sigma_b} (\sigma_b - \sigma_u)^{m+1} - \frac{1}{\sigma_p} (\sigma_p - \sigma_u)^{m+1} \right] & ; \sigma_b > \sigma_p \\ 0 & ; \sigma_b \leq \sigma_p \end{cases} \quad (12)$$

where

σ_p is the proof stress.

The graphical solution of Equation (12) for a σ_p of 6.8 ksi using the Weibull parameters for ZnSe is also shown in Figure 15. The dotted lines bracketing this curve represent the 5% and 95% confidence limits for a sample size of 21.

The array of experimental data for the proof test survivors fell below the predicted strengths. This is regarded as additional evidence that the proof load had damaged the ZnSe specimens.

The indication of proof stress damage prompted an evaluation of the cyclic load sensitivity of ZnSe at a more realistic proof load. A group of 21 mechanical test bars from Plate 61C were cycled to 4.0 ksi twenty times and then loaded to failure. The results of these tests are summarized in Table 7.

One test bar failed at 4.0 ksi during the first loading cycle. This was not totally unexpected since the failure probability at this proof stress

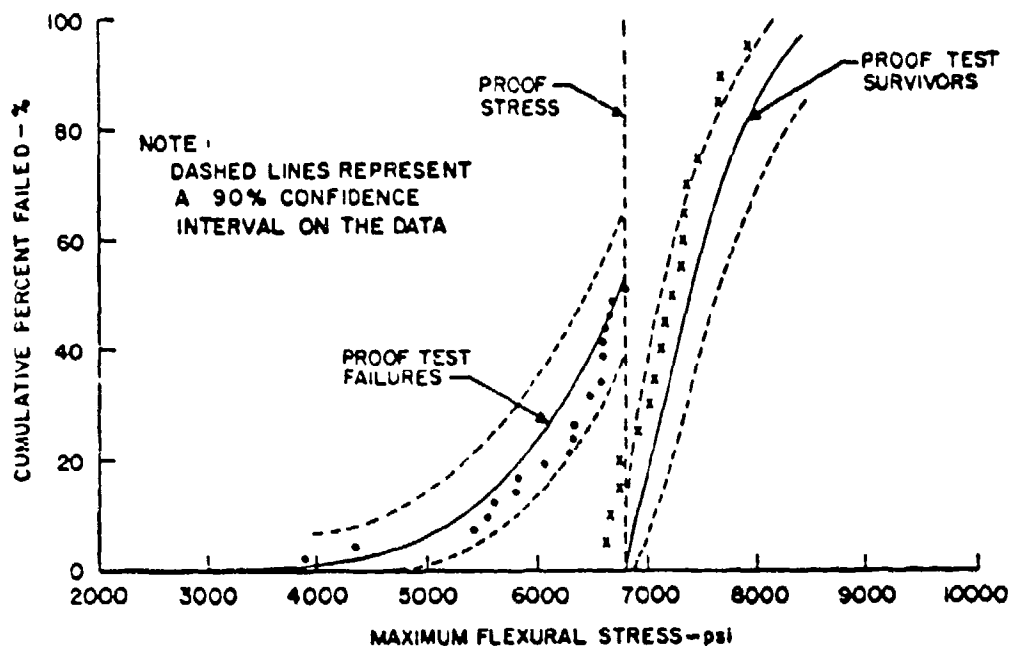


Figure 15. Cumulative Failure Distribution of ZnSe
Proof Tested at 6800 psi.

level is on the order of 5%. The remaining 20 specimens survived the full 20-cycle sequence and exhibited ultimate strengths ranging from 5.1 to 6.8 ksi. Their average strength was 5.93 ksi, a value nearly equal to the average strength of Plate 61C material. A statistical comparison between the load-cycled specimens and virgin ZnSe revealed a significant difference in strength. The effect of repetitive loading was also apparent in the cumulative distribution of strength as compared with the predicted distribution derived from Equation 12 for a proof stress of 4.0 ksi (Figure 16). There was a significant displacement of the empirical distribution towards lower stress levels presumably as a consequence of noncatastrophic damage accumulated during load cycle sequence.

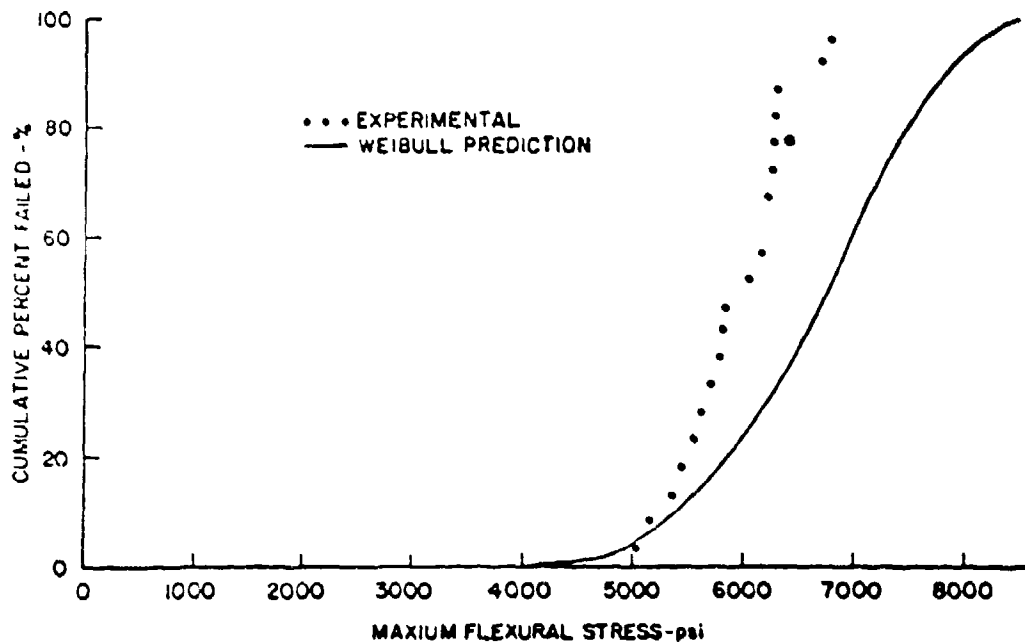



Figure 16. Cumulative Failure Distribution of ZnSe
Proof Tested at 4000 psi.

Nine other mechanical test bars from Plate 61C were fatigue tested in four-point bending by personnel of the Air Force Materials Laboratory. Individual specimens were evaluated at peak cyclic stresses ranging from 2.05 to 6.10 ksi. Run-out, in excess of 10×10^6 cycles, was obtained for stresses up to 5.79 ksi. A second specimen failed in 174,000 cycles at this stress level. Specimens tested at 5.9 and 6.1 ksi failed in less than one cycle. The fatigue test results are listed in Table 7 with post-test ultimate strengths for the six specimens which went to run-out. Residual strengths ranged from 5.42 to 7.17 ksi. The number of specimens involved was too few to statistically confirm a loss of strength from cyclic loading even though some degradation was anticipated in view of proof test results.

TABLE 7. FATIGUE TEST RESULTS FOR RAYTHEON ZnSe
(PLATE 61C)

Maximum Cyclic Stress (ksi)	Cycles to Failure	Post-test Flexural Strength (ksi)
<u>High Cycle Fatigue (AFML)</u>		
2.05	Runout*	5.75
3.07	Runout	5.42
4.10	Runout	5.89
4.88	Runout	6.89
5.58	Runout	7.17
5.79	Runout	6.51
5.79	174000	
5.90	< 1	
6.10	< 1	
* > 10 x 10 ⁶ cycles.		
<u>Low Cycle Fatigue (UDRN)</u>		
4.00  4.00	Runout	5.81**
	Runout	6.73
	Runout	5.43
	< 1	
	Runout	5.04
	Runout	6.05
	Runout	6.22
	Runout	5.35
	Runout	6.22
	Runout	6.27
	Runout	5.55
	Runout	6.26
	Runout	6.80
	Runout	6.30
	Runout	5.70
	Runout	5.62
	Runout	5.14
	Runout	6.28
	Runout	5.77
	Runout	6.17
Runout	5.80	

**** Broke at load point.**

3.1.1.10 Static Fatigue

The loss of strength experienced by ZnSe after cyclic loading would suggest that this material is subject to environmentally assisted slow crack growth. This behavior, often referred to as static fatigue, is a form of stress-aided corrosion and is commonly observed in glasses and ceramics. The combined effect of tensile stress and chemical attack (usually water vapor) produces a time-dependent growth of surface flaws which eventually reach critical dimensions and become the initiation sites of catastrophic fracture.

A simple experiment, originally intended to evaluate the possibility of long term microcreep-induced permanent deformation in ZnSe, provided a preliminary indication of the nature of static fatigue in this compound. A mechanical test bar was dead-weight loaded in four-point bending and failed in less than 5 minutes at 5.33 ksi. Subsequent tests of 10 additional test bars were conducted at stress levels ranging from 3.8 to 6.4 ksi (Table 8).

TABLE 8. STATIC FATIGUE TESTS OF ZnSe

Stress Level (ksi)	Failure Time (min)	Remarks
3.78	15,900+	No failure
5.0	4	
5.33	4	
5.5	0	Failed on loading
5.5	0	Failed on loading
5.5	0	Failed on loading
5.5	4	
5.5	600	
5.5	6,600+	No failure
5.6	240	
5.6	7,200+	No failure

The 3.73 ksi test was suspended after 15,900 minutes without a sample failure. At 5.0 ksi, failure occurred in four minutes. Three specimens failed spontaneously when loaded to 5.5 ksi, whereas, two others failed in 4 and 600 minutes at this stress level and a sixth specimen survived 6,600 minutes without failing. At 5.6 ksi, one specimen failed in 240 minutes while a second specimen was removed from test, unfailed, after 7,200 minutes.

The delayed fracture behavior of ZnSe is consistent with an active static fatigue mechanism. Moreover, the wide variability of failure times indicate that there is a statistical character to this behavior.

Investigations now being conducted at the Naval Research Laboratories and the National Bureau of Standards have independently demonstrated that CVD ZnSe is susceptible to environmentally assisted slow crack growth. Water has been identified as the corrosion medium.

3.1.1.11 Fracture Toughness of ZnSe

The stress intensity factor for Mode I cracks (K_I) in ZnSe was measured using five specimens from Run 58. These measurements were in accordance with ASTM procedures for single-edge cracked bars in four-point bending. The specimens had span to depth ratio of 3:33 which exceeded the ASTM minimum value of 2.0 for such tests. Crack length to beam depth ratios (a/h) of 0.20 and 0.48 were evaluated. Cracks were placed in the specimen with a diamond saw using sufficient pressure to generate microscopically observable cracks at the base of the saw cuts. The stress intensity factor was calculated from the relationship:

$$K_I = \frac{3PX\sqrt{a}}{bh^2} Y = \sigma_b \sqrt{a} Y \quad (13)$$

where

P is the failure load.

σ_b is the maximum applied bending stress.

X is the distance between the inner and outer load points.

a is the initial crack depth.

Y is a constant related to the mode of test as defined by:

$$Y = 1.99 - 2.47(a/h) + 12.97(a/h)^2 \\ - 23.17(a/h)^3 + 24(a/h)^4.$$

The stress intensity factors thus obtained are summarized in Table 9. These data were relatively consistent despite a two-fold difference in crack length for the two sets of specimens. An average value of 616 psi $\sqrt{\text{in}}$ was obtained with a coefficient of variation of 0.06.

The fracture energy values associated with the stress intensity factor measurements were calculated from the relationship:

$$\gamma = \frac{(1-\mu^2)}{2E} K_I^2 \quad (14)$$

where

γ is the fracture energy.

μ is Poisson's ratio.

E is Young's modulus.

The results of this calculation are also summarized in Table 9.

Extrapolations of preliminary crack velocity data obtained by NRL for CVD ZnSe indicate a K_{IC} value of 1300 psi $\sqrt{\text{in}}$. Evans of NBS has measured a K_{IC} value of 900 psi $\sqrt{\text{in}}$ for the same material in similar experiments.**

* Private communication with S. W. Freiman, Naval Research Laboratories.

** Private communication with A. G. Evans, National Bureau of Standards.

TABLE 9. RESULTS OF FRACTURE TOUGHNESS MEASUREMENTS
OF RAYTHEON ZnSe

Specimen Number	Crack Depth (in.)	Stress Intensity Factor, K_I ($\text{psi}\sqrt{\text{in}}$)	Fracture Energy (J/m^2)
58-3	0.0605	643	3.29
58-15	0.0610	645	3.31
58-1	0.1498	612	2.98
58-11	0.1490	574	2.63
58-13	0.1490	609	2.95
Average		616	
Std. Deviation		37.7	

The relationship between flaw size and apparent strength was evaluated using Equation (13) for the two extreme values of K_I (616 and 1300 $\text{psi}\sqrt{\text{in}}$). The results of this calculation are summarized in Figure 17.

Approximately 200 ZnSe test bars have been evaluated with flexural strengths falling in the range of 3.0 to 8.6 ksi. According to Figure 17, the equivalent surface crack depths associated with this strength range should fall between 0.05 and 0.0014 inches.

All of the mechanical test specimens evaluated in this program were visually inspected at 30X magnification prior to test. None were free of surface defects. Polished surfaces always contained grain pull-outs typically 0.0015 inches in diameter and approximately 0.0075 inches in depth. Edge scratches and pits 0.002 to 0.005 inches deep were present on all moderately well finished specimens. Most specimens also contained zinc inclusions approximately 0.002 inches in diameter and somewhat smaller irregularly shaped particles of encapsulated ZnSe dust. These surface and bulk defects all represent potential sites for initiation of catastrophic crack growth. However, except in extreme cases where there are numerous grinding-induced pressure cracks or a large number of bulk inclusions

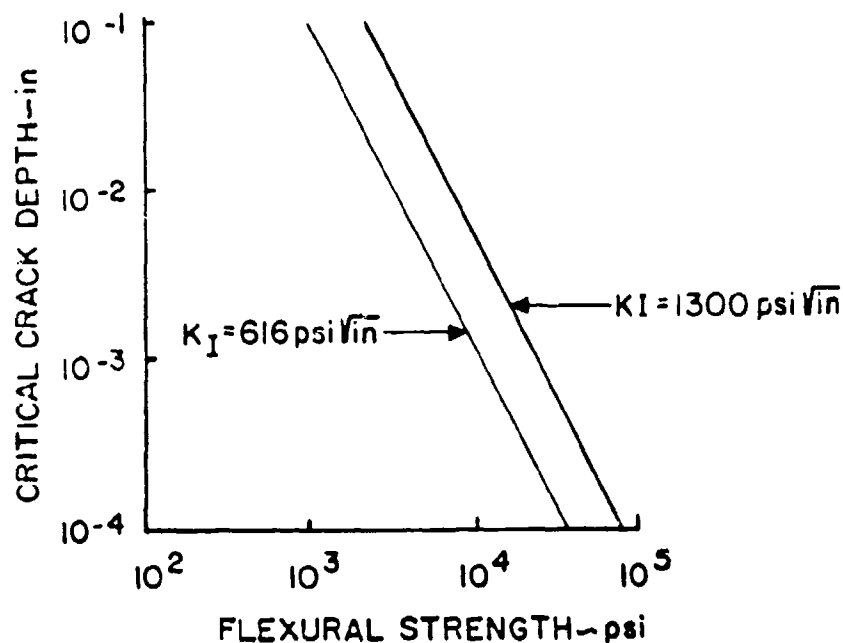


Figure 17. Flexural Strength of ZnSe as a Function of Critical Flaw Size.

(Run 60, for example). these microdefects do not appear to adversely affect strength. Removal of all surface defects by careful hand polishing did not increase the strength of the Run 64 mechanical test bars. This would suggest that the strength limiting flaws in CVD ZnSe are primarily volume-distributed. One possible source of volume-distributed flaws in ZnSe are the twin boundaries so prevalent in this material. Twin boundaries will block dislocation motion and, consequently, a material under stress can develop massive dislocation pile-ups on these twin boundaries. Cracks or internal voids can form by coalescence of dislocations and grow to catastrophic proportions. Dislocation-formed cracks could form along isolated twin boundaries and at intersections with other twin boundaries.

If this is the mechanism of volume-distributed flaw formation, then it should be possible to correlate the strength of ZnSe with the size of its twin boundaries. Since these twins bisect the individual grains of polycrystalline ZnSe, grain diameter provides a direct measure of twin boundary length. The size of a dislocation-formed internal void is limited to the length of the twin boundary upon which it forms. Therefore, the strength of ZnSe would be governed by the largest twinned grain favorably oriented with respect to the applied stress.

Equation (13) was rearranged to the form,

$$D = \left(\frac{K_I}{\sigma_b Y} \right)^2 \quad (15)$$

where a , the initial flaw depth, is replaced by D , the equivalent grain diameter.

Using a value of $K_I = 900 \text{ psi } \sqrt{\text{in}}$ and $Y \doteq 1.99$, equivalent grain sizes were calculated for the Gould, Coors, and Raytheon materials. These calculations are summarized in Table 10.

TABLE 10. EFFECTIVE GRAIN SIZE FOR TWIN BOUNDARY INITIATED BRITTLE FRACTURE IN ZnSe

Source	Average Ultimate Strength (ksi)	Equivalent Grain Size (μm)	Mean Grain Size (μm)
Coors	3.25	493	435
Gould	4.8	225	190
Raytheon	6.65	117	47

Relatively good agreement between the measured and calculated grain sizes were obtained for the Coors and Gould material. The equivalent grain size of the Raytheon ZnSe corresponding to an average strength of 6.65 ksi was 117 μm , approximately 2.5 times the mean grain size of this material.

However, large elongated grains 100 to 200 μm in length are not unusual in the CVD ZnSe; nearly every polished section examined contained several grains of this size.

3.1.1.12 Design of a Proof Test For ZnSe

Background

The use of large ZnSe components as optical elements in infrared laser systems presents serious design problems if thermal and mechanical loads capable of generating damaging stress are part of the operating environment. ZnSe is a brittle material and, as such, exhibits the size-dependent statistical distribution of strength characteristic of brittle materials. The uncertainties associated with the structural capacity of brittle components can be eliminated if each and every component is subjected to a proof-test simulating anticipated use conditions.

Proof testing provides a means whereby safe operating stresses can be established for a brittle structure. With this technique, those members of the statistical population too weak to survive in service are eliminated. The survivors, if undamaged by the proof test, are certified to have a structural capacity equal to or greater than the applied proof stress.

The establishment of an appropriate proof stress level usually involves a trade-off between the number of components which must be sacrificed to the proof test and the desired level of demonstrated structural capacity.

High quality, optical grade ZnSe is an expensive material of limited availability. Proof testing of ZnSe hardware must be accomplished with an acceptable risk of failure and yet the proof loads must be sufficient so that unrealistic operational constraints are not imposed on the component. To provide some guidance in the solution of suitable proof test loads, an analysis combining Weibull statistics and a finite element analysis was developed to utilize uniaxial strength data for predictions of the reliability of complex structures subjected to triaxial stresses.

Experimental verification of the Weibull/finite element analysis was accomplished in a series of tests using glass specimens as a brittle analog for ZnSe. Weibull parameters were obtained for the glass from flexural tests of bar specimens. These parameters were used to predict the burst pressures of the glass disks using a closed-form analytical expression derived expressly for the biaxial stresses which develop in this specimen geometry. Typical large sectors of glass were also pressure tested to failure to verify reliability predictions based on a finite element analysis which incorporated the Weibull parameters obtained from the bar tests. Surface flaw models were employed in these analyses of the brittle behavior of glass.

Similar experiments, of a more limited scope, were also performed on CVD ZnSe. Bars were tested in four-point bending to obtain Weibull parameters which were incorporated in a reliability prediction of the pressure response behavior of ZnSe disks. In these analyses, it was assumed that the ZnSe failed by propagation of volume-distributed flaws.

The Weibull/Finite Element Analysis

The Weibull parameters for ZnSe, a volume-flaw material, were obtained from the expression for a prismatic bar in four-point loading given by Equation (10). All of the glass bars failed by crack initiation from one of the tensile-stressed edges. This permitted the use of the relatively simple Weibull expression:

$$F(b) = 1 - \exp - 2L \left(\frac{\sigma_b - \sigma_u}{\sigma_o} \right)^m \quad (16)$$

where L is the specimen distance between the inner load points.

The disk specimens were simply supported along their circumference and subjected to uniform pressure loading. Biaxial stresses (radial and tangential) develop in this situation which can be calculated as a function of radial position from the expression: ⁽¹²⁾

(12) R. J. Roark, Formulas for Stress and Strain, 3rd Ed., McGraw-Hill, New York, 1954.

$$\sigma_t = \frac{3wa^2z}{4kt^3} \left[(3k+1) - (k+3) \frac{r^2}{a^2} \right] \quad (17)$$

$$\sigma_r = \frac{3wa^2z}{4kt^3} \left[(3k+1) \left(1 - \frac{r^2}{a^2} \right) \right] \quad (18)$$

where

σ_t and σ_r are the tangential and radial stresses, respectively.

w is the applied pressure.

a is the radius of the disc.

k is $1/\mu$ where μ is Poisson's ratio.

t is the disc thickness.

z is the distance from the neutral axis in the thickness direction.

r is the radial distance from the center of the disc.

By incorporation Equations (17) and (18) in Equation (9) and completing the appropriate integration for either a surface- or volume-flaw model, Weibull expressions for a pressure loaded disc were obtained in the following form:

Surface-flaw model:

$$F(x) = 1 - \exp - \left\{ \frac{32\pi \cdot kt^2(k+1)}{3w(3k+1)(k+3)(m+1)\sigma_o^m} \left[\frac{3}{8} \frac{w}{kt^2} (3k+1) a^2 \cdot \sigma_u \right]^{m+1} \right\} \quad (19)$$

Volume-flaw model: $\sigma_u = 0$

$$F(x) = 1 - \exp - \left\{ \frac{\pi a^2 t}{(m+1)^2} \left[\frac{3w(3k+1)a^2}{8kt^2\sigma_o} \right]^m \left[\frac{k-1}{k+3} \right] \left[\left(\frac{2k-2}{3k+1} \right)^m - 1 \right] \right\} \quad (20)$$

In deriving Equations (19) and (20), it was assumed that the tangential and radial forces acted independently of one another and the total effect of the two resultant stresses upon component reliability could be taken as the sum of the individual tangential and radial reliability values, i. e.

$$R_{\text{total}} = R_{\sigma_t} \cdot R_{\sigma_r} \quad (21)$$

where

$$R \equiv 1 - F(x). \quad (22)$$

The finite element analysis used in the reliability predictions of the large glass sectors is an approximate numerical method which mathematically reduces complex structures to an equivalent array of simple geometrical forms. The technique converts stress producing inputs of loads and temperature gradients to corresponding forces on each equivalent element which in turn can be converted to the principal stresses on these elements. Weibull analysis, employing the empirically-derived materials parameters, can be used to determine the reliability of each element at its appropriate stress level. Then, by considering the brittle structure as a composite of series elements, the overall reliability of the structure can be determined from:

$$R_{\text{total}} \equiv R_1 \cdot R_2 \cdot R_3 \dots R_n \quad (23)$$

where

$$R \equiv 1 - F(x),$$

$F(x)$ being obtained from the appropriate Weibull function for the type of loading and the flaw distribution within the element.

Empirical determinations of Weibull parameters are usually based upon simple uniaxial tests. However, finite element analyses of complex structures often involve reliability calculations of elements subjected to triaxial stresses.

The simplest approach to computing the reliability of an element in triaxial loading involves an independent calculation of the element reliability

for each principal stress^{*} with the combined reliability being determined from the product of the three, i. e.,

$$R_1 = R_{(\sigma_1)} \cdot R_{(\sigma_2)} \cdot R_{(\sigma_3)},$$

and Equation (23) becomes:

$$R_{\text{total}} = \left(R_{\sigma_1} \cdot R_{\sigma_2} \cdot R_{\sigma_3} \right)_1 \cdot \left(R_{\sigma_1} \cdot R_{\sigma_2} \cdot R_{\sigma_3} \right)_2 \cdots \left(R_{\sigma_1} \cdot R_{\sigma_2} \cdot R_{\sigma_3} \right)_n \quad (24)$$

where it is assumed that compressive stresses do not contribute to the probability of failure and, therefore,

$$R_{\sigma} = 1 \text{ for } \sigma < 0. \quad (25)$$

Specimen Preparation

All of the glass specimens employed in this study were machined from a single sheet of commercial plate glass, thereby minimizing any problems of batch-to-batch reproducibility of the test material. A total of 135 mechanical test bars, 100 discs, and 18 sectors were fabricated. The mechanical test bars measured 0.3" x 0.4" x 3.0". The four longitudinal edges of the bars were fully rounded with a radius of approximately 0.060 inches. All four sides and the edges were optically polished such that no flaws could be detected at 30X magnification. The discs were 2 inches in diameter and 0.15 inches thick; the sectors were 0.310 inch thick and were in the form of a 60° circular wedge with an inner radius of 3.5 inches and an outer radius of 12.0 inches. The discs and sectors were polished to the same quality of finish as the mechanical test bars.

Twenty-four mechanical test bars and twenty 2-inch diameter discs (0.15 inch thick) of CVD ZnSe were fabricated from a pair of one-inch thick plates of low optical quality material (Raytheon Run 113).

* The principal stresses are defined as the normal stresses which act a set of orthogonal planes oriented such that the shear stresses on the orthogonal planes is zero. By convention, these principal stresses are designated σ_1 , σ_2 , and σ_3 , with σ_1 being the largest tensile stress.

Test Results

The 135 glass bars were tested at room temperature in four-point bending. Ultimate strengths ranged from 4.65 to 15.80 ksi. Equation (16) was treated with the Harter-Moore three-parameter model (see Section 3.1.1.6) to obtain the following Weibull parameters:

$$\begin{aligned}m &= 4.202 \\ \sigma_u &= 3.191 \text{ ksi} \\ \sigma_o &= 9.885 \text{ ksi}\end{aligned}$$

The calculated cumulative frequency distribution was in excellent agreement with the experimental data as shown in Figure 18. The Weibull parameters for glass were incorporated in Equation (19) to predict the reliability of the two-inch discs subjected to uniform pressure loading. A total of 100 discs were then pressure tested to failure using dry nitrogen gas as the pressurizing medium. Test times were short, less than 20 seconds, to minimize complications arising from slow crack growth. The computed and experimental reliability curves for the discs are shown in Figure 19. While the calculated curve was somewhat nonconservative, these results indicated it was possible with Weibull analysis to apply uniaxial test results to predict the structural behavior of specimens 5 times larger and subjected to biaxial stresses.

The Weibull parameters for glass were also used in a finite element-surface flaw analysis to predict the bursting pressures of the large glass sectors. Destructive tests were then performed by edge sealing the sectors in a rubber-lined steel frame and rapidly pressurizing the assembly with dry nitrogen. All of the sectors were failed in less than 24 seconds. While many of the sectors shattered into numerous fine fragments, those which could be reassembled after test (see Figure 20) clearly indicated that fracture had initiated at or near the center of the sector.

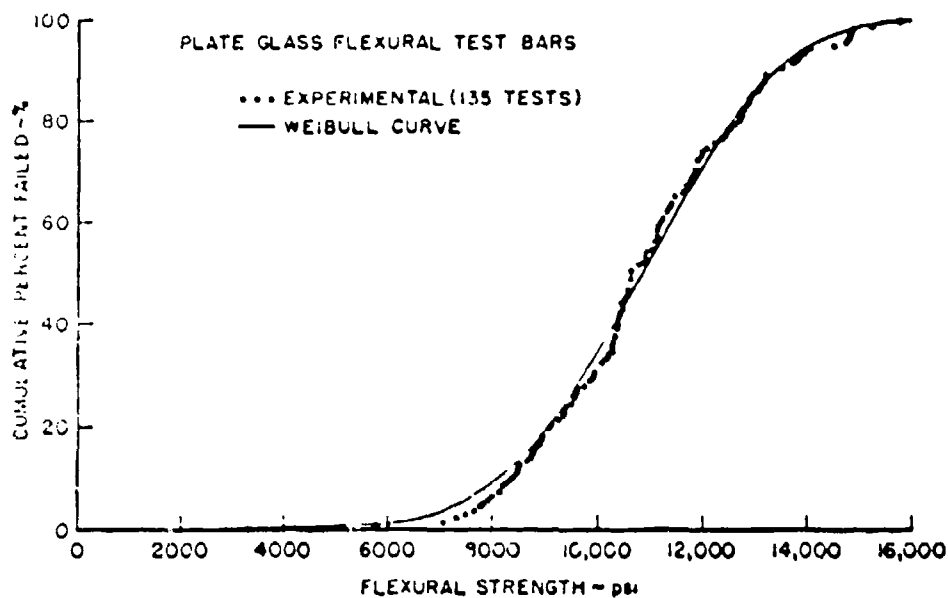


Figure 18. Cumulative Frequency Distribution of the Glass Flexural Test Bars.

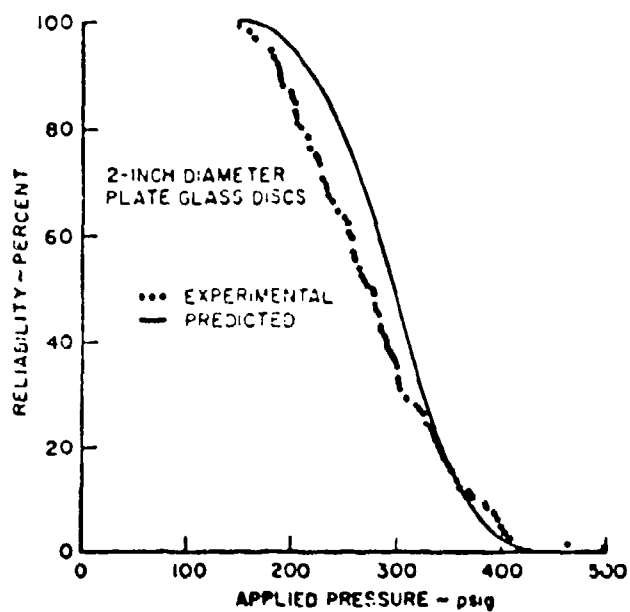


Figure 19. Reliability of Two-inch Glass Discs Subjected to Uniform Pressure Loading.

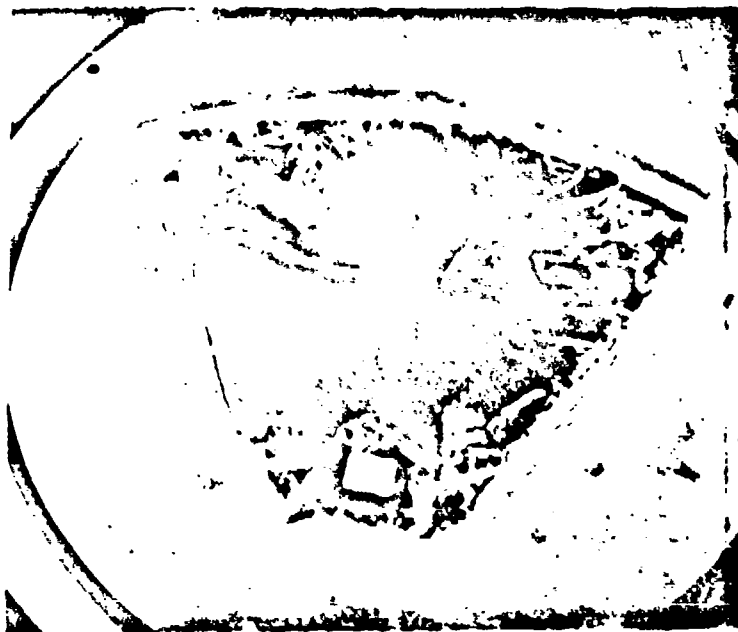


Figure 20. Glass Sector After Test.

As indicated in Figure 21, the finite-element prediction was conservative. The computations predicted failures in the range of 20 to 50 psig, whereas, experimental values ranged from 31 to 70 psig.

Prior experience with controlled defect studies had indicated that ZnSe could be represented by a volume-flaw model. Therefore, Equation (10) was employed to evaluate the Weibull parameters for ZnSe from the flexural test data. Unfortunately, attempts to adapt Equation (10) to the maximum likelihood three-parameter computer analysis, which had been successfully employed with the glass bar results, were fruitless. A simpler two-parameter analysis in which σ_u was assigned a value of zero was used. Further complications were encountered with the ZnSe data. Strength measurements have been accumulated for ZnSe from a number of different

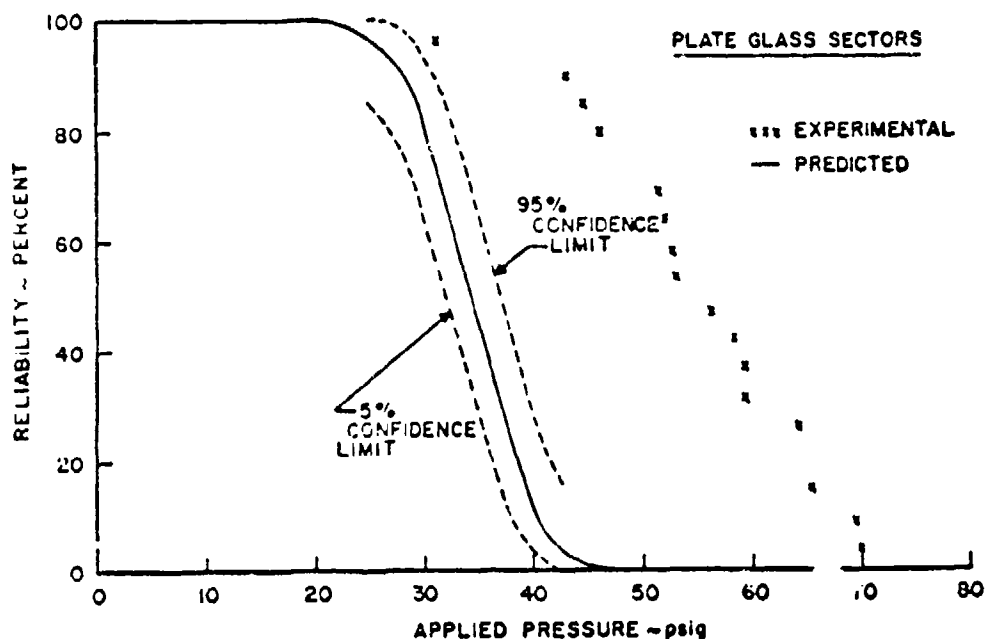


Figure 21. Reliability of Large 60° Glass Sectors Subjected to Uniform Pressure Loading.

production runs and in the course of this testing, a statistical characterization of good quality ZnSe has developed. By comparison, the twenty-four test bars from Run 113 were abnormally weak (see Table 4). Moreover, the Weibull parameters of the Run 113 material were also atypical. These differences are quite evident in the cumulative distribution curves of Figure 22. The "composite" ZnSe data formed a tight distribution about its calculated Weibull curve, whereas, the fit of the Run 113 data was much poorer. Weibull parameters for the two groups of data were as follows:

	<u>Run 113 ZnSe</u>	<u>"Composite" ZnSe</u>
m	3.878	7.970
σ_0	1.588 ksi	3.763 ksi
σ_u	0	0

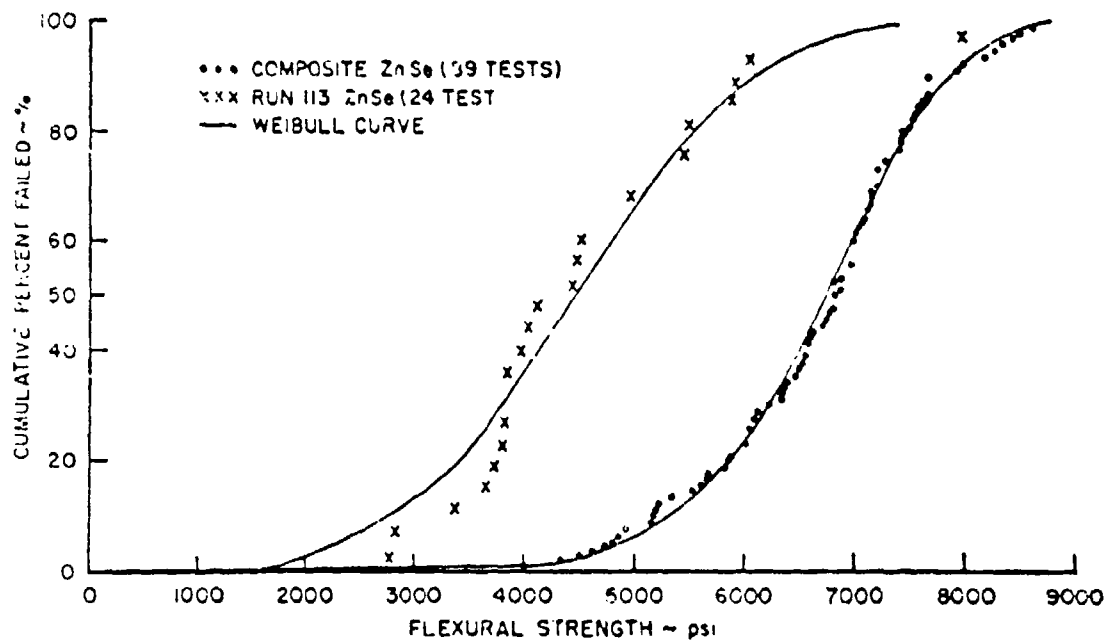


Figure 22. Cumulative Frequency Distributions for ZnSe Flexural Test Bars.

Both sets of Weibull parameters were employed to predict the reliability of pressure-loaded, 2-inch diameter ZnSe discs using Equation (20).

Pressure-burst tests were conducted on the twenty ZnSe discs using the same procedure employed with the glass discs. Times to failure were less than 20 seconds in every test. As shown in Figure 23, the experimental data were bracketed by the two predicted curves; the Run 113 Weibull parameters yielded conservative results, while the "composite" parameters led to a nonconservative prediction. Based on a sample size of 20, the 95% confidence bands of both predicted curves overlapped and, therefore, it was impossible with these few data points to determine which set of Weibull parameters more accurately represented the ZnSe discs.

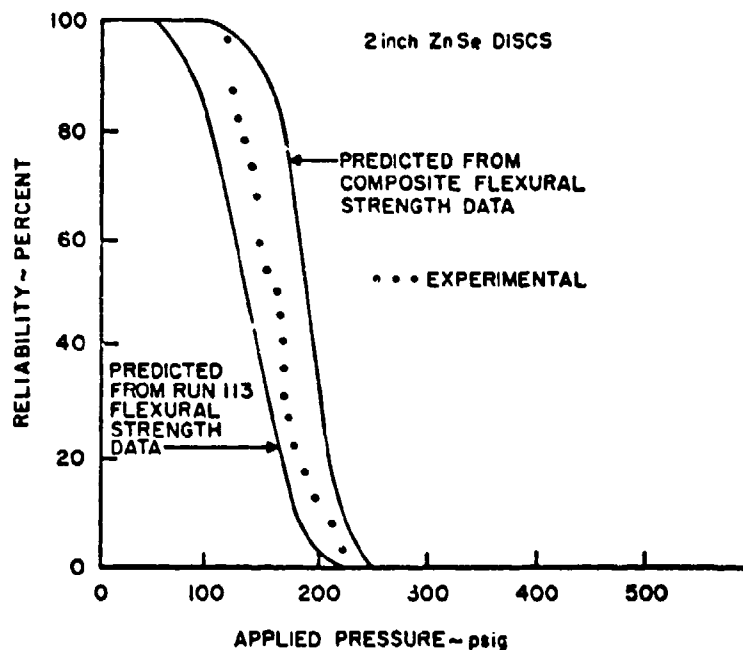


Figure 23. Reliability of Two-inch ZnSe Discs Subjected to Uniform Pressure Loading.

Conclusions

The predictions of structural behavior derived from laboratory test data, while not exact, were adequate for the purpose of identifying appropriate proof stress levels. The quantitative estimates of component performance which result from the Weibull/finite element analysis of laboratory test data provide assurance that a reasonable measure of the structural capacity of a brittle component can be experimentally demonstrated without excessive proof-test attrition.

3.1.2 Gould ZnSe

Three sets of ZnSe specimens produced by physical vapor deposition were submitted by Gould in the form of finished mechanical test bars nominally 2 x 7 x 30 mm. A pair of specimens from each of two process runs (333 and 358) and a six-specimen group from Run 459 were evaluated. The results of this evaluation are summarized in Table 11.

The PVD material had a large-grained, elongated microstructure (see Figure 24). The mean grain sizes of the 333 and 358 samples were 130 and 250 μm , respectively. Both sample sets contained internal pores 2 to 50 μm in diameter which produced a slight lowering of their bulk density.

Polished sections were not obtained for the 459 samples. These specimens had been heavily etched by Gould using a mixture of Br and methanol. The etchant clearly delineated the specimen microstructure (see Figure 24) which consisted of massive, heavily twinned grains in a columnar array 3 to 6 mm in length and 2 to 3 mm wide. The bases of the columnar grains were equiaxed and approximately 1.0 mm in diameter. The chemical etching of the 459 samples produced well rounded edges and corners. However, there was also surface roughening due to grain boundary penetration.

The orientation of the columnar grains in the 459 samples placed the maximum grain dimensions normal to the tensile stresses imposed by the flexure tests. This unfavorable microstructural orientation combined with the etchant surface damage was expected to result in very low strengths. As indicated in Table 11, however, the strength of these specimens was surprisingly high. Values ranged from 4.94 to 8.41 ksi and averaged 6.20 ksi.

Somewhat lower strengths were measured for the other two specimen sets (333 and 358) even though they had a finer grained microstructure and smoother surface finish.



Specimen 333 (75X)



Specimen 358 (100X)



Specimen 459

Figure 24. Representative Microstructure of Gould PVD ZnSe.

TABLE 11. SUMMARY OF TEST RESULTS FOR GOULD ZnSe

	Sample Number		
	333	358	459
Density at R. T. (gm/cc)	5.25	5.24	5.27
Ultimate Strength at. R. T. (ksi)	5.56*	4.09*	6.20**
Knoop Hardness- 50 gm load (kg/mm ²)	125	131	---
Mean Grain Size (μ m)	130	250	3000
Resistivity at 300°K (ohm-cm)	---	3×10^{10}	2×10^{11}

* Average of two tests.

** Average of six tests.

The electrical resistivity of the 358 and 459 samples exhibited an intrinsic temperature dependence at elevated temperatures with an energy gap nearly equal to that of pure ZnSe (2.45 ev). However, with decreasing temperatures below 200 to 300°K, the resistivity behavior of both samples indicated the presence of extrinsic free carriers, probably from impurities. As is evident in Figure 25, the resistivity of the Gould material fell midway between the values obtained for "as-deposited" and annealed CVD ZnSe from Raytheon.

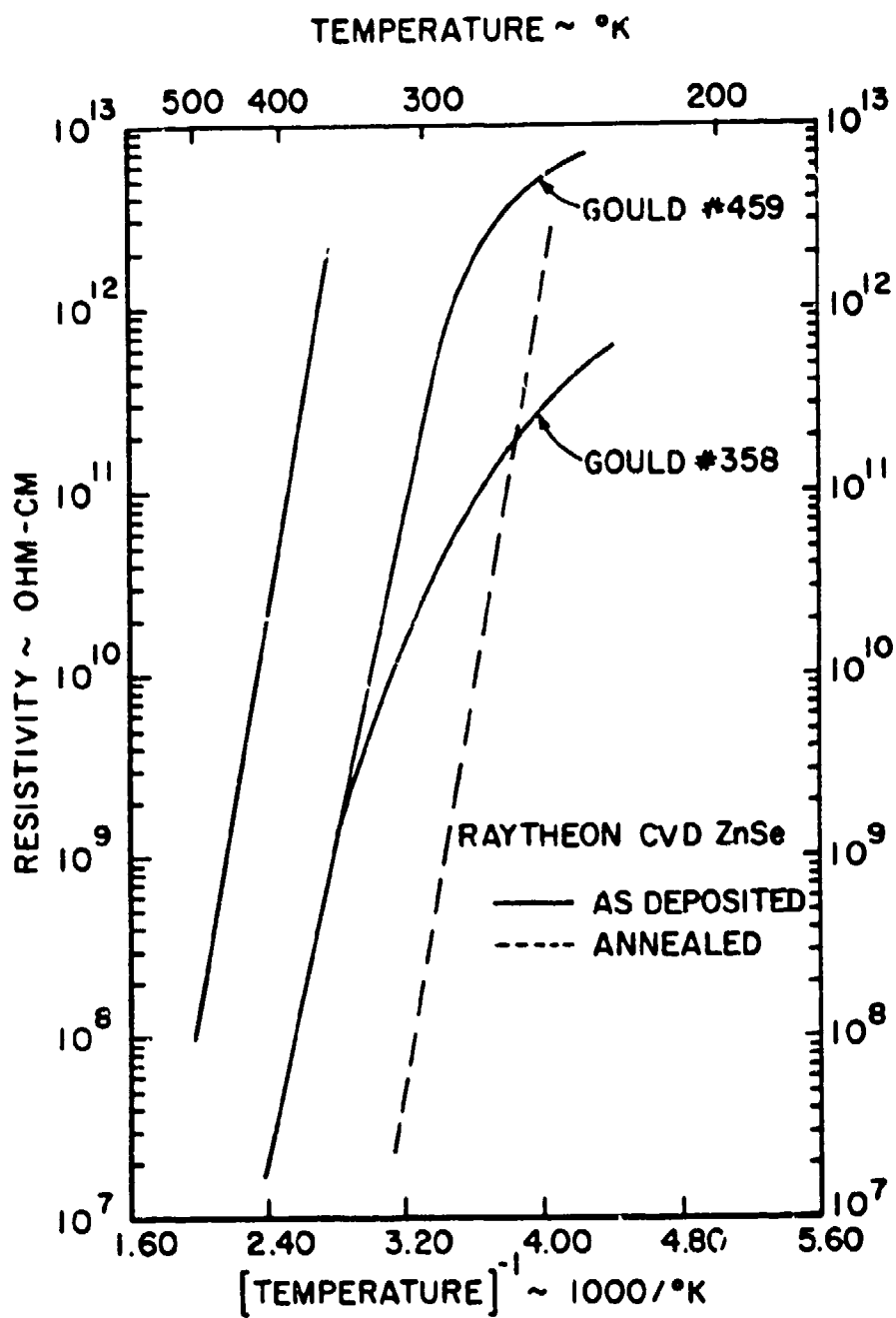


Figure 25. Electrical Resistivity of Gould ZnSe.

3.1.3 Coors ZnSe

Three polycrystalline ZnSe discs, 38 mm in diameter and 6 mm thick, fabricated by Coors using a hot pressing technique were evaluated. The results of this evaluation are summarized in Table 12.

This material had a large-grained, equiaxed, microstructure with the pronounced twinning typical of ZnSe. The polished section of Sample 105 shown in Figure 26 is representative of this sample group. Scanning electron microscopy of the fracture surface of Sample 105 revealed a few pores 2 to 4 μm in diameter. This minor porosity could explain the slightly lowered density of this sample. The specific heat and thermal expansion coefficient values of the Coors material were 0.085 cal/gm $^{\circ}\text{C}$ and 8.1×10^{-6} cm/cm $^{\circ}\text{C}$ respectively. These are normal values for ZnSe. The room temperature thermal diffusivity value of 0.112 cm²/sec was approximately 10% larger than that obtained for ZnSe from other suppliers.

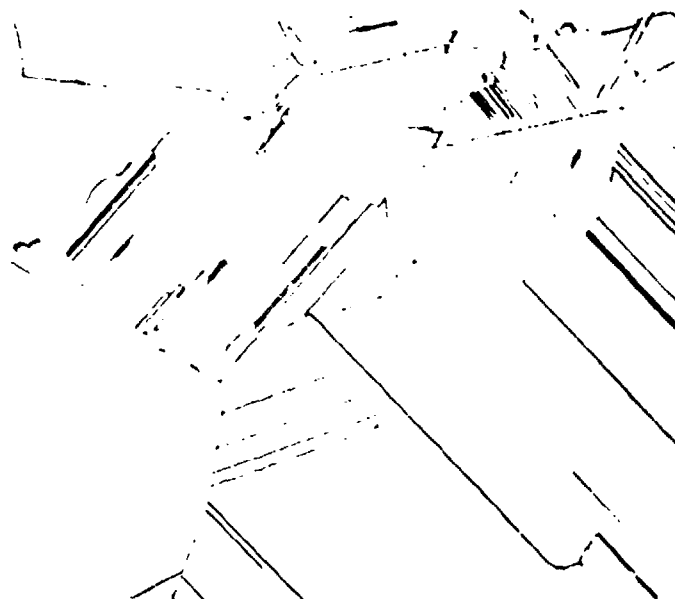
The hardness of the Coors material averaged 135 kg/mm² which was somewhat higher than the 100 to 120 kg/mm² values usually obtained for ZnSe.

Flexural strength measurements were confined to three tests which yielded values in the range of 2.50 to 3.72 ksi. Fracture occurred in a brittle fashion by transgranular crack propagation with no evidence of yielding.

The electrical resistivity of the Coors material was on the order of 1×10^{12} ohm-cm at 78 $^{\circ}\text{K}$ and exceeded 5×10^{10} ohm-cm at 300 $^{\circ}\text{K}$. Specimen currents were too low to obtain reliable Hall measurements.

TABLE 12. SUMMARY OF TEST RESULTS FOR COORS ZnSe

	Sample Number		
	47	104	105
Density (gm/cc)	5.26	5.26	5.23
Specific Heat at 10°C (cal/gm°C)	0.085	0.084	0.086
Ultimate Strength at Room Temperature (ksi)	3.53	2.50	3.72
Knoop Hardness-50 gm load- at Room Temperature (kg/mm ²)	151	130	125
Average Grain Size (microns)	415	395	495
Coefficient of Thermal Expansion-25° to 200°C (cm/cm°C x 10 ⁻⁶)	8.5	7.7	8.1
Resistivity at 300°K (ohm-cm)	4.2 x 10 ¹⁰	8 x 10 ¹⁰	7.5 x 10 ¹⁰
Thermal Diffusivity at Room Temperature (cm ² /sec)	---	---	0.112



Polished Section (75X)



SEM (800X)

Figure 26. Typical Polished Section and Scanning Electron Micrograph of Coors ZnSe Sample 105.

3.1.4 Gould CdTe

Specimens of CdTe from Gould were submitted for evaluation, usually in the form of discs approximately 50 mm in diameter and 6 mm in thickness. These discs were formed by physical vapor deposition of high purity CdTe typically doped with 10 ppm of Ga. The dopant, in combination with post-deposition heat treatment in Cd and Te vapors, was intended to produce a high resistivity n-type semiconductor.

The Gould CdTe was dense, virtually pore-free material of essentially theoretical density (5.86 gm/cc). The discs were polycrystalline with grain sizes in the range of 0.5 to 3.0 mm.

Specimens from seven different process runs were evaluated. These data are summarized in Table 13. Two sets of specimens (No. 357 and No. 459) were submitted by Gould in the form of finished test bars 2 x 6 x 32 mm. The remaining specimens were machined from discs by UDRI personnel.

These CdTe specimens, as well as those from other suppliers, were difficult to finish to a flawless condition. With the exception of the six No. 459 specimens, the flexural strength specimens failed in a brittle fashion by transgranular fracture at ultimate strengths ranging from 1.8 to 3.2 ksi. Gould employed a chemical polish on the No. 459 specimen to obtain an exceptionally smooth surface finish with well-rounded corners and edges. These were the strongest CdTe specimens evaluated and the only ones to exhibit a yield point.

The Knoop hardness of the Gould CdTe generally varied from 55 to 65 kg/mm with one specimen, No. 357, inexplicably having a hardness value of 88 kg/mm².

TABLE 13. SUMMARY OF PROPERTY MEASUREMENTS OF GOULD CdTe

	Sample Numbers						
	44	87	88	155	333	357	459
Density (g/cm ³)	5.85	5.86	5.86	5.86	---	5.87	5.87
Knoop Hardness-50 gm load (kg/mm ²)	---	---	61	---	65	88	55
Mean Grain Size (μ m)	---	---	3000	---	~1000	---	500-1000
Ultimate Strength (ksi)	---	---	3.21	---	1.80	2.93	3.88*
Yield Strength (ksi)	---	---	none	---	none	none	3.15*
Young's Modulus (psi $\times 10^6$)	---	---	5.4	---	---	---	---
Specific Heat at 10°C (cal/gm°C)	0.055	0.053	0.052	0.053	---	---	---
Thermal Diffusivity at Room Temperature (cm ² /sec)	---	0.056	---	0.0470	---	---	---
Thermal Conductivity at Room Temperature (cal/sec cm°C)	---	---	---	0.0146	---	---	---
Avg. Coefficient of Thermal Expansion-20 to 200°C (cm/cm°C $\times 10^{-6}$)	4.4 4.4	4.3	4.7	---	---	---	---
Electrical Resistivity (ohm-cm) at 78°K	3 $\times 10^6$	1.4 $\times 10^7$	2 $\times 10^3$	---	---	8 $\times 10^5$	6 $\times 10^8$
at 300°K	1 $\times 10^4$	2.6 $\times 10^4$	2.7 $\times 10^2$	---	---	9 $\times 10^2$	2 $\times 10^3$
Carrier Type	n	n	p-n	---	---	n	n

* Average of six tests.

Horrigan and Rudco⁽¹³⁾ reported values of specific heat, Young's modulus, and thermal expansion coefficient for CdTe as 0.05 cal/gm °C, 5.3×10^6 psi, and 4.5×10^{-6} cm/cm °C, respectively. The Gould material had virtually identical values for these properties.

A thermal diffusivity of $0.056 \text{ cm}^2/\text{sec}$ at room temperature was obtained for Sample 87 early in the evaluation program. Later, as the measurement technique was refined and test equipment improved, a room temperature value of $0.0470 \text{ cm}^2/\text{sec}$ was obtained with Sample 155. Measurements of specific heat and thermal diffusivity with Sample 155 were also taken over the temperature range of -50° to $+200^\circ\text{C}$. These data and the derived values of thermal conductivity are presented in Figure 27.

The electrical resistivity of the Gould CdTe varied significantly from sample to sample. As is evident in Figure 28, this variability was especially apparent at low temperatures; the high temperature resistivity values tended to converge at elevated temperatures.

The highest resistivity values were displayed by Sample 459 which exhibited an intrinsic temperature dependence with an energy gap virtually identical to that of pure CdTe (1.45 ev).

Hall coefficient measurements were rather erratic but did indicate that, except for Sample 88, all of these samples were n-type semiconductors. The determination of carrier type was confirmed with hot probe measurements. Sample 88 exhibited sharp transition from p to n-type conductivity as the temperature increased above 128°K .

(13) F. A. Horrigan and R. I. Rudco, "Materials for High Power CO₂ Lasers," Raytheon Company Final Report on Contract DA-AH01-69, C-0038, September 1969.

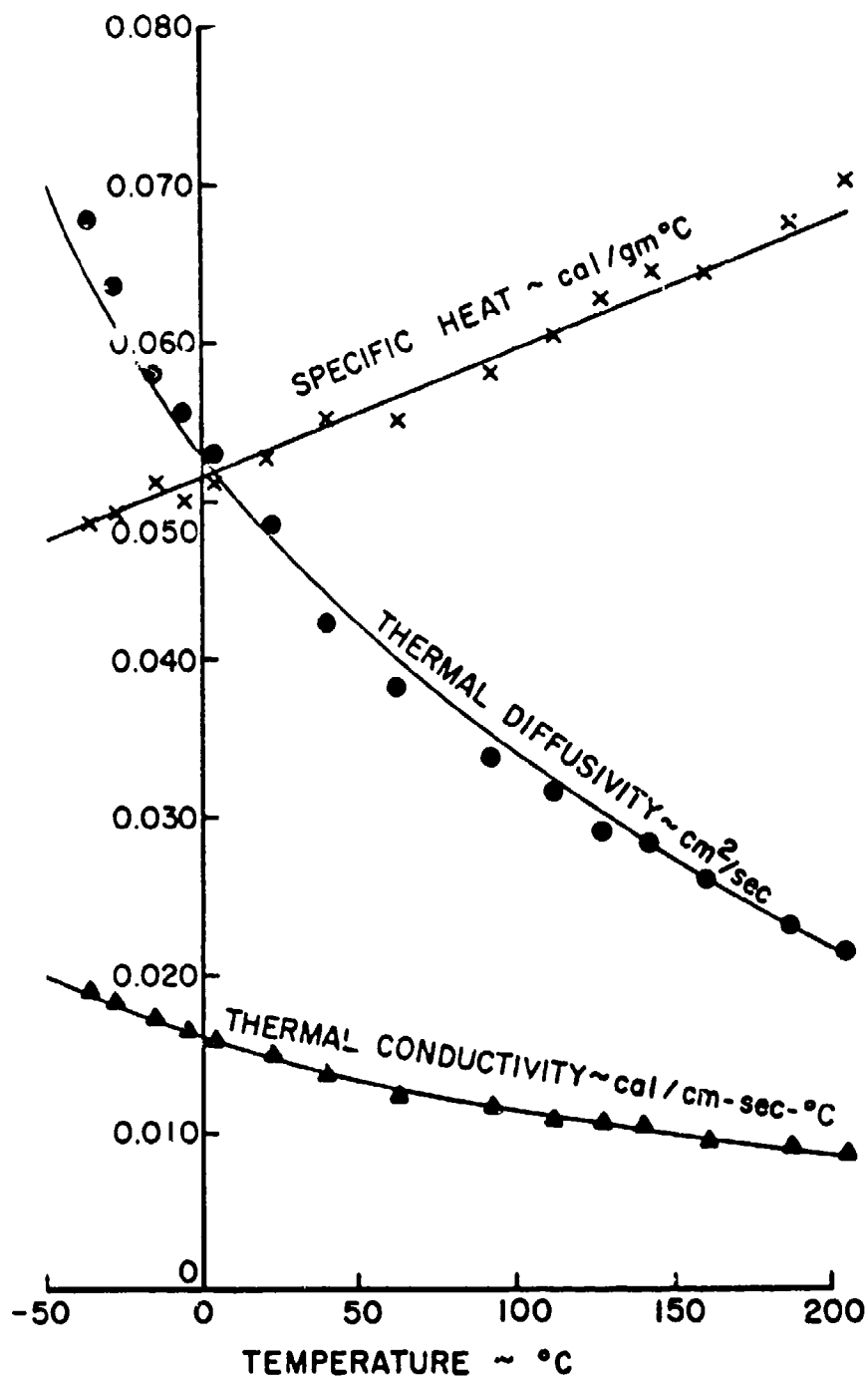


Figure 27. Thermal Properties of Gould CdTe.

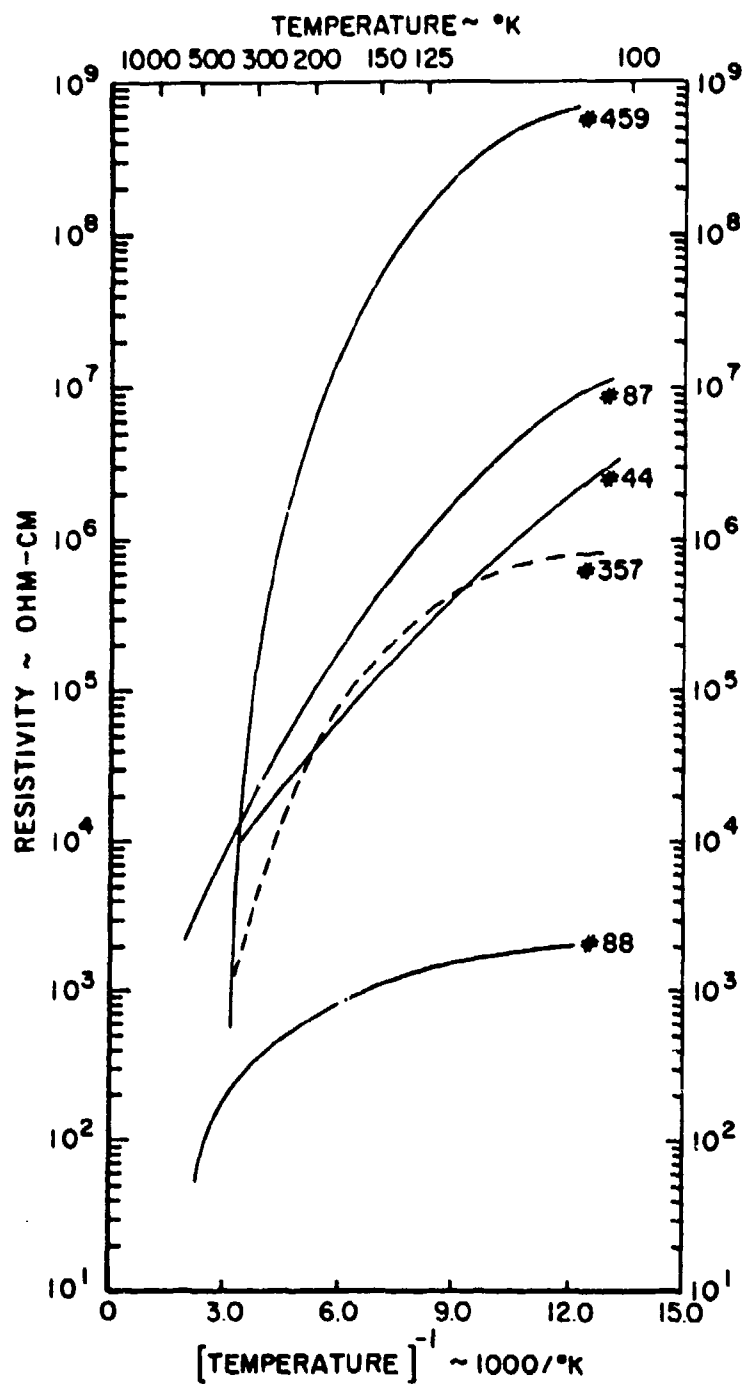


Figure 28. Electrical Resistivity of Gould CdTe.

3.1.5 Tyco CdTe

Two samples of Tyco CdTe designated as Runs 74 and 75 were submitted for evaluation in the form of polycrystalline discs 50 mm in diameter and 6 mm thick. These samples were fabricated by "sonic casting", a process whereby high purity CdTe was melted and subjected to an ultrasonic vibratory field while cooling in an attempt to induce the formation of a fine-grained polycrystalline solid.

The material received from Tyco had very large grains ($\sim 3000 \mu\text{m}$). One side of each sample had several clusters of surface connected pores 1 to 3 mm in diameter. There was minor internal porosity in both samples, but not enough to significantly lower their bulk density.

A summary of the test results obtained with the two Tyco samples is given in Table 14.

This was a typically soft material with the relatively low strength associated with large-grained CdTe. Normal values of specific heat and thermal expansion coefficient were obtained with this material. Resistivity values were not particularly large (see Figure 29) and both samples were p-type semiconductors.

TABLE 14. SUMMARY OF PROPERTY MEASUREMENTS OF TYCO CdTe

	Sample Number	
	74	75
Density (gm/cc)	5.86	5.83
Knoop Hardness- 50 gm load (kg/mm)	64	62
Mean Grain Size (μm)	~3000	~3000
Ultimate Strength (ksi)	2.28	1.68
Specific Heat at 10°C (cal/gm°C)	0.052	0.055
Coefficient of Thermal Expansion (cm/cm°C)	4.4	4.6
Electrical Resistivity (ohm-cm) at 78°K	3×10^4	---
at 300°K	2×10^3	1.6×10^3
Carrier Type	p	p

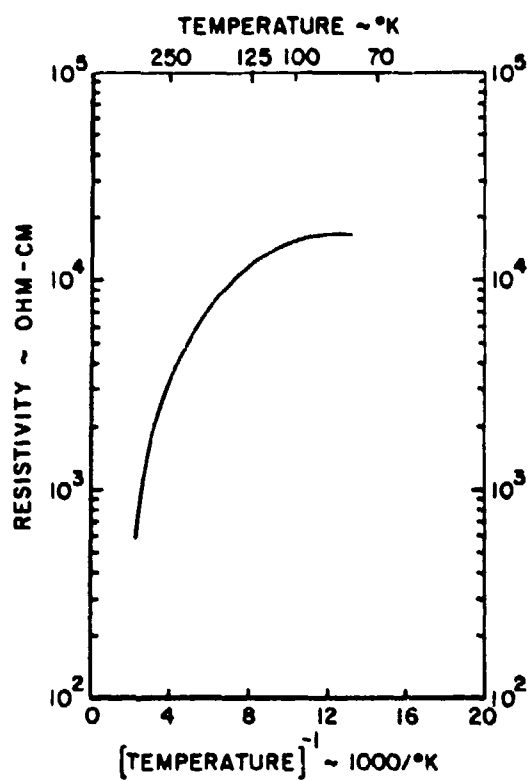


Figure 29. Electrical Resistivity of Tyco CdTe.

3.1.6 Hughes CdTe

Two disc shaped specimens (approximately 33 mm in diameter and 2 mm thick) from Hughes were evaluated. This was an In doped CdTe produced in a large grained polycrystalline form by a modified Bridgeman technique. The process included a special thermal anneal to obtain a high resistivity n-type semiconductor.

These samples were fully dense and of normal hardness. The specific heat and thermal diffusivity values of the Hughes material were comparable to those obtained for CdTe from other suppliers. A summary of these measurements is given in Table 15.

Sample 38 was a p-type semiconductor of moderately high resistivity. Sample 175 was n-type and as is evident in Figure 30, had a significantly larger low-temperature resistivity than Sample 38.

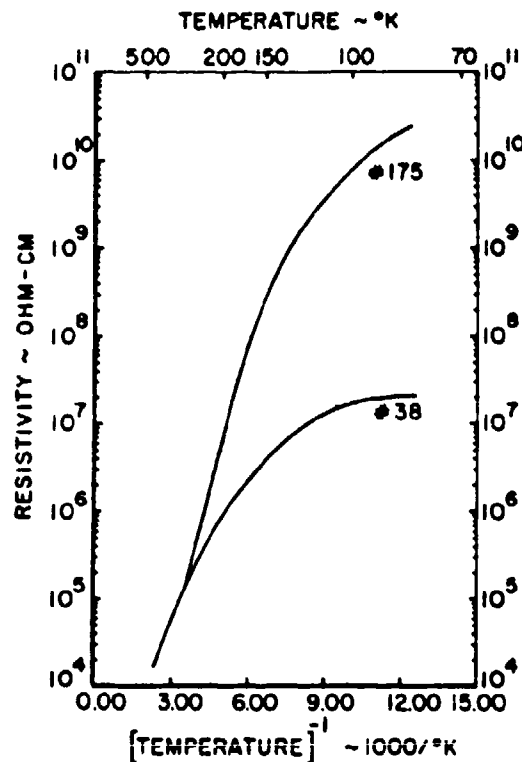


Figure 30. Electrical Resistivity of Hughes CdTe.

TABLE 15. SUMMARY OF PROPERTY MEASUREMENTS
OF HUGHES CdTe

	Sample Number	
	39	175
Density (gm/cc)	5.83	5.86
Knoop Hardness-50 gm load (kg/mm)	65	---
Specific Heat at 10°C (cal/gm °C)	---	0.053
Thermal Diffusivity (cm ² /sec)	0.042	---
Electrical Resistivity (ohm-cm) at 78°K	2x10 ⁷	2x10 ¹⁰
at 300°K	1x10 ⁵	2x10 ⁵
Carrier Type	p	p

3. 1. 7 Grain Boundary Effects in CdTe

Electrical measurements of polycrystalline CdTe were characterized by marked anomalies, nonlinearity, and specimen-to-specimen variability. Sample cleaning procedures and the ohmic character of the ultrasonically soldered specimen contacts were evaluated and eliminated as major causes of these difficulties. Some improvement was realized with a redesign of the specimen holder to minimize convective thermal gradients in the dewar at the sample position; but unusual electrical behavior persisted. It was noted that electrode placement was often quite critical and offset voltages frequently were quite large when oppositely placed contacts occupied different grains. Grain boundaries were therefore suspected to be at least partially responsible for the erratic behavior. Accordingly, an investigation was initiated to evaluate the influence of grain boundaries upon the resistivity and photoconductive response of several CdTe samples from various suppliers.

Grain boundary resistance effects were evaluated by ultrasonically soldering rows of indium dots at one millimeter spacing on several samples of CdTe. A voltage was impressed across these samples and the potential at each solder dot was then measured with respect to one end of the sample using a high impedance voltmeter.

Typical data obtained with the technique are shown in Figure 31, a plot of potential as a function of specimen position for a bicrystal of Tyco No. 75 CdTe. As the grain boundary was traversed, a voltage drop exceeding 95% of the applied potential occurred. Similar results for Tyco No. 74 and Gould No. 44 CdTe samples are presented in Figure 32. Several grains were traversed in the Tyco No. 74 sample which produced the series of sharp breaks in the potential plot. The linear resistance change across the grain boundary of Gould No. 44 at an impressed potential of 100 volts proved to be the result of dielectric breakdown between solder dots, a phenomenon not observed at 1 and 10 volts. Grain boundary resistance effects were

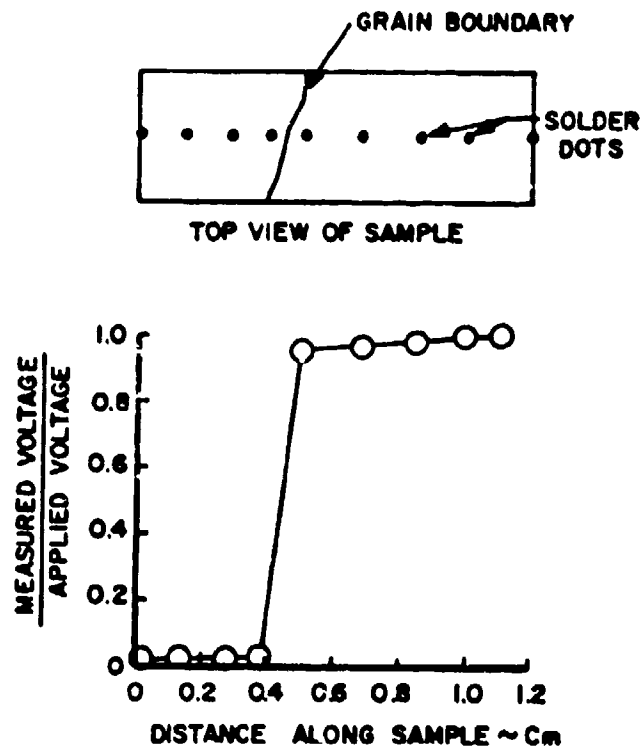


Figure 31. Grain Boundary Resistance Measurements of a Tyco 75 CdTe Bicrystal.

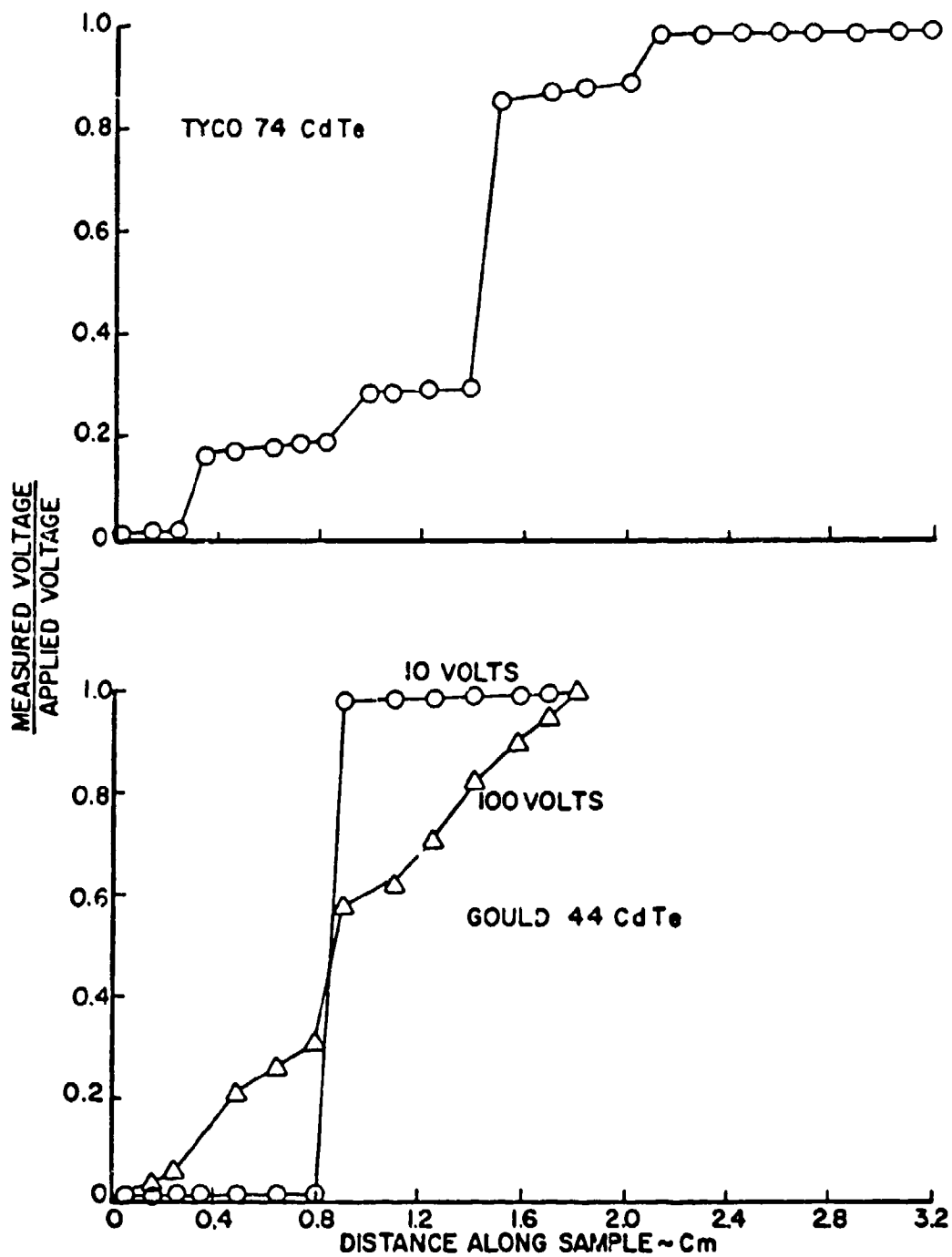


Figure 32. Grain Boundary Resistance Measurements of Tyco 74 and Gould 44 CdTe Samples.

observed only with high angle boundaries; twin boundaries had the same resistivity as the bulk material.

To further characterize the electrical behavior of grain boundaries in CdTe and to facilitate a more rapid evaluation of samples, the photoconductive response of this material was investigated. To accomplish this, bar-shaped specimens were electroded on either end and irradiated with a He-Ne laser. The current generated by the laser beam was recorded as a function of beam position on the sample. Initially, samples were mounted on the pen holder of an x-y recorder. The vertical position of the sample with respect to the laser beam was adjusted using the y-axis zero control. A scan-ramp voltage generator drove the x-axis at a uniform rate to translate the sample across the laser beam. The photovoltage signal excited by the laser beam was amplified with an electrometer and displayed on the y-axis of this recorder to obtain a photovoltage-position record. This system provided acceptable resolution but was subject to excessive background noise. Ultimately, a precision micrometer stage driven by an adjustable synchronous motor was used to translate the specimen across the laser beam. A gear-coupled 10-turn potentiometer was employed to obtain a voltage signal proportional to sample position. A 10X objective lens was used to focus the laser beam to a spot size less than 0.1 mm in diameter. This modified experimental arrangement which is diagrammed in Figure 33 proved quite satisfactory.

Photoresponse measurements were performed on the same Tyco No. 75 sample which had been used in the potential drop measurements. As evident in Figure 34, when the laser beam crossed the grain boundary in this sample, a positive and negative photovoltage spike was produced. It was observed that ambient light would shift the base line of the photoresponse but would not alter its form. When a bias voltage was applied, sample current peaked sharply but did not change sign as the grain boundary was crossed by the laser beam.

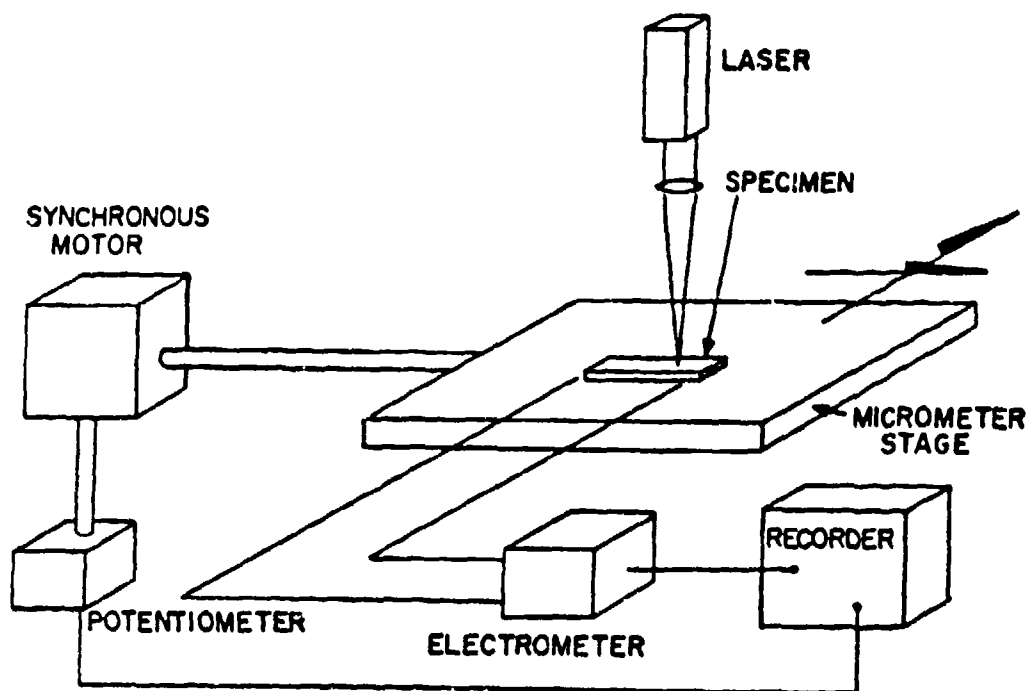


Figure 33. Experiment Arrangement for Photoresponse Measurements of Polycrystalline CdTe.

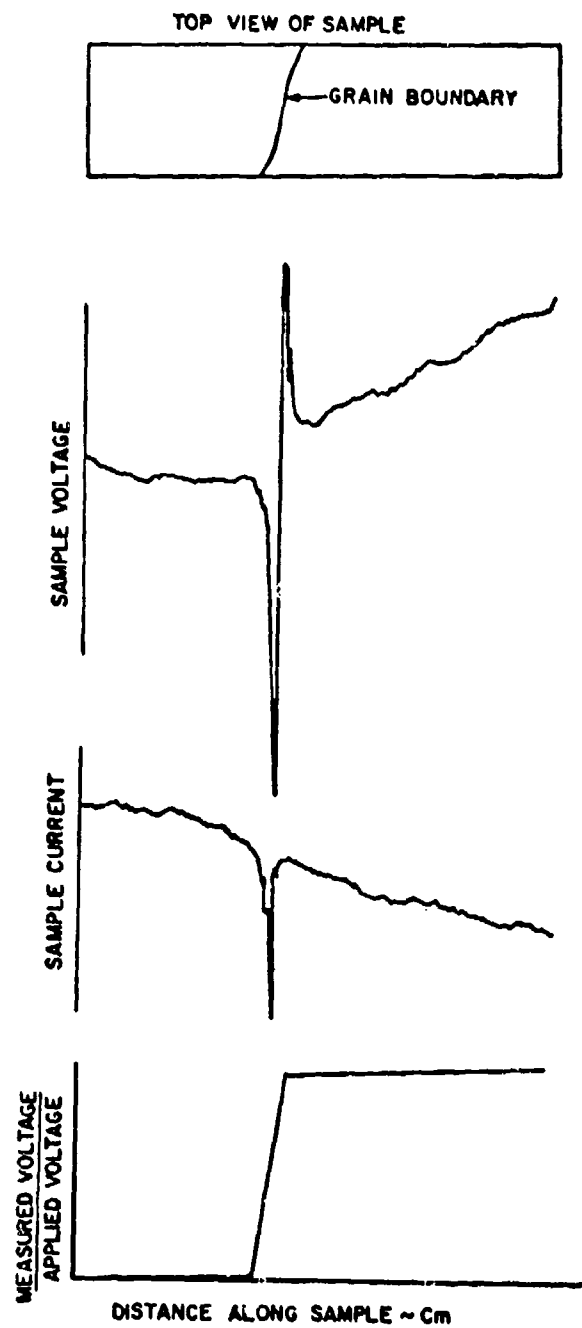


Figure 34. Photovoltage, Photocurrent, and Resistivity Measurements of a Tyco 75 CdTe Bicrystal.

The Tyco No. 75 sample received no special preparation. An as-cut surface was used which was sufficiently smooth to discern the boundary as a difference in reflectivity between adjacent grains. As these studies progressed, a sample of Tyco No. 74 CdTe was polished and lightly etched to clearly delineate the location of all grain boundaries. Laser scans were taken across this sample and as indicated in Figure 35, the photoresponse corresponded quite well with the position of high angle grain boundaries. The grain boundary spikes were superimposed on a uniformly changing background which contained a number of small signals apparently uncorrelated with the sample microstructure. The background noise behavior is not understood but may be due to grain boundary orientation. The small signals are thought to be due to equipment noise and scattering from the non-planar surface of the specimen.

A marked sensitivity to specimen surface roughness would be anticipated since CdTe is opaque at this laser wavelength and the penetration distances are therefore quite small. The influence of surface condition upon the photoresponse of CdTe was qualitatively evaluated with a sample of Gould 44. A bicrystal of this material in the as-cut condition produced a very strong photosignal as the grain boundary was traversed. The sample was subsequently etched in a mixture of nitric and hydrofluoric acids until the grain boundary was no longer visible. In this over-etched condition, the photosignal at the grain boundary was barely detectible above a very large noise background presumably produced by surface scattering of the incident laser beam. This simple experiment illustrated the necessity for a fairly smooth surface. It is not necessary, however, to have an optically flat polish; if grain boundaries can be visually observed, then decent photo-response measurements can be obtained.



TYCO 74 CdTe



VISUAL MAPPING OF HIGH ANGLE GRAIN BOUNDARIES
SHOWING LASER SCAN PATHS

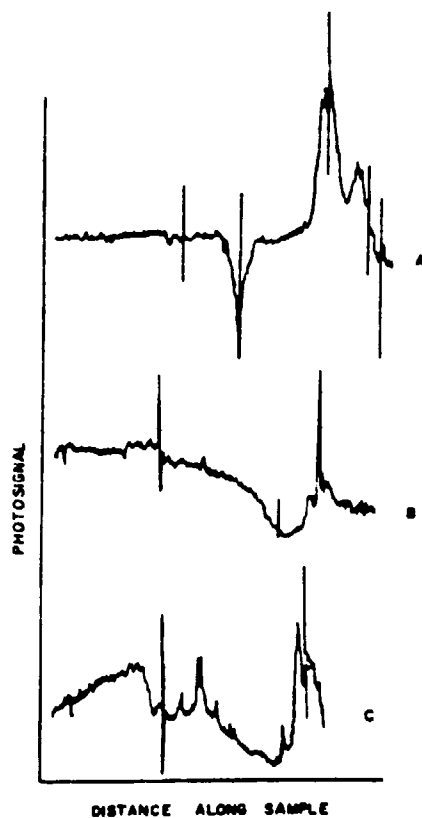


Figure 35. Photoreponse Scans of Polycrystalline Tyco 74 CdTe.

3.1.8 A Proposed Grain Boundary Model for CdTe

• Experimental data indicate that grain boundaries exert a significant influence upon the electrical behavior of polycrystalline CdTe. The infrared transmission properties may also be affected by the presence of these grain boundaries and thus an evaluation of grain boundary models in semiconductor materials was considered appropriate.

No studies of grain boundary effects in CdTe were found in a preliminary review of the literature. As expected, a substantial amount of work has been done in this area with germanium.⁽¹⁴⁾ The model which has emerged from these studies is generally in accord with experimental observations of CdTe.

In the germanium model, grain boundaries are treated as a plane of edge dislocations such as depicted in Figure 36. Each dislocation is assumed to form a free or dangling bond with acceptor characteristics and an energy level below the Fermi level of the n-type host. The acceptor character of these dislocations was inferred from experimental observations of a decrease in the negative charge carrier population as the dislocation population of a single crystal is increased via plastic deformation.

If free electrons combine with the acceptors to form a double dangling bond, a space charge build-up occurs which repels other electrons. If the wave functions of the bond levels overlap (and this appears to be the case with high angle grain boundaries) charge pipes form. In this situation, the grain boundary region can be treated as an n-p-n junction. The area around the dislocation sites behaves as p-type material collecting electrons from adjacent n-type regions to form depletion layers to either side of the dislocation such as illustrated in the schematic band diagram of Figure 37.

(14) Herbert F. Matari, Defect Electronics in Semiconductors, Wiley-Interscience, New York, 1971.

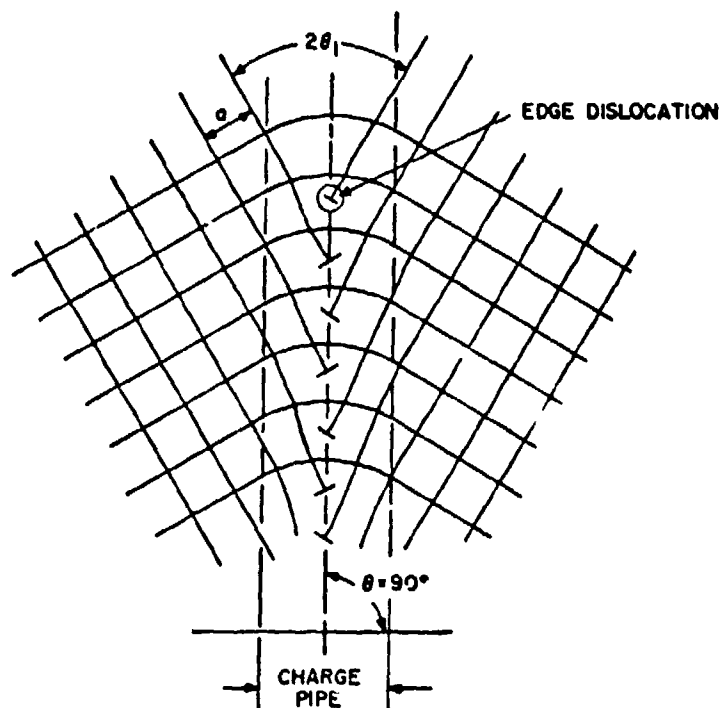


Figure 36. Dislocation Model of a Grain Boundary (after Matari).

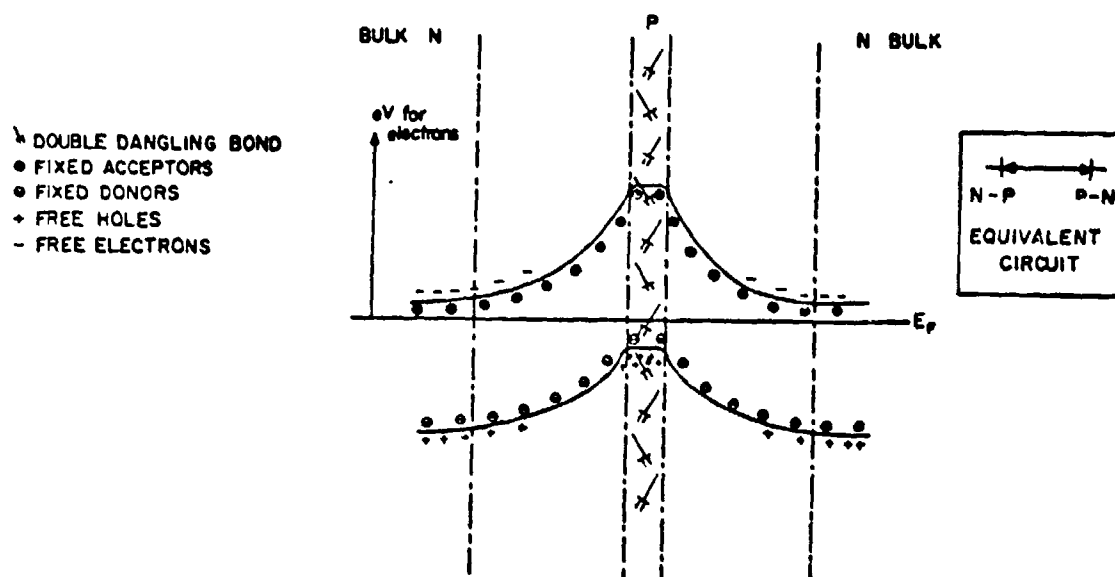


Figure 37. Energy Band Model of a Grain Boundary and its Equivalent Electrical Circuit (after Matari).

The effects noted in CdTe can be interpreted according to the band diagram and circuit of back-to-back diodes of Figure 37. For example, d. c. measurements will always show a large potential drop across a grain boundary regardless of the polarity of the applied potential since one side of the grain boundary will always be reverse biased and thereby introduce a large series resistance in the circuit. The photoresponse of CdTe can also be interpreted with this model. With no bias applied to the sample, electron hole pairs will form when the region to the left of the grain boundary is irradiated with light at a wavelength exceeding the band gap energy. The electrons will be driven to the left and the holes to the right by the potential gradient. The directions of electron and hole drift will reverse as the right side of the grain boundary is irradiated. Thus, as the beam is swept across the grain boundary, a reversal in the photoresponse should be observed.

External bias of the sample will effectively eliminate the potential gradient on one side of the grain boundary so that only the opposite side of the boundary is reverse biased. Only one side will exhibit electron-hole transport and thus no current reversal will occur as the laser beam traverses the grain boundary. This model also predicts that illumination of the sample with ambient white light will produce a background signal superimposed upon the laser-induced signal.

The experimentally observed photoresponse behavior of polycrystalline CdTe seems to be explained by the germanium model. The experimental data does not exhibit the symmetry across grain boundaries that would be anticipated but this is probably due to misorientation of the grain boundaries with respect to the laser beam.

The majority of electrical measurements with CdTe have been made with the current flow perpendicular to the grain boundaries. Electrical measurements down the grain boundaries of germanium have shown that the region within a grain boundary has a significantly lower resistance than the bulk material. Preliminary measurements indicate that this is also true for polycrystalline ZnSe.

3.1.9 Summary of the II-VI Compounds

3.1.9.1 ZnSe

The hot pressing procedure employed by Coors and Gould's physical vapor deposition technique produced laboratory size specimens of relatively coarse grained polycrystalline ZnSe with slight amounts of residual porosity.

The chemical vapor deposition process developed by Raytheon produced large slabs of fully dense, fine-grained material suitable for direct fabrication into full size operational hardware. Early problems with metallic zinc and ZnSe dust inclusions were eliminated by process refinements. However, a banded haziness, believed to be microporosity, has continued to occur on an intermittent basis in some process runs.

The primary differences among the three ZnSe materials were their electrical and mechanical properties, both of which were related to microstructural factors.

Electrical measurements of fine-grained "as deposited" CVD ZnSe and annealed CVD ZnSe with a very coarse microstructure revealed an inverse relationship between electrical resistivity and mean grain size. This relationship was corroborated with similar measurements of coarse grained PVD ZnSe. Thus, high values of electrical resistivity in polycrystalline ZnSe (or CdTe) are not necessarily indicative of a low concentration of infrared absorbing free carriers, but rather a measure of the degree to which any free carriers have been immobilized by the presence of an array of current-blocking grain boundaries. Therefore, high electrical resistivity does not necessarily insure low infrared absorbance.

The increase of strength with decreasing grain size observed with ZnSe is consistent with the general behavior of polycrystalline materials. Moreover, since ZnSe is a brittle material, a statistical variation in strength had been anticipated.

The presence of massive inclusions (Run 60 material) or visible surface cracks due to improper finishing significantly weakened ZnSe. Elimination of the inclusions and improvements in specimen surface finish produced significant strength increases. However, beyond a certain level of surface quality, a strength plateau was reached, presumably at the transition from surface-flaw to volume-flaw failure initiation.

A homogeneity analysis of a single large plate of CVD ZnSe indicated that within the statistical precision of the evaluation, the plate was spatially homogeneous with respect to its thermal and mechanical properties. The strength of the material was unaffected by specimen orientation despite a preferred growth direction. Varying strain by a factor of 10^3 had no effect on strength. Young's modulus exhibited an expected decrease with increasing temperature over the range of -55°C to $+65^{\circ}\text{C}$. A similar variation of strength over this temperature range was obscured by statistical variations in the test results.

Proof testing at very large proof loads and a series of preliminary static load tests provided evidence that ZnSe is susceptible to environmentally assisted slow crack growth with water as the corrosive medium. The absence of a significant strain-rate dependence in this material and the repeated observance of run-out in fatigue tests would indicate that slow crack growth is not a potent phenomena in ZnSe. It has not been established that slow crack growth is an operative failure mechanism in the stress-time regime of laser window applications. Nevertheless, the potential for such a problem should be recognized and situations involving the prolonged exposure of components to a combined input of stress and a moist environment should be avoided.

The experiments involving validation of the combined Weibull-finite element analyses indicate that the predictions of large component structural behavior derived from laboratory test data, while not exact, were adequate for the purpose of identifying appropriate proof stress levels.

The quantitative reliability estimates which result from this analysis provide assurance that a reasonable measure of the structural capacity of a brittle component can be experimentally demonstrated without excessive proof test attrition.

3.1.9.2 CdTe

The evaluation of CdTe was confined to tests of research quantities of material produced by three different processes; physical vapor deposition, sonic casting, and a modified Bridgeman technique.

All three processes resulted in coarse-grained polycrystalline material with grain sizes on the order of 0.3 to 3.0 mm. Fabrication of mechanical test bars was complicated by the pronounced tendency of CdTe to chip and crack even with gentle wire sawing. The gage sections of the test bars usually consisted of one or two large grains and thus the strength data for this material is probably more representative of the single crystal cleavage strength of edge-flawed specimens. Undoubtedly fine-grained, well-polished samples of CdTe would exhibit much higher strengths.

Dopants and special thermal anneals were employed as part of the fabrication processes to obtain high resistivity CdTe; these strategies were not always successful as was evident in the low resistivity values obtained with the Tyco CdTe and the specimen to specimen variations of resistivity and charge carrier sign observed with the Hughes and Gould material.

Grain boundaries were found to exert a pronounced influence on the electrical behavior of polycrystalline CdTe. The electrical property data presented herein represent a combination of bulk and grain boundary resistivity values and as such would be sensitive to microstructural alterations.

3.2 ALKALI HALIDES

3.2.1 Honeywell Alkali Halides

Alkali halides press forged by Honeywell from starting material provided by Optovac and Harshaw were evaluated. Alloyed and unalloyed samples of KCl, KBr, and NaCl were included in this evaluation which consisted of measurements of flexural strength, hardness, and microstructural characteristics and, to a limited extent, measurements of thermal expansion, thermal diffusivity, thermal conductivity, specific heat, and precision lattice constants.

In reviewing these data, it should be recognized that these alkali halide materials were produced over a 12-month period under a continuing Air Force sponsored effort.* The reported data are the product of more than 200 experimental forgings intended to define optimal techniques for the fabrication of strong, high quality, polycrystalline, optical materials. Generally, only one or two specimens of each forging were available for evaluation and, consequently, there was no opportunity to establish a statistical basis for inherently variable properties such as ultimate strength. Even though only research quantities of material were available for evaluation, progress in the achievement of higher strength materials should have been apparent in a chronological listing of the properties of forgings as they were produced since the inception of the Honeywell program. Accordingly, in the presentation of the mechanical properties for the Honeywell material, these data were listed in the order in which the forgings were made. While not all forging experiments were equally successful and optimization did not proceed in all cases in a smooth progression, general trends in the progress of the Honeywell program were apparent in the data listings.

* Air Force Contract F33615-72-C-2019, "Halide Material Processing for High Power, Infrared Laser Windows," Honeywell, Inc.

In the interpretation of the room temperature mechanical property data for these alkali halide materials, it should be noted that while most of the specimens did exhibit a yield point, fracture ultimately occurred in a brittle fashion by catastrophic extension of critically-sized flaws. These strength limiting flaws can have several origins; they can develop during and after the press forging operation as a consequence of excessive cooling rates, residual stresses, etc.; flaws can be introduced during the cutting and finishing operations associated with the preparation of mechanical test bars; and finally, necessary handling operations involved in the transfer of specimens in and out of test fixtures can be a source of mechanically induced and environmentally enhanced flaws. Interpretation of flaw origins would require a controlled evaluation of each step in the processing and testing of specimens and would involve statistical quantities of material. The research nature of the program currently supplying specimens to the University of Dayton for evaluation precluded a definitive characterization of the origin and nature of strength limiting flaws in the alkali halides.

The absence of a measurable yield point in a particular specimen or its failure to exhibit a high strength may reflect the presence of extrinsic flaws and not necessarily describe its intrinsic strength. Therefore, in reviewing and comparing the strength data, greater significance should be assigned to the strongest specimens of a compositional grouping since these are likely to be most representative of achievable strength levels.

The same qualifications should also apply to the test specimens supplied by other vendors (Harshaw, ManLabs, Hughes, and Optovac).

3.2.1.1 Potassium Chloride

Mechanical property data, including yield and ultimate strength in four-point bending, were obtained for a total of 91 specimens, nominally 4 x 4 x 50 mm, representing 45 different combinations of composition and fabrication procedures. Supplementing these data were measurements of Knoop hardness and a microstructural evaluation.

Measurements of thermal diffusivity, thermal conductivity, specific heat, and thermal expansion were performed on a select group of press forged specimens, including unalloyed KCl and three alloys. A limited amount of x-ray diffraction measurements were also performed to develop lattice parameter-composition correlations for several alloys.

Mechanical Properties of Honeywell KCl and KCl Alloys

Mechanical property data for unalloyed KCl and six different alloys are summarized in Table 16. These data are arranged in their order of forging number for each composition.

A total of 30 specimens of press forged unalloyed KCl from 14 different forgings were evaluated. In general, it was noted that the strength of these specimens varied directly with hardness and inversely with mean grain size.

A few of these specimens experienced secondary grain growth at some point in their fabrication and exhibited yield strengths typically in the range of 0.5 to 0.75 ksi with corresponding Knoop hardness values of 10 to 13 kg/mm².

The majority of the specimens, however, had a fine grained, elongated microstructure typical of that shown in Figure 38. Mean grain sizes of these specimens were generally 8 to 13 μm with a few having mean values as large as 20 μm . Corresponding hardness values were typically in the range of 15 to 22 kg/mm². The average yield strength of the 8 to 13 μm grain size specimens was 2.58 ksi with an average ultimate strength of 3.57 ksi.

Specimens from six of the unalloyed KCl forgings exhibited microstructures indicative of extensive discontinuous grain growth and yet their strength and hardness values were more representative of fine grained polycrystalline material. Honeywell's microstructural data for these particular forgings specified mean grain sizes of 4 to 9 μm , but when polished sections were prepared by UDRI, microstructures typical of Figure 39 were obtained. The photomicrograph of Sample KCO75-5B-1M is of particular significance

TABLE 16. TEST RESULTS FOR HONEYWELL PRESS FORGED KCl

Specimen No.	Strength (ksi)		Knoop Hardness (kg/mm ²)		Mean Grain Size (μm)
	Yield	Ultimate	50 gm	100 gm	
<u>Unalloyed Potassium Chloride</u>					
KCO22-3B-1-1M	2.48	3.33	17.8	15.5	9.2
-2M	2.45	3.54	17.0	14.4	8.6
-11M	2.49	3.85	12.9	15.5	19.6
-12M	2.99	3.92	15.2	16.8	12.5
KCO13-2B-1-1M	3.03	4.80	17.3	22.4	12.3
-2M	3.04	3.83	18.1	21.2	17.5
KCH31-1B-2-3M	1.94	3.20	14.7	12.0	12.1
-4M	2.18	3.19	10.3	12.5	13.1
KCO60-4B-1-1M	none	2.92	17.9	22.4	7.2
-2M	3.12	4.35	19.2	22.3	8.6
KCO61-4B-1-1M	2.46	3.14	15.4	16.2	8.1
-2M	2.61	3.65	17.8	18.3	9.9
-3M	1.70	2.20	18.1	15.3	9.1
KCI23-1C-2-7M	2.21	3.18	16.2	17.6	12.1
-8M	2.34	2.93	16.2	16.0	10.0
KCH77-1B-2-1M	4.05	6.71	19.7	21.9	*
-2M	none	1.81	11.1	10.2	*
KCO69-5B-1M	2.99	3.64	16.9	18.2	10.4
-2M	0.75	1.42	12.6	10.8	*
KCO73-5B-1M	2.40	5.91	16.4	17.6	*
KCO74-5B-1M	2.49	4.26	14.7	16.4	20.1
-2M	2.42	3.37	14.1	17.6	12.6
KCO76-5B-1M	3.67	4.67	16.7	18.6	*
-2M	3.56	5.86	16.8	16.0	*
KCO71-5B-1M	none	3.66	22.9	20.9	*
-2M	3.86	5.07	17.2	20.1	10.0
KCO75-5B-1M	4.69	6.55	17.8	21.3	*
-2M	3.95	7.24	22.8	26.2	*
KCH87-4B-1-1M	0.51	1.24	13.8	9.1	*
-2M	0.74	1.59	10.4	9.5	657

* Discontinuous grain growth.

TABLE 16. TEST RESULTS FOR HONEYWELL PRESS FORGED KCl
(continued)

Specimen No.	Strength (ksi)		Knoop Hardness (kg/mm ²)		Mean Grain Size (μm)
	Yield	Ultimate	50 gm	100 gm	
<u>Potassium Chloride + 5 m/o Potassium Bromide</u>					
KC5KBH-1B-1M	none	1.26	15.6	18.8	Single XTL
-2M	1.38	1.83	18.1	22.6	Single XTL
KC5KB-OC-2-2M	none	3.27	19.6	22.8	15.2
-3M	3.95	5.07	22.8	26.3	9.1
KC5KB-OC-3-3m	3.54	5.04	20.1	23.0	6.8
-4M	4.04	5.20	21.4	25.6	5.8
KC5KB-OC-2-1M	4.15	5.15	20.3	22.5	---
-2M	4.43	5.64	21.2	23.1	9.8
KC5KB-OC-4-3M	3.97	5.85	18.1	19.1	8.0
-4M	4.37	6.55	18.5	19.1	12.1
KC5KBO31-4C-35					
-1M	5.48	6.97	18.3	18.8	9.8
-2M	5.15	6.21	17.9	18.6	11.6
KC5KBH45-1-1M	5.52	6.82	16.5	17.9	6.7
-2M	5.41	7.85	17.8	17.8	---
KC5KBH47-1-1M	3.20	5.21	14.7	13.7	8.2
-3M	5.69	6.88	14.0	14.7	10.5
KC5KBH48-4-2M	4.51	6.28	14.8	13.6	---
-3M	4.41	7.05	16.7	16.1	11.6
KC5KBH49-1-3M	5.07	7.13	17.7	17.3	8.2
-5M	5.47	7.29	17.6	16.9	7.0
KC5KBH56-2-5M	4.55	7.28	14.9	15.6	8.2
-6M	5.16	7.68	13.9	13.9	---
KC5KBH57-1-5M	3.06	5.77	16.6	15.2	8.4
-6M	3.61	5.11	16.8	16.2	8.2

TABLE 16. TEST RESULTS FOR HONEYWELL PRESS FORGED KCI
(continued)

Specimen No.	Strength (ksi)		Knoop Hardness (kg/mm ²)		Mean Grain Size (μm)
	Yield	Ultimate	50 gm	100 gm	
<u>Potassium Chloride + 5 m/o Rubidium Chloride</u>					
KC5RCO1B-9M	1.13	1.64	16.0	16.8	Single XTL
-10M	1.11	1.47	18.0	18.2	Single XTL
KC5RCO(83)-5M	2.70	4.82	21.3	22.4	9.4
-6M	3.54	4.94	19.9	22.5	8.3
KC5RC-OC-2-1M	5.03	6.48	21.8	26.3	6.0
-2M	4.55	6.48	22.8	20.7	8.5
KC5RCH30-1B-35					
-1M	5.77	7.75	17.4	18.6	---
-2M	5.77	7.71	16.3	18.8	6.9
KC5RCH-38-1-3M	5.13	6.08	17.8	17.5	7.5
-4M	5.69	6.90	17.3	16.5	---
KC5RCH-37-1-3M	5.60	7.26	17.7	17.9	7.4
-4M	5.45	6.37	15.0	15.8	---
KC5RCH40-15-7M	4.15	5.66	17.8	18.6	12.1
-8M	3.53	5.43	18.1	18.6	---
KC5RCH-35-1M	2.76	5.53	17.8	18.9	5.9
-2M	4.45	5.93	17.9	18.6	---
KC5RCH38-2-3M	5.50	8.92	17.3	16.9	12.0
-5M	none	4.21	16.2	15.9	12.4
KC5RCH52-1-1M	4.33	6.67	17.1	16.1	9.1
-2M	4.77	6.53	15.9	16.1	8.4
KC5RCH42-4-1M	4.94	6.30	15.7	16.6	---
-3M	5.05	5.90	15.6	16.2	8.4
KC5RCH60-1-5M	4.53	6.12	17.0	17.2	9.1
-6M	2.89	6.01	18.4	18.9	9.6

TABLE 16. TEST RESULTS FOR HONEYWELL PRESS FORGED KCl
(concluded)

Specimen No.	Strength (ksi)		Knoop Hardness (kg/mm ²)		Mean Grain Size (μm)
	Yield	Ultimate	50 gm	100 gm	
<u>Potassium Chloride + 10 m/o Rubidium Chloride</u>					
KC10-RCO-1B-7M	2.01	2.55	22.0	21.0	Single XTL
-8M	2.18	2.88	19.9	23.0	Single XTL
KC10RCO(86)-2M	5.93	7.22	21.3	25.3	8.2
KC10RC-OC-1-2M	none	4.99	26.8	29.1	4.5
-3M	3.68	6.35	28.2	26.3	---
KC10RCH39-4-5M	5.01	6.07	17.8	18.7	7.0
-6M	5.39	6.29	17.8	17.8	---
<u>Potassium Chloride + 500 ppm Eu⁺²</u>					
KC05EuH27-1B-3					
-4M	6.11	9.80	18.2	18.8	---
-5M	5.99	10.30	17.8	15.4	4.4
<u>Potassium Chloride + 1 m/o Cesium Chloride</u>					
KC1CCH26-1B-2					
-2M	3.96	4.41	16.4	18.8	15.7
-3M	4.34	5.42	17.8	15.8	11.3
<u>Potassium Chloride + 500 ppm Strontium Chloride</u>					
KC05SCH-1B-1M	2.32	3.09	14.9	14.3	Bicrystal
-2M	2.35	3.32	17.8	18.2	Bicrystal

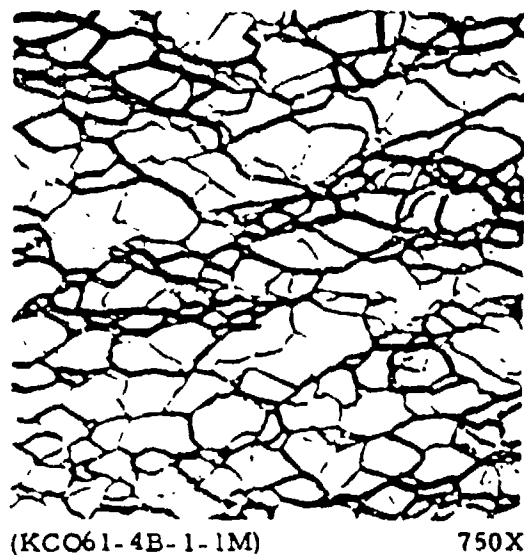
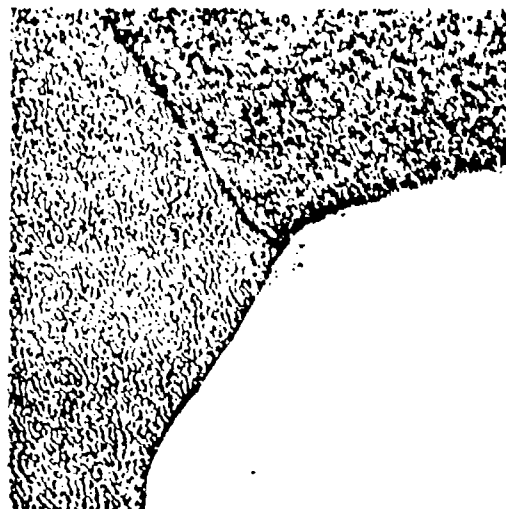


Figure 38. Honeywell Hot Forged Unalloyed KCl.

since this specimen, with a yield strength of 4.69 ksi, was the strongest of the unalloyed KCl from Honeywell even though a yield strength well below 1.0 ksi would have been anticipated with grains this large. Honeywell's data for this forging indicated a mean grain size of $4.0\text{ }\mu\text{m}$ which would be consistent with its strength. Thus, it would appear that discontinuous grain growth was induced in this specimen (and probably in the other strong specimens as well) after the flexural tests by the cutting and grinding operations associated with the preparation of optical microscopy samples.

The initiation of discontinuous grain growth at near room temperature by the relatively moderate strain energy input from polishing would indicate that the press forged microstructure of the unalloyed KCl was not very stable.



6A)

(KCO75-5B-1M)

250X



6B)

(KCO74-5B-2M)

250X

Figure 39. Discontinuous Grain Growth in Honeywell Hot Forging Unalloyed KCl.

Two specimens of single crystal KCl + 5 m/o KBr and 12 specimens from six forgings of the same alloy were evaluated. One of the two single crystal specimens failed without yielding at 1.26 ksi, whereas, the second specimens had a yield strength of 1.38 ksi (approximately three times that of unalloyed KCl) and an ultimate strength of 1.83 ksi.

The press forged specimens had a uniform elongated microstructure typical of that shown in Figure 40. Mean grain sizes ranged from 7 to 15 μm with hardness values of 14 to 26 kg/mm^2 ; not much higher than the hardness range of the single crystal material (16 to 23 kg/mm^2).

With the exception of one specimen which failed without yielding at 3.27 ksi, the strengths of the press forged KCl + 5 m/o KBr alloys were relatively high. Yield strength averaged 4.50 ksi and an average ultimate strength of 6.15 ksi was obtained. The first few forgings of this group were weaker than the others. Otherwise, no direct correlation between strength and forging sequence was apparent.



Figure 40. Honeywell Hot Forged KCl + 5 m/o KBr.

Two specimens of single crystal KCl + 5 m/o RbCl and 14 specimens from 7 forgings of the same alloy were evaluated. The two single crystal specimens exhibited similar characteristics with an average yield strength of 1.12 ksi and an average ultimate strength of 1.56 ksi. Single crystal hardness values ranged from 16 to 18 kg/mm².

The strength of the press forged KCl - 5 m/o RbCl alloy was nearly the same as the KCl - 5 m/o KBr alloy. The average yield strength was 4.56 ksi; the average ultimate strength was 6.27 ksi. One forging, KC5RCH30-1B-35, was significantly stronger than the others with two specimens exhibiting yield strengths of 5.8 ksi and ultimate strengths of 7.7 ksi. The hardness of the press forgings ranged from 15 to 26 kg/mm² which was not appreciably different from that of the m/o KBr alloy.

Most of the KCl - 5 m/o RbCl specimens exhibited a normal microstructure similar to that shown in Figure 41. One specimen, KC5RC-OC-2-2M, however, contained regions of apparent discontinuous grain growth (Figure 42A) and duplex microstructure (Figure 42B). The strength and hardness of this sample did not indicate the presence of oversized grains and, therefore, it is suspected that this grain growth occurred after flexural testing, probably during the preparation of the optical microscopy specimen. The duplex microstructure, while unusual, had no detrimental effect upon the strength of this sample.

A pair of single crystal specimens of KCl - 10 m/o RbCl and 5 specimens from three press forgings of the same alloy were evaluated. The single crystal specimens had average yield and ultimate strength of 2.09 and 2.71 ksi, respectively. These values are approximately four times larger than unalloyed single crystal KCl. The hardness of the alloy (22 kg/mm²) was twice that of unalloyed KCl.

One of the press forged samples (KC10RC-OC-1-2M) failed at 4.99 ksi without exhibiting a yield point. The three specimens from the other two



Figure 41. Hot Forged KCl + 5 m/o RbCl.



42A) Discontinuous Grain Growth
250X



42B) Duplex Microstructure
(KC5RC-OC-2-2M) 250X

Figure 42. Honeywell Hot Forged KCl + 5 m/o RbCl.

forgings had yield strengths of 5.01 to 5.93 ksi and ultimate strengths of 6.07 to 7.22 ksi. There was not a good correlation between hardness and strength with this alloy. The weakest of the press forgings (KC10RC-OC-1) was, in fact, the hardest. Similarly, the smallest mean grain size ($4.5\text{ }\mu\text{m}$) was measured for this weakest forging. It is suspected that the strength of this forging was affected by microstructural factors. While most of the material had a typical forged microstructure (Figure 43A), at least one region contained a massive faceted single crystal (Figure 43B). If single crystals such as this were prevalent throughout the forged material, weakening would be expected.

A pair of specimens from a single forging of KCl doped with 500 ppm of Eu^{+2} were the strongest KCl alloys evaluated. Yield strengths of 6.11 and 5.99 ksi and ultimate strengths of 9.80 and 10.30 ksi were obtained with this alloy. These were not especially hard alloys (15.4 to 18.8 kg/mm^2). Optical microscopy (Figure 44) revealed a fine grained, very elongated microstructure with a mean grain size of $4.4\text{ }\mu\text{m}$.

The addition of 1 m/o CsCl appeared to have a moderate strengthening effect. Two press forged samples of this alloy had higher strengths than unalloyed KCl of similar grain size but hardness values were equivalent. As is evident in Figure 45, the microstructures of the KCl - 1 m/o CsCl alloy was atypically equiaxed.

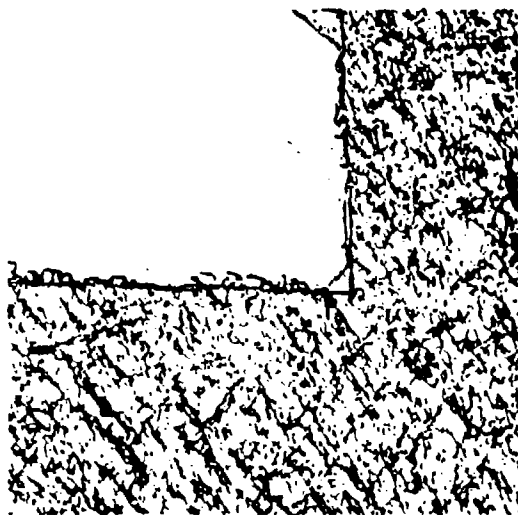
A pair of KCl:500 ppm Sr^{+2} bicrystals were the strongest of the unforged alloys evaluated. The two specimens had yield strengths of 2.32 and 2.35 ksi with corresponding ultimate strengths of 3.09 and 3.32 ksi. These strengths, 4 to 6 times that of unalloyed KCl, were due entirely to the SrCl_2 addition. It is doubtful if the presence of the single transverse grain boundary in each of the test bars had any effect upon their strength.



43A)

Typical Region

250X



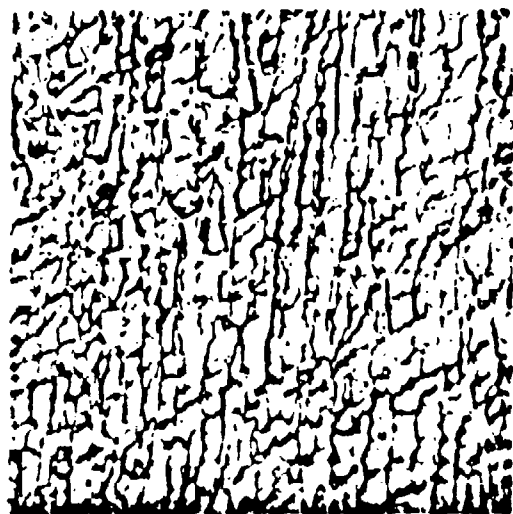
43B)

Discontinuous Grain Growth

250X

(KC10RC-OC-1-2M)

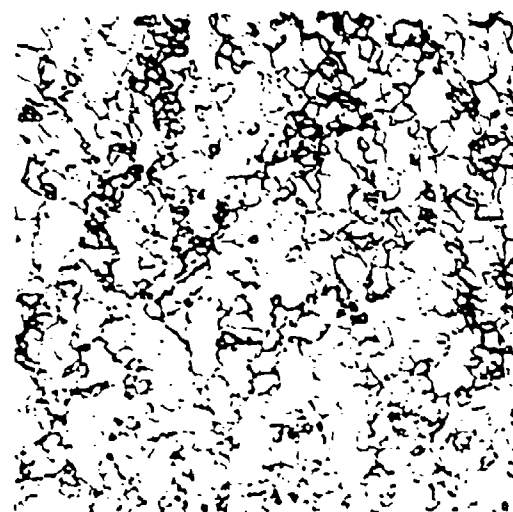
Figure 43. Honeywell Hot Forged KCl + 10 m/o RbCl.



(KC05EuH27-1B-3-5M)

750X

Figure 44. Honeywell Hot Forged KCl:500 ppm Eu^{+2} .



(KC1CCH26-1B-2-3M)

250X

Figure 45. Honeywell Hot Forged KCl + 1 m/o CsCl.

X-Ray Diffraction Studies

Debye-Scherrer x-ray patterns were obtained for single crystal alloys of KCl + 5 m/o KBr, KCl:500 ppm Sr^{+2} , KCl + 5 m/o RbCl, KCl + 10 m/o RbCl, KCl + 20 m/o RbCl, KCl + 40 m/o RbCl, and unalloyed RbCl. The diffraction lines of only KCl were obtained with all of the alloys. Precision lattice constants were calculated from the diffraction patterns. These data are summarized in Table 17 and Figure 46.

The lattice constants of both the KCl - KBr and KCl - RbCl were larger than that of unalloyed KCl. Moreover, the lattice expansion of the KCl - RbCl alloys increased linearly in proportion to the amount of RbCl formation. Since the ionic radii of both Rb and Br are both slightly larger than K and Cl, respectively, lattice expansion would be expected if the alloys formed substitutional solid solutions.

The KCl:500 ppm Sr^{+2} alloy experienced a slight lattice contraction which probably represented the combined effect of substitution of a smaller cation and relaxation of the cation sublattice around charge-compensating cation vacancies.

Thermal Properties of Honeywell KCl and KCl Alloys

A group of polycrystalline press forged KCl and KCl alloys were evaluated by the flash technique to determine their thermal diffusivity, specific heat and thermal conductivity. Included in this group were press forged specimens from both Optovac and Harshaw starting material; a 500 ppm Eu^{+2} KCl alloy; and two other alloys (KCl + 5 m/o KBr and KCl + 5 m/o RbCl). These data are summarized in Figure 47 and include similar results for large grained Polytran material from Harshaw.

The baseline measurements of specific heat for these materials exhibited relatively large scatter which was independent of specimen composition. This scatter is believed to result from the combined effects of the small sized samples used in the drop-calorimeter measurement and an

TABLE 17. SUMMARY OF X-RAY DIFFRACTION STUDIES
OF HONEYWELL KCl ALLOYS

Alloy	Lattice Constant (\AA)
KCl - 5% KBr	6.310 ± 0.002
KCl + 500 ppm Sr^{+2}	6.291 ± 0.001
Unalloyed KCl	6.293 ± 0.001
KCl + 5 m/o RbCl	6.304 ± 0.001
KCl + 10 m/o RbCl	6.321 ± 0.001
KCl + 20 m/o RbCl	6.364 ± 0.001
KCl + 30 m/o RbCl	6.390 ± 0.003
KCl + 40 m/o RbCl	6.423 ± 0.003
RbCl	6.594 ± 0.002

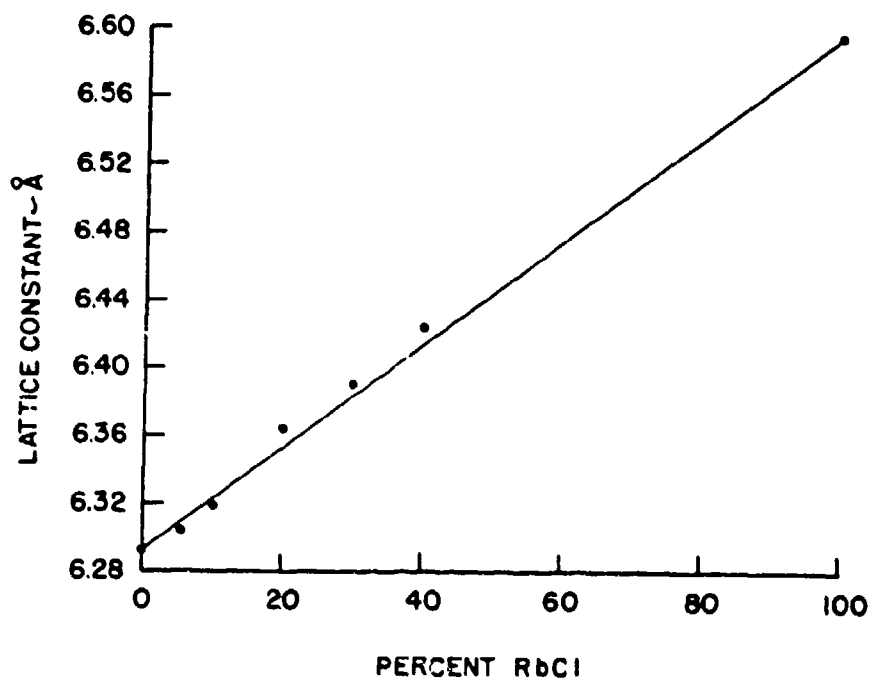


Figure 46. Lattice Constants for Various KCl-RbCl Alloys.

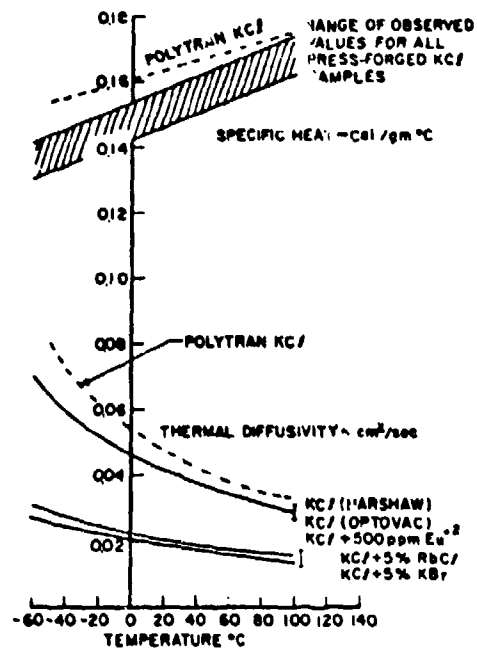
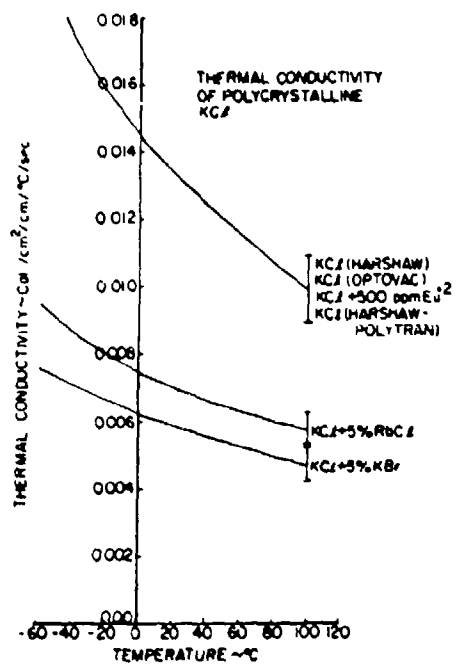


Figure 47. Thermal Properties of Honeywell Press Forged KCl Alloys and "Polytran" KCl.

insufficient number of repeat measurements to establish a good statistical basis for the measurement. As a consequence, these data are presented as a range of observed values for all of the press forged samples. In contrast, the specific heat values for Polytran KCl were larger than those obtained for the press forged material and were quite close to published values for KCl.

Thermal diffusivity data were quite reproducible with the two unalloyed KCl samples and the 500 ppm Eu^{+2} KCl alloy forming one tight group and the KCl - KBr and KCl - RbCl alloys another. The thermal diffusivity of the Polytran KCl was somewhat higher than that of the fine grained materials; a difference which may be the result of phonon scattering by grain boundaries in the press forged material.

When the measurements of specific heat and thermal diffusivity were reduced to thermal conductivity values, all of the unalloyed KCl samples and the 500 ppm Eu^{+2} alloy formed a common group, whereas, the two 5 m/o alloys had much lower values. The lowering of thermal conductivity by more than a factor of two with an alloying addition of only five mole-percent was not anticipated. Repeat measurements with freshly prepared samples have confirmed these results.

Thermal expansion measurements were obtained from room temperature to 100°C for three KCl alloys containing 5 m/o KBr, 5 m/o RbCl, and 10 m/o RbCl. These data are compared in Table 18 with similar results obtained earlier for unalloyed KCl.

The data for each alloy were obtained in four separate runs and while individual values varied, the average coefficient of thermal expansion for each alloy was identical; $34.7 \times 10^{-6} \text{ cm/cm}^{\circ}\text{C}$. This is only 4% lower than the reference value for unalloyed KCl of $36 \times 10^{-6} \text{ cm/cm}^{\circ}\text{C}$. It would, therefore, appear that the alloying additions had no significant effect upon the thermal expansion behavior of the KCl.

TABLE 18. COEFFICIENT OF THERMAL EXPANSION
OF HONEYWELL KCl AND KCl ALLOYS

Sample No.	Composition	Coefficient of Thermal Expansion- (20-100°C) (cm/cm°C x 10 ⁻⁶)
IAH-7	KCl	36.8
KC5KBH-1B-2M	KCl + 5 m/o KBr	34.8
		33.0
		35.2
		35.7
		(Avg. 34.7)
KC5RCO(83)-6M	KCl + 5 m/o RbCl	35.3
		34.2
		34.9
		34.2
		(Avg. 34.7)
KC10RC-OC-1-2M	KCl + 10 m/o RbCl	34.8
		33.7
		35.9
		34.5
		(Avg. 34.7)

Homogeneity of Single Crystal KCl Alloy Ingots

Single crystal ingots of KCl - 10 m/o RbCl and KCl - 10 m/o KBr, nominally 6.4 to 7.6 cm in diameter and 9.0 to 11.5 cm in length, were evaluated for compositional homogeneity. Analytical procedures involved in this evaluation included x-ray diffraction measurements of precision lattice constants and measurements of heat capacity and thermal diffusivity.

Test samples were obtained by sawing a rectangular parallelepiped lengthwise from each ingot according to the schematic diagram of Figure 48. The 8.25 cm diameter KCl - 10 m/o RbCl ingot was cut at radial distances of 2.64 and 3.64 cm and trimmed to obtain a slice 1.0 cm thick, 1.27 cm wide, and 11.43 cm long. Similar cuts were taken on the KCl-KBr ingot at

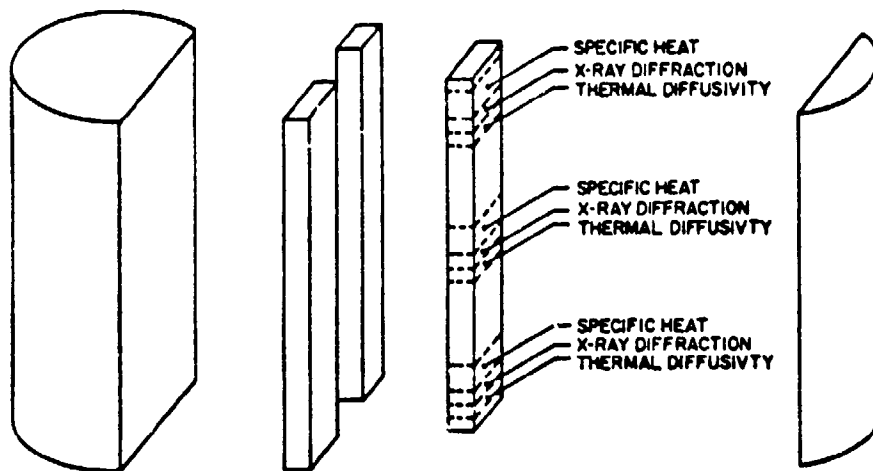


Figure 48. Cutting Diagram for KCl Alloy Homogeneity Analysis.

radial distances of 1.87 and 2.79 cm to obtain a slice 0.91 cm thick, 1.27 cm wide and 8.89 cm long. Approximately 0.65 cm of material were sliced from either end and discarded so that the samples consisted entirely of material from the bulk of the ingots. Sections 1.20 cm long were then sliced from either end and the center of the ingot samples. These sections were further reduced to 3 slices; a 0.63 cm thick heat capacity specimen, 0.25 cm thick x-ray specimen, and a 0.32 cm thick thermal diffusivity specimen.

X-ray powder diffraction samples were scraped from the sides of the x-ray specimens corresponding to the two radial locations of the original ingot. A total of six specimens, two at each of the 3 axial locations, were analyzed for each ingot. The results of these measurements are given in Table 19.

TABLE 19. SUMMARY OF X-RAY DIFFRACTION STUDIES
OF SINGLE CRYSTAL KCl ALLOY INGOTS

<u>Lattice Constants of KCl - 10 m/o RbCl (\AA)</u>		
<u>Axial Distance (cm)</u> *	<u>Radial Distance (cm)</u>	
	<u>2.64</u>	<u>3.64</u>
1.40	6.3219 ± 0.0008	6.3301 ± 0.0008
5.84	6.3245 ± 0.0006	6.3241 ± 0.0010
10.35	6.3250 ± 0.0010	6.3290 ± 0.0007

<u>Lattice Constants of KCl - 10 m/o KBr (\AA)</u>		
<u>Axial Distance (cm)</u> **	<u>Radial Distance (cm)</u>	
	<u>1.87</u>	<u>2.79</u>
1.40	6.3328 ± 0.0008	6.3370 ± 0.0013
4.57	6.3347 ± 0.0009	6.3344 ± 0.0009
7.81	6.3362 ± 0.0008	6.3344 ± 0.0010

<u>Lattice Constants of Pure Alkali Halides (\AA)</u>	
KCl	6.2936 ± 0.0012
KBr	6.5998 ± 0.0002
RbCl	6.5939 ± 0.0002

* In a direction opposite to the ingot growth direction.

** Crystal growth direction unknown.

If it can be assumed that both alloys obey Vegard's law and exhibit a linear variation of lattice constant with alloy content (see Figure 46), the effective composition of the two ingots can be computed from empirically derived relationships between alloy content and lattice parameter values with the following equations:

$$X_{\text{RbCl}} = \frac{a_o - 6.2936}{0.3003} \quad (26)$$

$$X_{\text{KBr}} = \frac{a_o - 6.2936}{0.3062} \quad (27)$$

Table 19 was converted from lattice constant values to equivalent alloy contents to yield the data of Table 20.

TABLE 20. COMPUTED ALLOY CONTENTS OF SINGLE CRYSTAL KCl ALLOY INGOTS

<u>RbCl Content of the KCl - RbCl Ingot (%)</u>		
<u>Axial Distance (cm)</u>	<u>Radial Distance (cm)</u>	
	<u>2.64</u>	<u>3.64</u>
1.40	8.8 - 10.1	11.5 - 12.8
5.84	9.7 - 10.9	9.4 - 10.9
10.35	9.7 - 11.2	11.2 - 12.4
<u>KBr Content of the KCl - KBr Ingot (%)</u>		
<u>Axial Distance (cm)</u>	<u>Radial Distance (cm)</u>	
	<u>1.87</u>	<u>2.79</u>
1.4	12.1 - 13.4	13.4 - 15.0
4.57	12.7 - 14.1	13.2 - 14.0
7.81	13.3 - 14.6	13.2 - 14.0

The range of percentages given in Table 20 represent estimates of the precision of the calculations resulting from specified accuracies of the lattice constant measurements. While this determination of ingot composition is probably oversimplified, it provides a fairly reasonable representation of compositional fluctuations in the ingots. In this respect, there appeared to be point-to-point variations in both alloys but no systematic changes in either the radial or axial directions. The calculated composition of the KCl-KBr ingot was close to the nominal value of 10% RbCl, whereas, the KCl-KBr ingot appeared to have a KBr content slightly higher than 13%.

Thermal diffusivity and heat capacity measurements required slab-shaped samples and there was no opportunity to evaluate changes in these properties with respect to radial position in the parent ingot. Axial position variations were, of course, evaluated; these data are summarized in Table 21. Within the precision of the two measurements, there was no apparent axial location dependence of heat capacity or thermal diffusivity in either ingot.

The measured values of thermal diffusivity and heat capacity, and the derived values of thermal conductivity for the 10 m/o alloys confirmed previous observations that both alloying additions have little effect upon the heat capacity but will produce a significant reduction of both thermal conductivity and thermal diffusivity. As is evident in Figure 49, the addition of up to 10 m/o of either KBr or RbCl produces a monotonic decrease of thermal conductivity. This behavior is quite consistent with the experimental observation of Eucken and Kuhn⁽¹⁵⁾ in their studies of KCl-KBr alloys.

(15) A. Eucken and G. Kuhn, "Ergebnissen neuer Messungen der Wärmeleitfähigkeit fester krystallisier Stoffe bei 0° und -190°C," Z. Physical Chem., 134, Feb. 26, 1928.

FIGURE 21. THERMAL PROPERTY VARIATIONS IN THE SINGLE CRYSTAL KCl ALLOY INGOTS AT 250°C

Average Axial Position (cm)	Heat Capacity (cal/gm°C)	Thermal Diffusivity (cm ² /sec)
<u>KCl - 10 m/o RbCl</u>		
1.56	0.156	0.0141
6.00	0.153	0.0133
10.51	0.156	0.0137
Average	0.155 ± 0.008	0.0137 ± 0.0009
<u>KCl + 10 m/o KBr</u>		
1.56	0.147	0.0134
4.73	0.140	0.0138
7.97	0.141	0.0138
Average	0.143 ± 0.007	0.0137 ± 0.0009

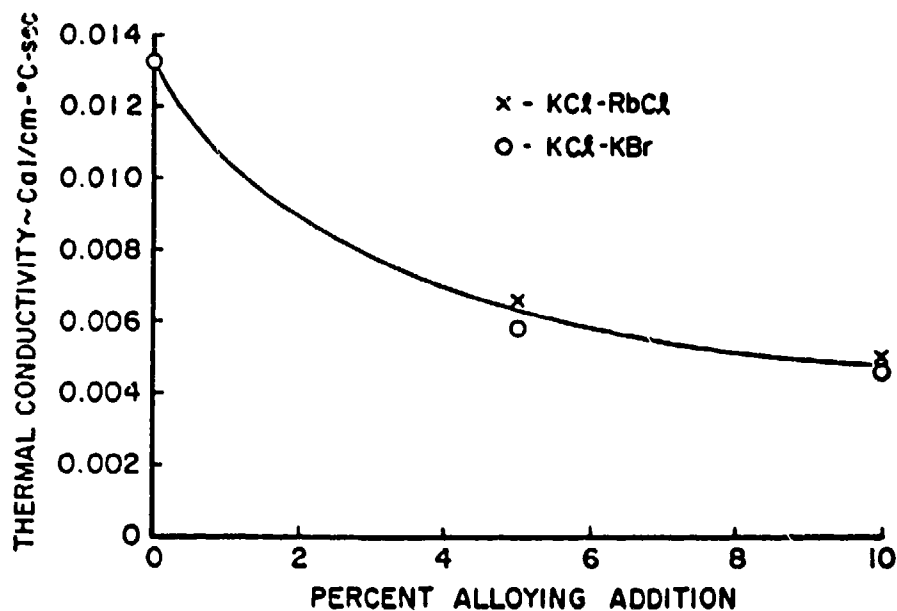


Figure 49. Thermal Conductivity of KCl Alloys.

3.2.1.2 Honeywell Press Forged NaCl

A total of 19 press forged NaCl specimens nominally 4 x 4 x 50 mm representing 8 forgings of pure NaCl and one press forged NaCl - 10 m/o NaBr alloy were evaluated. The results of this evaluation are summarized in Table 22. All of the unalloyed NaCl forgings produced a fairly uniform, slightly elongated microstructure typical of that shown in Figure 50. Mean grain diameters ranged from 8 to 14 μm and there was preferred orientation evident in all of the specimens. The NaCl-NaBr alloy had a coarser microstructure (Figure 51) and also displayed elongated oriented grains.

The samples forged from Bridgeman-grown single crystals (denoted by the letter B in the specimen number) had yield strengths ranging from 2.52 to 4.15 ksi and ultimate strengths of 3.89 to 5.99 ksi. Similar strengths were obtained with two of the three forgings of Kyropoulos-grown material (denoted by the letter K in the specimen number). The third pair of Kyropoulos-grown specimens (NCH-26-1K) were significantly stronger than the others with average yield and ultimate strength of 6.61 and 9.87 ksi, respectively. It was suspected that these specimens were actually mis-labeled NaCl alloys. However, a quantitative compositional analysis with a scanning electron microscope/energy dispersive analyzer failed to detect significant levels of either possible alloying additions, Br or K. Honeywell⁽¹⁶⁾ has observed that the Kyropoulos growth process is not as clean as the Bridgeman process. It is possible that forging NCH-26-1K was inadvertently impurity strengthened by contamination during the growth of the starting material.

The relatively large-grained NaCl - 10 m/o NaBr forged specimens were stronger than most of the finer grained unalloyed NaCl specimens. The alloying addition of NaBr did produce a measurable strengthening of the NaCl.

(16) W.B. Harrison, et al., "Halide Material Processing for High Power Infrared Laser Windows," Interim Technical Report 2, Contract F33615-72-C-2019, Honeywell, Inc., February 1973.

TABLE 22. TEST RESULTS FOR HONEYWELL PRESS FORGED NaCl

Specimen No.	Strength (ksi)		Knoop Hardness (kg/mm ²)		Mean Grain Size (μm)
	Yield	Ultimate	50 gm	100 gm	
<u>Sodium Chloride</u>					
NCO3-1B-1-1M	3.20	4.47	37.7	30.0	9.8
-2M	2.52	3.99	29.7	29.3	9.2
NCH17-1B-1-3M	3.73	5.99	27.4	29.5	10.1
-4M	3.92	5.78	31.2	27.8	10.6
NCO11-2B-3-3M	3.63	5.15	34.8	28.7	8.3
-4M	4.15	6.14	38.6	29.8	7.9
NCH17-1B-3-1M	3.18	5.66	33.3	32.9	10.3
-2M	3.29	5.13	36.0	28.5	13.6
NCO47-3B-3-1M	3.63	5.52	44.4	34.5	8.9
-2M	3.83	5.53	30.3	31.6	8.5
-3M	3.22	5.27	39.9	35.0	6.4
NCH24-1K-1M	2.86	6.62	22.0	22.0	8.0
-2M	3.91	6.87	25.0	22.0	7.8
NCH25-1K-1M	3.83	6.30	25.0	23.0	6.8
-6M	3.41	6.91	24.0	23.0	6.5
NCH26-1K-2M	6.62	9.56	23.2	28.0	10.5
-8M	6.60	10.18	37.9	30.5	7.3
<u>Sodium Chloride + 10% Sodium Bromide</u>					
NC10NBO33K-1					
-3M	5.07	6.01	44.4	35.8	48
-4M	4.23	5.51	31.6	35.6	37

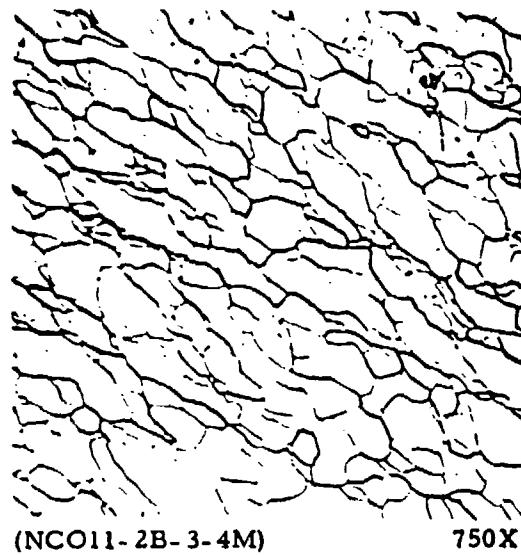


Figure 50. Honeywell Hot Forged Unalloyed NaCl.



Figure 51. Honeywell Hot Forged NaCl + 10 m/o NaBr.

3.2.1.3 Honeywell Press Forged KBr

Eleven press forged KBr specimens nominally 4 x 4 x 50 mm from five different forgings were evaluated. The test results are summarized in Table 23.

One pair of samples from forging KBH35-1B-1 had apparently experienced severe discontinuous grain growth during fabrication. The mean grain size of these samples exceeded 2000 μm . No yield point was observed in either specimen and their ultimate strengths were equivalent to that of single crystal materials. These samples were also quite soft with Knoop values of 7.5 to 9.7 kg/mm^2 . All of the other KBr samples had fine grained somewhat elongated, polycrystalline microstructures typical of that shown in Figure 52.

The strongest forging was KB05-1-B with an average yield strength of 3.15 ksi and average ultimate strength of 4.38 ksi. This was also the hardest of the KBr forgings; the Knoop values being nearly twice those of single crystal material. This forging had a mean grain size of 8.5 μm , which was smaller than that of the other forgings but not enough to account for the higher strength.

The other three forgings had yield strengths of 1.60 to 2.43 ksi and ultimate strengths of 2.5 to 4.49 ksi. The hardness of these forgings ranged from 8.1 to 12.4 kg/mm^2 and mean grain sizes ranged from 9.3 to 12.4 μm .

The only difference noted among the polycrystalline forgings was hardness, which in this group of samples appeared to correlate with strength.

TABLE 23. TEST RESULTS FOR HONEYWELL PRESS FORGED KBr

Specimen No.	Strength (ksi)		Knoop Hardness (kg/mm ²)		Mean Grain Size (μm)
	Yield	Ultimate	50 gm	100 gm	
KBH35-1B-1-1M	none	0.70	8.5	7.5	~ 2000
-2M	none	0.93	9.7	7.7	~ 2000
KB05-1B-1M	3.09	4.18	15.2	13.4	7.4
-2M	3.21	4.58	14.3	14.0	9.5
KB015-2B-3-3M	2.09	2.89	8.1	10.9	11.2
-4M	2.43	3.00	12.2	12.4	12.4
KB066-3B-1-1M	1.91	4.12	11.4	11.5	9.3
-2M	1.70	4.49	11.4	11.4	11.7
-3M	1.60	2.50	13.1	11.9	12.2
KB078-4B-1M	1.90	3.26	9.3	8.9	9.7
-6M	1.93	2.68	9.3	9.9	9.5



(KB066-3B-1-2M)

750X

Figure 52. Honeywell Hot Forged KBr.

3.2.2 Harshaw Alkali Halides

A total of 117 test specimens from Harshaw, representing single and polycrystalline KCl with various divalent elemental additions, were evaluated. These evaluations were confined to measurements of flexural strength, Knoop hardness and microstructural characteristics and are summarized in Table 24. The IAH, IAF, and IAG samples were 10 x 13 x 75 mm bars; all other Harshaw specimens had the nominal dimensions of 6.0 x 6.0 x 50 mm.


A group of 17 single crystal specimens exhibited a surprising range of ultimate strengths (0.9 to 5.8 ksi). These were among the first materials evaluated in this program and a suitable extensometer for yield strength measurement was not available until most of the single crystal samples had been evaluated. Unfortunately, none of the four specimens for which a yield point was obtained were exceptionally strong.

An attempt was made to identify the cause of this wide range of strengths. Laue and Debye-Scherrer x-ray patterns were obtained for selected specimens. Knoop hardness measurements were performed on the tension surface of the specimens; electron microprobe analyses were performed on the strongest specimen of this set.

The Laue x-ray analysis revealed that the tension-compression faces of the single crystals were parallel to the (111) crystallographic plane. Hardness values ranged from 11 to 15 kg/mm² and were apparently unrelated to the strength of the sample. Lattice constants derived from the x-ray diffraction patterns fell within $\pm 0.01\text{\AA}$ of the reported value of 6.29 \AA for pure KCl. The electron microprobe analysis detected the presence of only the elements K and Cl. Subsequent emission spectrographic analyses by AFML of one of the stronger samples found no foreign cation in a concentration greater than 30 ppm.

Thus, the unusually high strengths exhibited by several of these specimens could not be explained on the basis of strengthening impurities or

TABLE 24. TEST RESULTS FOR HARSHAW SINGLE
AND POLYCRYSTALLINE KCl

Specimen No.	Strength (ksi)		Knoop Hardness (kg/mm ²)		Mean Grain Size (μm)
	Yield	Ultimate	50 gm	100 gm	
LAH -2	*	0.90	13	---	 Single XTL
-3	*	1.46	14	---	
-4	---	2.98	14	---	
-6	0.49	1.50	12	---	
-7	0.49	1.50	---	---	
-8	0.46	1.94	---	---	
-9	*	3.22	10	---	
-11	*	1.26	13	---	
-12	*	0.90	14	---	
-13	*	1.32	13	---	
-14	*	1.08	13	---	
-16	*	1.50	14	---	
-17	0.47	1.88	---	---	
-21	*	2.89	11	---	
-23	*	3.49	---	---	
-24	*	2.02	13	---	
-25	*	5.83	15	---	
LAF -6	0.57	0.79	---	---	---
-10	0.49	0.61	---	---	---
-11	0.42	0.65	14	---	800
-12	0.40	0.57	---	---	---
-19	0.55	0.84	---	---	---
-21	0.44	0.59	---	---	---
-22	0.45	0.78	---	---	---
-23	0.43	0.70	---	---	---
-24	0.45	0.73	---	---	---
-25	0.46	0.80	13	---	2000
-26	0.47	0.80	---	---	---
-27	0.40	0.67	---	---	---
-30	0.49	0.81	---	---	---
-28	0.40	0.54	---	---	---
-29	0.40	0.60	---	---	---
-31	0.45	0.73	---	---	---
-32	0.44	0.78	14	---	900
-33	0.40	0.64	---	---	---
-35	0.42	0.69	---	---	---
-36	0.44	0.70	---	---	---

* Not measured.

TABLE 24. TEST RESULTS FOR HARSHAW SINGLE
AND POLYCRYSTALLINE KCl (continued)

Specimen No.	Strength (ksi)		Knoop Hardness (kg/mm ²)		Mean Grain Size (μm)
	Yield	Ultimate	50 gm	100 gm	
IAG -2	0.43	0.64	---	---	---
-3	0.45	0.73	---	---	---
-4	0.43	0.77	14	---	1050
-5	0.43	0.78	---	---	---
-6	0.39	0.69	---	---	---
-7	0.45	0.69	---	---	---
-8	0.45	0.68	---	---	---
-11	0.40	0.77	---	---	---
-12	0.47	0.73	---	---	---
-13	0.45	0.55	---	---	---
-15	0.42	0.66	---	---	---
-16	0.48	0.89	12	---	1330
-17	0.49	0.82	---	---	---
-18	0.53	0.82	--	---	---
-19	0.52	0.83	---	---	---
-21	0.51	0.79	---	---	---
-22	0.54	0.98	11	---	1670
-23	0.56	0.82	---	---	---
-25	0.56	1.02	---	---	---
-26	0.54	0.99	---	---	---
<u>Potassium Chloride + 1000 ppm Ba⁺²</u>					
E25D56-1	1.60	1.90	14.1	13.5	28
-3	1.38	1.82	11.5	10.6	51
-5	1.25	2.29	14.0	11.6	42
-6	1.36	2.02	11.4	9.9	57
-8	1.34	2.26	13.6	11.6	50
-11	1.43	2.04	15.4	13.5	45
-13	1.13	2.12	14.1	12.2	53
-14	1.34	2.22	13.3	10.9	42
<u>Potassium Chloride + 500 ppm Ba⁺²</u>					
E42D56-1	1.25	2.32	15.5	16.1	26
-3	1.56	2.15	14.6	14.5	39
-5	1.75	3.47	14.1	15.2	35
-7	1.59	3.12	15.2	15.1	27
-9	1.70	2.89	13.7	14.6	---

TABLE 24. TEST RESULTS FOR HARSHAW SINGLE
AND POLYCRYSTALLINE KCl (continued)

Specimen No.	Strength (ksi)		Knoop Hardness (kg/mm ²)		Mean Grain Size (μm)
	Yield	Ultimate	50 gm	100 gm	
<u>Hot Forged Potassium Chloride + 500 ppm Ba⁺²</u>					
E42D56TCXF50-1	1.71	3.24	14.5	14.1	21
<u>Potassium Chloride + 500 ppm Eu⁺²</u>					
E28D63-9	1.83	2.88	15.4	13.5	44
-15	2.21	2.96	13.7	15.8	48
-20	1.99	2.79	13.5	13.5	63
-27	2.51	2.96	17.2	15.3	58
-28	1.95	2.74	19.8	15.3	48
E30D631-2	2.22	2.87	16.9	16.7	56
-3	1.76	2.72	18.4	19.0	34
-5	1.43	2.15	17.4	18.5	32
-7	2.09	2.49	15.4	15.9	49
-8	1.89	3.64	16.0	18.4	36
E43D63-1-3	1.91	2.35	17.8	18.8	51
-4	1.83	2.66	20.5	18.8	45
-8	1.65	2.38	19.4	18.8	112*
<u>Hot Forged Potassium Chloride + 500 ppm Eu⁺²</u>					
E30D631XF20B-1	2.43	2.96	15.3	18.1	43
-3	2.33	2.79	16.1	17.3	44
-4	2.45	3.67	15.6	15.8	30
-5	2.39	2.89	16.9	20.0	30
AFML638-3	3.18	5.11	16.6	15.8	---
-5	none	2.91	15.4	16.0	6.5
-7	none	2.99	14.7	16.2	---
-9	3.60	5.43	15.5	15.8	6.7
-12	3.71	4.96	15.4	15.8	7.4

* Discontinuous grain growth.

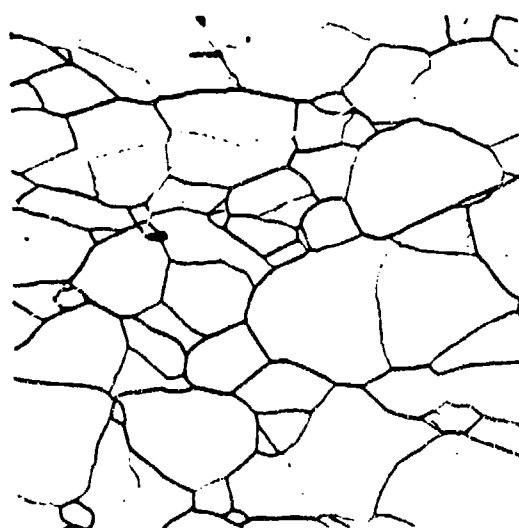
TABLE 24. TEST RESULTS FOR HARSHAW SINGLE
AND POLYCRYSTALLINE KCl (concluded)

Specimen No.	Strength (ksi)		Knoop Hardness (kg/mm ²)		Mean Grain Size (μm)
	Yield	Ultimate	50 gm	100 gm	
<u>Potassium Chloride + 200 ppm Sr⁺²</u>					
E19D-38-3	1.59	2.02	16.2	13.5	37
-5	1.74	2.42	15.7	15.8	41
-8	1.91	2.23	17.0	13.7	29
-9	1.63	2.15	15.5	12.9	34
-10	1.71	2.70	15.3	13.5	35
-12	1.50	1.78	14.0	13.1	52
-13	1.23	1.67	14.0	12.9	54
-17	1.55	2.38	17.8	15.8	33
-18	1.37	2.61	14.0	15.8	36
<u>Potassium Chloride + 500 ppm Sr⁺²</u>					
E40D381-1	1.86	2.38	15.4	13.4	52
-3	1.99	2.56	15.7	16.1	52
-5	1.80	2.42	17.1	17.0	51
-6	1.62	2.33	15.9	16.4	37
-8	1.75	2.37	15.6	16.7	53
<u>Hot Forged Potassium Chloride + 500 ppm Sr⁺²</u>					
E40D381AXF50-2	2.69	3.72	17.9	20.7	29
E40D381BXF20-1	1.95	2.90	16.1	18.1	32
-2	2.34	2.73	17.5	18.1	38
-5	2.47	2.85	16.0	17.5	28
-6	2.04	2.78	16.7	16.7	34
<u>Potassium Chloride + 400 ppm Sr⁺² and 100 ppm Ba⁺²</u>					
E46D3856-1	1.65	2.69	16.0	18.8	53
-3	1.42	2.72	16.7	18.8	51
-5	1.83	4.00	16.3	18.1	61
-7	1.69	2.53	16.3	18.7	52
-9	1.68	5.53	16.7	18.7	43

differences in crystallographic orientation. The large-grained polycrystalline KCl samples of the IAF and IAG series behaved in a more conventional manner. Mean grain sizes ranged from 800 to 2000 μm and, consequently, no appreciable hardening or strengthening was expected. The measured values of hardness varied from 11 to 14 kg/mm^2 ; the yield strength of the 40 samples averaged 0.47 ksi and the average ultimate strength was 0.74 ksi. These strength and hardness values are typical of randomly oriented single crystal KCl.

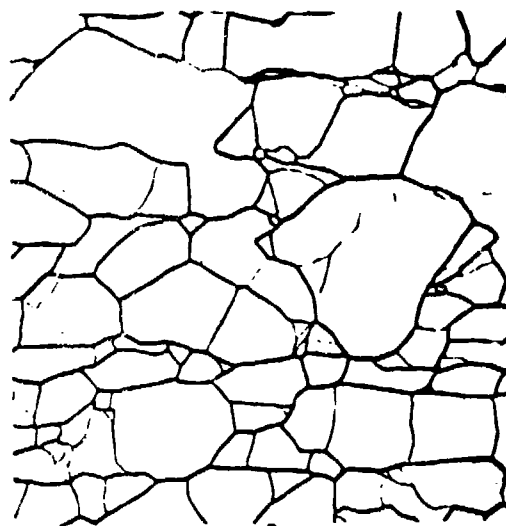
A group of hot extruded samples containing additions of Ba^{+2} , Sr^{+2} , or Eu^{+2} in concentrations ranging from 200 to 1000 ppm were also evaluated. These data are also summarized in Table 24. Three of the KCl alloys were hot forged after extrusion in an attempt to produce a finer grain structure than could be achieved by extrusion alone. Representative microstructure of these alloys are shown in Figures 53 through 56.

The 500 ppm additions of Eu^{+2} appeared to be the most effective of the divalent elements. As extruded, the yield strength of this alloy averaged 1.95 ksi with an average mean grain size of 47 μm . Two sets of hot forged KCl: Eu^{+2} were evaluated. With the first set of samples (E30D631XF20B), hot forging produced a modest decrease in the mean grain size (from 47 to 37 μm) and seemed to yield a more equiaxed microstructure. The average yield strength was increased to 2.40 ksi. A second set of hot forged specimens (AFML638) had a very elongated microstructure (Figure 54) with a mean grain size of 6.5 to 7.4 μm . Two of the five specimens in this group failed without yielding with ultimate strengths of 2.91 and 2.99 ksi. The average yield and ultimate strength of the other three samples was 3.50 and 5.17 ksi, respectively. The hardness of the KCl: Eu^{+2} specimens ranged from 13.5 to 20.5 kg/mm^2 (at a 50 gm load) and was apparently independent of the post-extrusion hot forging.



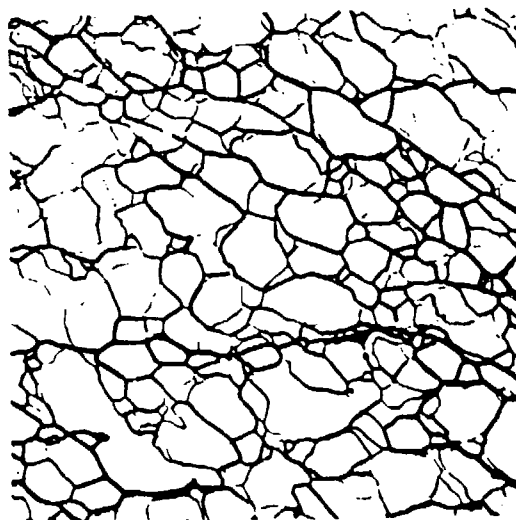
53A) 1000 ppm Ba⁺²
(E25D56-5)

250X



53B) 500 ppm Ba⁺²
(E42D56-5)

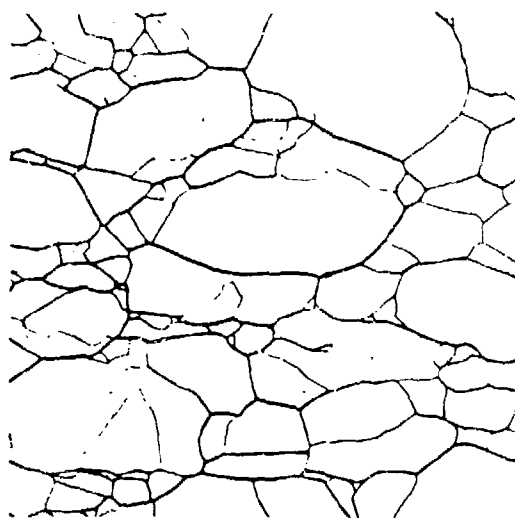
250X



53C) 500 ppm Ba⁺²
Hot Forged
(E42D561CXF50-1)

250X

Figure 53. Harshaw Hot Extruded KCl:Ba⁺².

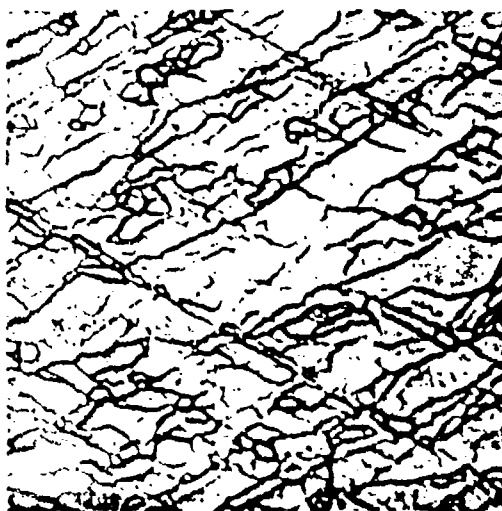


54A)
(E28063-9)

250X

54B) Hot Forged
(E30D63IXF 20B-4)

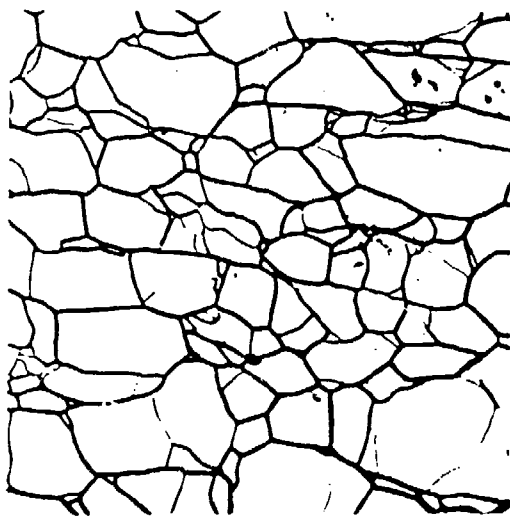
250X



54C) Hot Forged
(AFML 638-5)

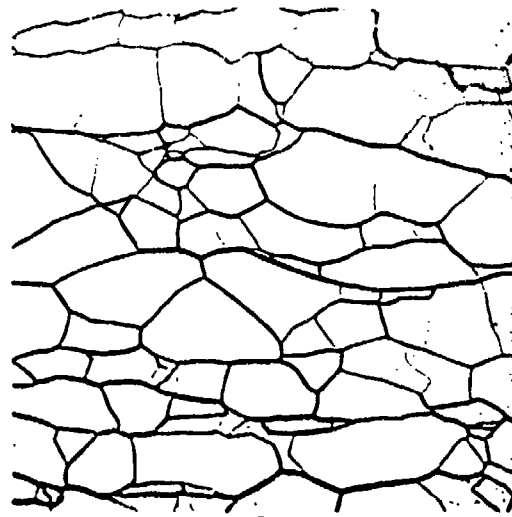
750X

Figure 54. Harshaw Hot Extruded KCl:500 ppm Eu^{+2} .



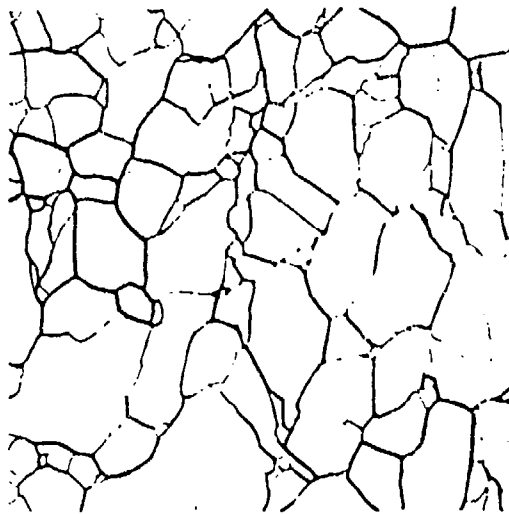
55A) 200 ppm Sr^{+2}
(E19D38-17)

250X



55B) 500 ppm Sr^{+2}
(E40D381-1)

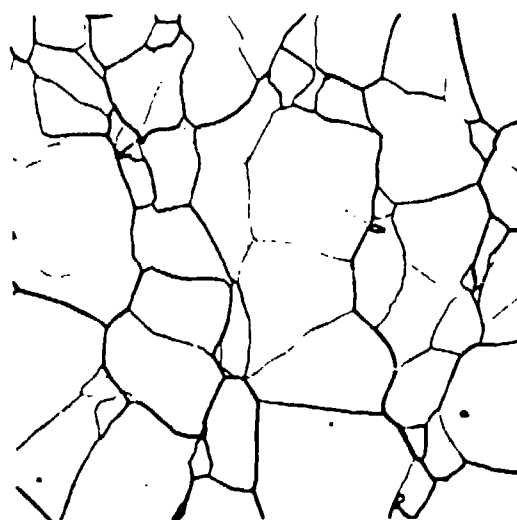
250X



55C) 500 ppm Sr^{+2}
Hot Forged
(E40D381BXF20-5)

250X

Figure 55. Harshaw Hot Extruded $\text{KCl}:\text{Sr}^{+2}$.



56A) 400 ppm Sr^{+2} + 100 ppm Ba^{+2} 250X
(E46D3856-5)



56B) 200 ppm Sr^{+2} 150X
Discontinuous Grain Growth
(E19038-18)

Figure 56. Harshaw Hot Extruded KCl.

The Sr^{+2} addition produced strengthening in proportion to the concentration of the additive. As the Sr^{+2} concentration was increased from 200 to 500 ppm, the average yield strength increased from 1.58 to 1.80 ksi despite an increase in the average mean grain size from 39 to 57 μm . The average yield strength of the 500 ppm Sr^{+2} material was increased to 2.30 ksi by hot forging. The average mean grain size of this forging (32 μm) remained relatively large, however.

The least effective additive was Ba^{+2} . A 500 ppm addition resulted in higher strengths than 1000 ppm of Ba^{+2} . Hot forging reduced the average mean grain size of this alloy from 32 to 21 μm and increased the average yield strength from 1.57 to 1.71 ksi.

The mixed system, containing 400 ppm of Sr^{+2} and 100 ppm Ba^{+2} , was evaluated in the "as extruded" condition. The combination of these additives produced strengthening approximately equivalent to that obtained with 500 ppm of Sr^{+2} , or by hot forging KCl + 500 ppm Ba^{+2} .

Discontinuous grain growth similar to that shown in Figure 56 was observed in a few specimens. In every instance, this occurred in a specimen in which one surface was part of the parent ingot surface. It is likely that this discontinuous grain growth was the consequence of the higher residual strain energy which would prevail near the ingot surface as the result of an extrusion deformation gradient due to die friction.

3.2.3 ManLabs KCl and KCl Alloys

A total of 80 specimens representing 28 hot forgings of 10 different KCl compositions were evaluated for flexural strength, Knoop hardness, and microstructural characteristics. These data are summarized in Table 25. Thermal expansion data were also obtained for three representative alloy compositions.

TABLE 25. TEST RESULTS FOR MANLABS KCl

Specimen No.	Strength		Knoop Hardness (kg/mm ²)		Mean Grain Size (μm)
	Yield	Ultimate	50 gm	100 gm	
<u>Unalloyed Potassium Chloride</u>					
198 BH-3A	1.87	3.16	13.2	11.6	15.0
-4B	none	1.48	8.8	15.3	---
-5	none	1.04	9.4	15.8	18.0
<u>Potassium Chloride +500 ppm Eu⁺²</u>					
159 BH-1	none	4.89	16.3	15.6	---
-2	none	3.28	17.8	15.9	---
-3	none	5.29	16.3	15.4	11.6
194 BH-7	2.36	3.19	14.0	13.5	25.0
-8	2.35	3.18	15.4	17.4	---
-9	2.74	3.12	15.3	15.6	---
-10	2.35	2.82	14.3	16.2	---
-11	2.22	2.78	14.1	13.5	38.7
<u>Potassium Chloride + 1 m/o Cesium Chloride</u>					
231 BH-1	3.10	4.16	---	---	---
-2	3.30	4.52	---	---	---
-3	3.56	4.55	16	18	23
<u>Potassium Chloride + 5 m/o Potassium Bromide</u>					
154 BO-1	3.72	5.53	16.9	16.2	---
-2	3.63	4.71	18.1	15.8	10.3
155 BU-4	2.93	4.35	15.9	15.8	15.7
200 BH-6	4.13	5.59	18.6	18.0	8.2
-7	4.42	6.58	16.3	17.3	---
212 BH-1	3.44	4.65	19.2	18.2	12.2
-1A	none	4.71	17.8	17.7	---
-5	4.44	5.47	20.2	22.5	10.3
-5A	4.67	6.18	22.4	21.9	7.9
213H-3A	2.55	3.37	15.8	15.4	15.4
-3B	2.72	4.11	---	---	---
-4	none	2.92	15.3	15.6	12.2

TABLE 25. TEST RESULTS FOR MANLABS KCl (continued)

Specimen No.	Strength		Knoop Hardness (kg/mm ²)		Mean Grain Size (μm)
	Yield	Ultimate	50 gm	100 gm	
<u>Potassium Chloride + 10 m/o Potassium Bromide</u>					
215BH-1	4.11	7.19	20	20	13.4
-2	5.19	6.33	---	---	---
-3	none	5.33	---	---	---
216H-1	4.74	6.52	17.2	17.5	15.7
-1A	4.88	6.99	20.4	22.8	---
-3	4.40	6.52	21.3	21.4	---
218H-1a	none	5.13	14.7	15.7	17.3
-2	5.33	7.29	19.3	18.0	10.0
-2B	none	5.92	---	---	---
<u>Potassium Chloride + 5 m/o Rubidium Chloride</u>					
202BH-1	none	4.17	14.9	16.2	9.1
-24	none	3.82	15.4	15.4	11.7
-26	none	3.91	---	---	---
203BH-6	none	4.46	17.8	18.8	---
-7a	4.19	5.73	17.1	16.2	10.4
-7	none	5.16	17.8	18.8	12.5
204BH-4	4.08	5.47	17.8	16.8	8.7
206BH-3	none	4.91	15.9	17.8	---
-3A	4.74	5.99	17.8	16.2	10.6
208BH-1	3.37	3.92	15.4	15.6	---
-2	3.50	4.51	16.4	16.2	14.3
-3	2.86	3.80	15.5	14.4	17.3
-3A	3.40	4.23	14.5	16.8	---
211H-1	3.67	5.79	17.3	17.8	10.6
-1A	3.45	5.36	17.5	16.8	---
-2	3.44	4.82	16.6	17.0	---
217BH-4	3.72	5.87	15.2	15.6	14.5
-5A	4.21	5.88	14.7	15.6	13.0
-5B	none	4.55	---	---	---
219BH-4	none	6.23	16.7	15.8	---
-5	none	6.36	17.8	18.8	9.6

TABLE 25. TEST RESULTS FOR MANLABS KCl (concluded)

Specimen No.	Strength		Knoop Hardness (kg/mm ²)		Mean Grain Size (μm)
	Yield	Ultimate	50 gm	100 gm	
<u>Potassium Chloride + 20 m/o Rubidium Chloride</u>					
229H-1	5.88	7.19	---	---	---
-2	5.78	6.88	21	20	---
-3	3.28	6.05	---	---	---
-4	5.02	6.86	---	---	---
<u>Potassium Chloride + 30% Rubidium Chloride</u>					
232BH-1	5.67	6.49			---
-2	6.16	7.21	---	---	---
-3	4.80	6.28	---	---	---
-4	4.65	6.58	18	20	---
<u>Potassium Chloride + 40 m/o Rubidium Chloride</u>					
224H-1	none	5.27	20	23	---
-2	none	6.72	---	---	---
-3	none	5.75	---	---	---
-4	none	3.84	---	---	---
234H-1	3.67	5.46	23	23	---
-2	3.19	5.14	---	---	---
<u>"Algloy" 33 m/o KCl-67 m/o KBr</u>					
175OP-a	4.24	5.42	20.9	22.8	24.5
-b	none	2.85	---	---	27.2
176OP-a	none	2.83	21.7	22.8	39
-b	none	4.28	---	---	---
-c	none	3.30	---	---	---
177OP-a	4.42	5.52	20.0	22.7	14
-b	4.41	5.48	---	---	---
-c	3.81	5.22	---	---	---
180OP-a	none	4.87	20.9	22.6	32
-b	4.51	5.26	---	---	27.2

The quality of the ManLabs specimens was relatively poor. Surface scratches and pits, edge pits, and surface fogging were quite prevalent. A number of specimens had poorly rounded or sharply beveled edges. Poor surface finish and the resultant presence of weakening flaws was probably responsible for the unusually large number of specimens which failed without yielding, some at relatively low levels of strength.

Most of the specimens measured 6 x 6 x 50 mm. Forging 159BH specimens were larger (6 x 12 x 50 mm) and the "Alqloy" specimens were 3 x 6 x 50 mm.

Only one of the hot forged, unalloyed KCl specimens exhibited a yield point. This specimen had a yield strength of 1.87 ksi and an ultimate strength of 3.16 ksi. The microstructure of this specimen (Figure 57) was equiaxed with a mean grain size of 15 μ m. The other two specimens with equivalent microstructures had ultimate strengths of 1.04 and 1.48 ksi. These low values would suggest flaw-initiated failure.

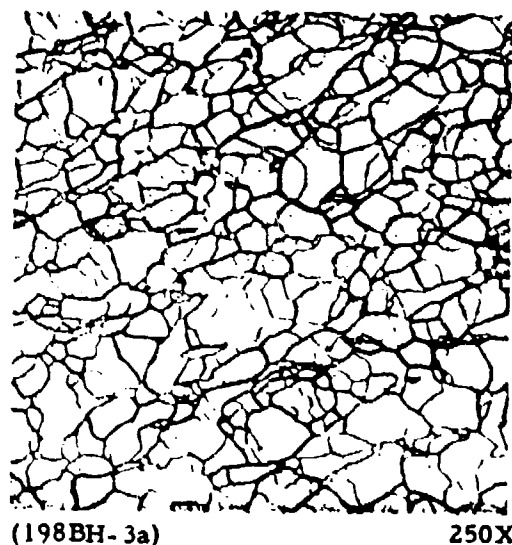


Figure 57. ManLabs Hot Forged Unalloyed KCl.

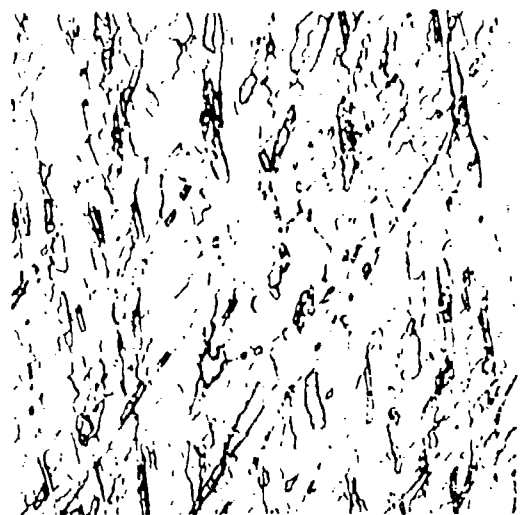
None of the KCl + 500 ppm Eu^{+2} specimens from Forging 159 displayed a yield point. However, the ultimate strengths of these specimens were quite consistent with the 12 μm mean grain size of this material. As is evident in Figure 58, the microstructure of this forging was very elongated. All six specimens of Forging 194BH (also a KCl + 500 ppm Eu^{+2} alloy) were ductile with an average yield strength of 2.40 ksi and an average ultimate strength of 3.02 ksi. The microstructure of two specimens selected at random from this group was equiaxed with mean grain sizes of 25 and 39 μm (Figure 59).

Ductile behavior was observed with KCl + 1 m/o CsCl. These samples averaged a yield strength of 3.32 ksi and an ultimate strength of 4.4 ksi. This alloy had an equiaxed microstructure (Figure 60) with a mean grain size of 23 μm .

Twelve specimens of KCl - 5 m/o KBr alloy from five different forgings had ultimate strengths ranging from 2.92 to 6.18 ksi. Only two of the twelve specimens failed without yielding; the remaining ten had yield strengths ranging from 2.55 to 4.67 ksi. The mean grain size of these specimens were equiaxed while others were very elongated. Typical photomicrographs of this alloy are shown in Figure 61.

Three of the nine specimens of KCl + 10 m/o KBr evaluated were brittle and all three exhibited ultimate strengths slightly lower than the six ductile specimens of this group. Yield strengths ranged from 4.11 to 5.33 ksi; ultimate strengths from 5.13 to 7.29 ksi. The mean grain size of this alloy ranged from 10 to 17.3 μm with a very elongated microstructure (see Figure 62).

A total of 21 specimens of KCl + 5 m/o RbCl from 8 different forgings were evaluated. Nine of these specimens failed without yielding, five of which had ultimate strengths below the average of the group. The yield strength of this alloy varied from 2.86 to 4.74 ksi with the ultimate strength



(159BH-3)

250X

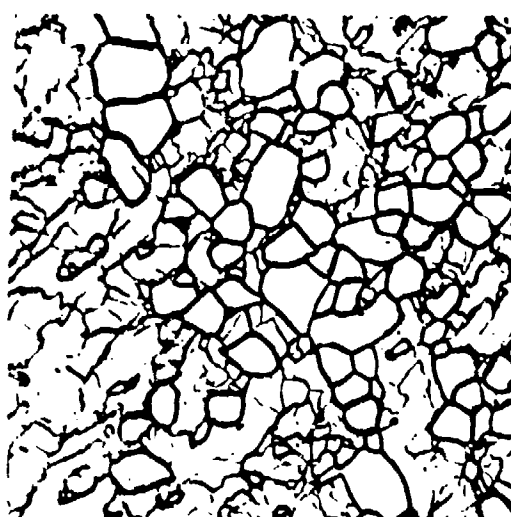
Figure 58. ManLabs Hot Forged KCl:500 ppm Eu^{+2} .



(194BH-7)

250X

Figure 59. ManLabs Hot Forged KCl:500 ppm Eu^{+2} .



(231BH-3)

250X

Figure 60. ManLabs Hot Forged KCl + 1 m/o CsCl.



26A) (212BH-1a)

250X



26B) (212BH-5a)

250X

Figure 61. ManLabs Hot Forged KCl + 5 m/o KBr.

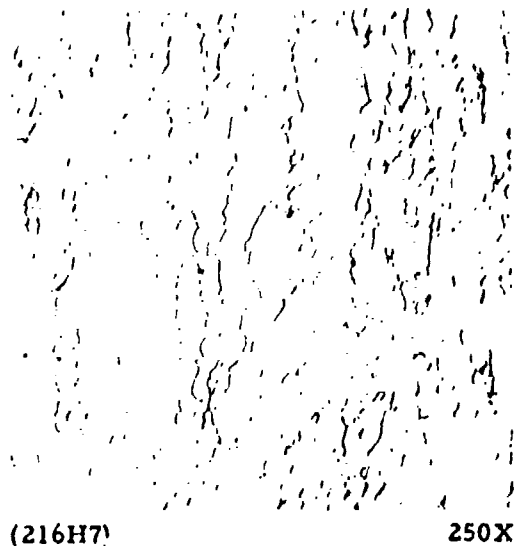


Figure 62. ManLabs Hot Forged 10 m/o KBr.

ranging from 3.82 to 6.36 ksi. The mean grain size varied from 9 to 17 μm . While most of the specimens had an equiaxed microstructure similar to that of Figure 63, several had very elongated grains (Figure 64).

Four specimens of KCl + 20 m/o RbCl were ductile and exhibited average yield and ultimate strengths of 4.99 and 6.75 ksi, respectively. A slightly higher yield strength (5.32 ksi) was obtained with four specimens of KCl + 30 m/o RbCl; but the ultimate strength of this alloy was slightly lower at 6.64 ksi. Brittle behavior was noted in all four specimens of a KCl + 40 m/o RbCl alloy from one forging (224H). The average ultimate strength of the alloy was 5.39 ksi. A second forging of KCl + 40 m/o RbCl was ductile; with average yield and ultimate strengths of 3.28 and 5.30 ksi, respectively.

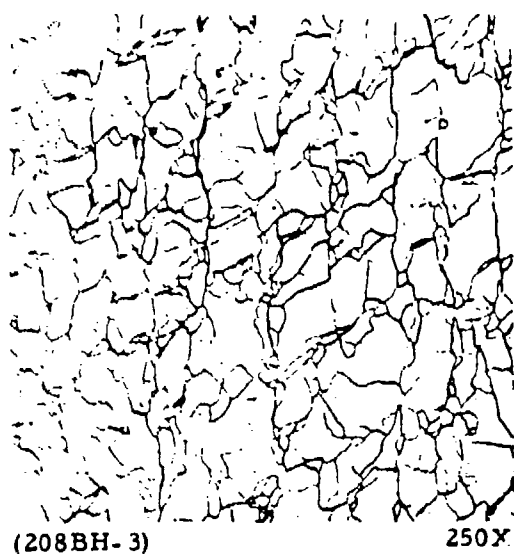


Figure 63. ManLabs Hot Forged
5 m/o RbCl.

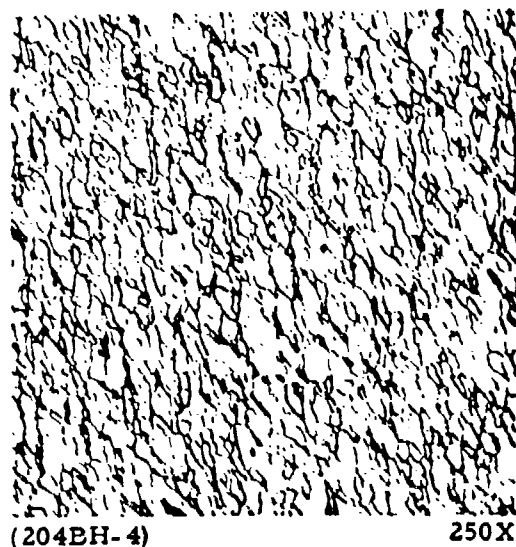


Figure 64. ManLabs Hot Forged
5 m/o RbCl.

Optical polished sections were not obtained for the 20, 30, and 40 m/o KBr alloys. The solubility of these was too high to obtain a legible, polished and etched surface despite repeated efforts with dilute water-alcohol and HCl etchants.

Ten specimens from 4 different forgings of "Alqloy", an alloy of 33 m/o KCl - 67 m/o KBr, were evaluated. Five of the specimens failed without yielding with ultimate strengths below the average of the other five specimens. The average yield strength of the ductile specimens was 4.28 ksi; the average ultimate strength was 5.38 ksi. These specimens had an equiaxed microstructure; mean grain sizes ranged from 14 to 39 μm with the majority being in the neighborhood of 27 μm , as is shown in Figure 65.

A hot forged polycrystalline disc of unalloyed KCl from ManLabs was submitted for flexural strength measurements. This disc was 6.0 mm thick and 23 cm in diameter. It had been laser-heated in a prior optical evaluation

and had formed a one-centimeter octagon-shaped crystal in the heated region. In the few weeks prior to reducing this disc to mechanical test specimens, several other octagons and a few square markings appeared both on the surface and within the bulk of the material. X-ray analyses revealed the octagon to be the (111) face of a cubic crystal. It was presumed that the squares were the (100) faces of other cubic crystals; both being the consequence of massive discontinuous grain growth occurring as a time-dependent response to residual press forging strain.

A group of 10 mechanical test bars, approximately $6.0 \times 6.0 \times 10$ mm, were machined from a large semicircular segment of the sample in a series of parallel cuts which spanned a 60-70 mm region extending radially from the original center of the sample towards one edge. The test bars were numbered sequentially and the carefully hand polished on all four sides to a scratch-free condition using methanol moistened jewelers rouge.

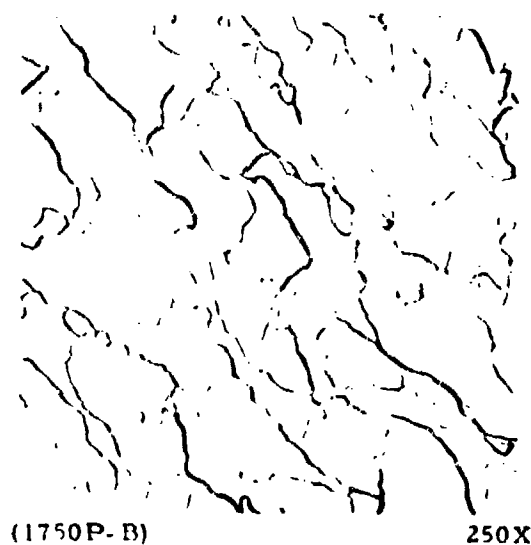


Figure 65. ManLabs Hot Forged "Alqloy".

All of the odd-numbered specimens were tested with their tension-compression surfaces parallel to the original window sample surface. The even-numbered specimens were rotated 90° , such that their tension-compression surfaces were perpendicular to the original window surface.

The results of these tests, which are summarized in Table 26, indicated a wide range of strengths for these specimens with no apparent dependence upon either radial location or orientation. The strength values were much lower than had been anticipated with this material which reportedly was very fine-grained (10 to 20 μm). Microscopy of these specimens revealed the cause of these unexpectedly low strengths. As illustrated in Figure 66, all ten specimens contained a fine-grained core sandwiched between regions of essentially single crystal material. The core had an average grain size of 12.6 μm and extended to the saw-cut surfaces of the specimens. This would indicate that the cutting and polishing procedures used in the preparation of mechanical test specimens were not responsible for the discontinuous grain growth.

It would appear that during the time interval between fabrication of the window sample and the measurements of mechanical strength, discontinuous grain growth initiated at the surfaces of the sample and proceeded inward. Initial evidence of this phenomenon was the appearance of massive (100) and (111) crystal facets shortly after optical absorption measurements were conducted. Low flexural strengths were inevitable since the test bars were subjected to maximum bending stresses in essentially single crystal regions.

Thermal expansion coefficients were measured for three representative ManLabs KCl alloys; KCl:Eu^{+2} , KCl:KBr , and KCl:RbCl . These data are summarized in Table 27 and are presented as the average value and standard deviation of several measurements over each of two temperature ranges; -65°C to 25°C and $+20^{\circ}\text{C}$ to $+100^{\circ}\text{C}$.

TABLE 26. TEST RESULTS FOR MANLABS KCl PRESS FORGED DISC

Sample Number	Strength (ksi)		Hardness (kg/mm ²)		Mean Grain Size (μm)
	Yield	Ultimate	50 gm	100 gm	
Press Forged					
Disk-1	0.69	1.27	13.9	13.6	**
-2	0.97	1.38	13.2	11.6	+
-3*	0.57	0.92	12.7	11.5	**
-4*	0.64	0.87	14.0	11.5	+
-5	0.83	1.00	13.3	13.2	12.6++ **
-6	1.44	1.63	17.2	18.8	+
-7	none	0.72	13.7	13.3	**
-8	0.60	1.28	12.7	11.6	+
-9*	0.59	0.91	17.0	18.6	**
-10	0.86	1.81	13.8	14.4	+

* Edge damaged in polishing.

** Parallel to original surface.

+ Perpendicular to original surface.

++ Typical grain size in polycrystalline region. Extensive discontinuous grain growth extending from the original surface noted on all of these samples.

TABLE 27. COEFFICIENT OF THERMAL EXPANSION OF VARIOUS MANLABS KCl ALLOYS

Alloy	Sample No.	Avg. Coef. of Ther. Exp. cm/cm°C × 10 ⁻⁶	
		(-65°C to +25°C)	(+20° to +100°C)
KCl:500 ppm Eu ⁺²	194BH-9	33.9 ± 1.4	34.6 ± 0.5
	194BH-8	---	34.2 ± 0.5
KCl + 5 m/o RbCl	203BH-6	33.5 ± 1.0	35.0 ± 0.3
	208BH-2	---	33.6 n.d.*
KCl + 5 m/o KBr	212BH-1	34.2 ± 0.9	34.8 ± 0.8
	212BH-5	---	34.8 ± 0.6
	200H-7	---	35.0 ± 0.5

* n. d. = not determined.

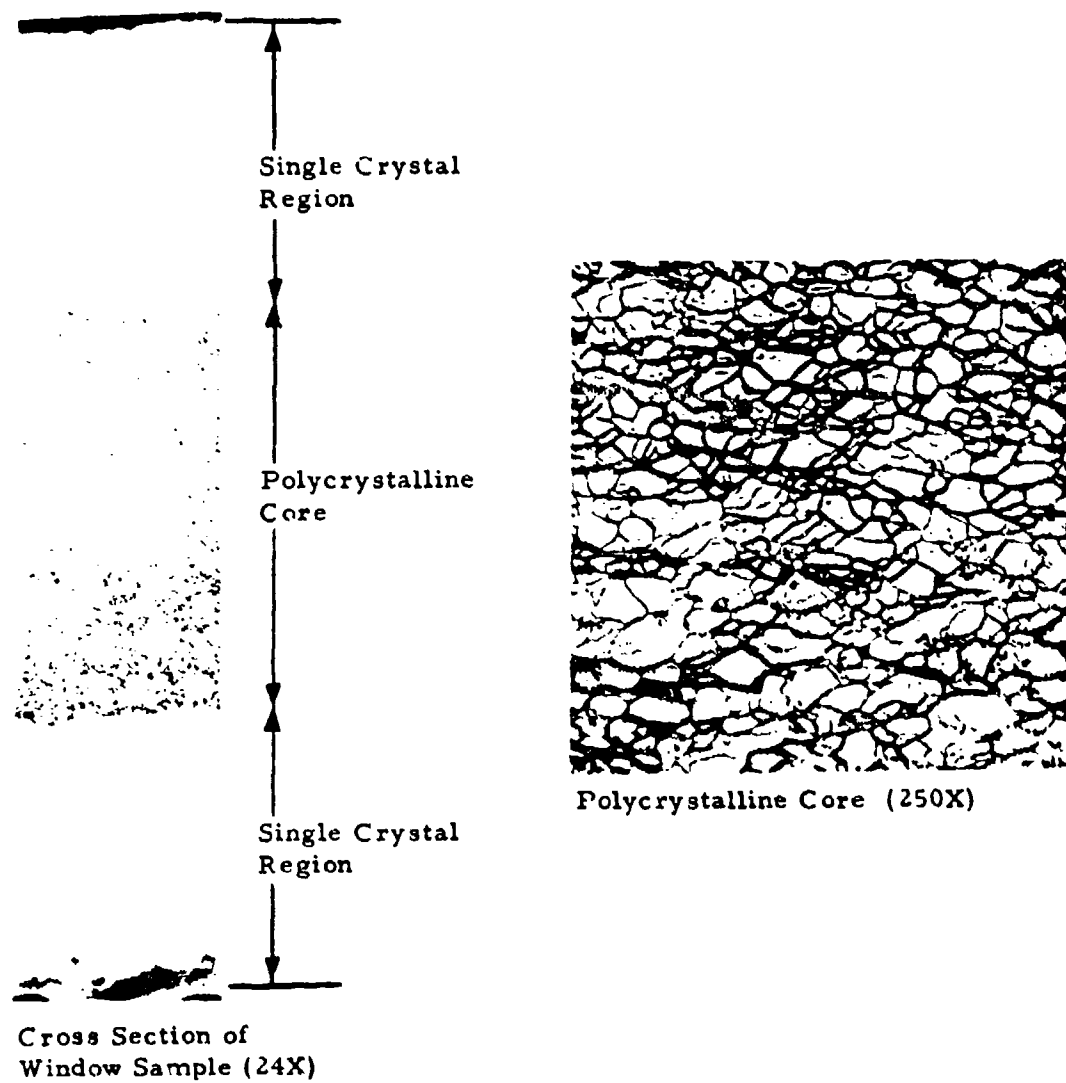


Figure 66. Representative Microstructure of ManLabs Hot Forged KCl.

There was no perceptible difference among the three alloys with respect to their coefficients of thermal expansion. This is consistent with the results obtained with several Honeywell KCl alloys. The low temperature measurements were less precise than those obtained in the 25°C to 100°C range. Pooling the measurements at -65°C to +25°C for the three alloys yielded an average expansion coefficient of $33.9 \times 10^{-6} \text{ cm/cm}^\circ\text{C} \pm 4\%$, whereas, in the higher temperature range, the average was $34.6 \times 10^{-6} \text{ cm/cm}^\circ\text{C} \pm 1\%$. A "Student t" test comparison of the two averages revealed that the slight difference was statistically significant. This had been anticipated since the expansion coefficient of KCl is known to vary directly with temperature.

3.2.4 Hughes Alkali Halides

Two specimens of "single crystal" KCl and one specimen of "single crystal" NaCl produced by Hughes using a Bridgeman process were evaluated. As is evident from the test results of Table 28, all three specimens exhibited strengths and hardness values typical of those observed with single crystal material. The specimens were actually polycrystalline with mean grain sizes greater than 2500 μm (Figure 67). Little, if any, strengthening by polygonization would have been expected for these specimens and, in fact, none was observed.

3.2.5 Isomet KCl

Two samples of single crystal KCl from Isomet were submitted for flexural strength measurements. These samples measured approximately $0.64 \times 0.95 \times 5.1 \text{ cm}$ and were polished only on the $0.95 \times 5.1 \text{ cm}$ faces. Both samples were tested such that the maximum tensile stresses were developed on a polished surface.

Each specimen failed in the central region where a constant bending moment is developed at ultimate strengths of 0.94 and 0.76 ksi. Laue x-ray patterns of the fracture surface revealed the four-fold symmetry of

TABLE 28. TEST RESULTS FOR HUGHES ALKALI HALIDES

Sample No.	Strength (ksi)		Hardness (kg/n.m ²)		Mean Grain Size μm
	Yield	Ultimate	50 gm	100 gm	
<u>Potassium Chloride</u>					
KCl-B19L3 Outer D	0.46	1.60	10.3	8.9	~2500
KCl-B19L3 Outer B	0.58	1.77	10.0	9.3	~2500
<u>Sodium Chloride</u>					
NaCl B20-3-B	0.90	1.40	24.2	22.4	~2500

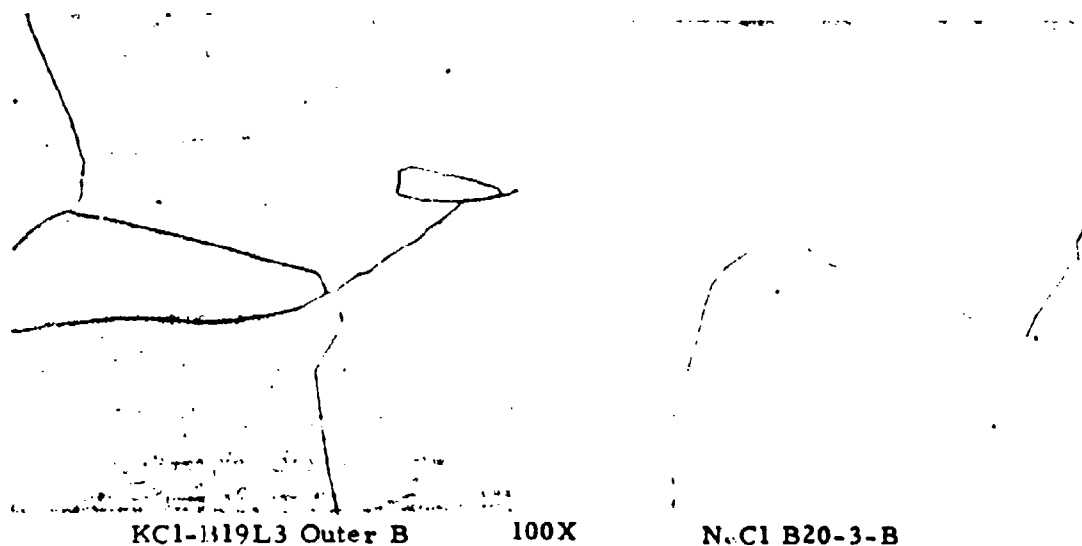


Figure 67. Representative Microstructure of Hughes Polycrystalline KCl and NaCl.

the 100 cleavage plane of KCl. Laue patterns of the four sides of the samples were complex and asymmetrical indicating that the sides of these specimens had not been cut with any special crystallographic orientation. The x-ray patterns of the unpolished sides also contained a pronounced diffraction ring indicating the presence of a polycrystalline deposit on these surfaces. Such deposits usually form when moisture is allowed to evaporate slowly on the surface with a resultant deposition of KCl as a polycrystalline precipitate. This precipitate can have a detrimental effect upon the strength of KCl by providing an egress for dislocations at the interface between the precipitate and the single crystal. These emerging dislocations will tend to coalesce into Griffith-type microcracks which will propagate catastrophically when stressed above a critical level.

It is not known if the polycrystalline layer had an adverse effect upon the strength of the Isomet samples. The observed failure stresses were of the general magnitude observed with single crystal KCl.

3.2.6 Summary

The strength of alkali halides can be significantly increased by hot working processes which lead to the formation of a fine-grained, polycrystalline microstructure. Alloying additions also produced strengthening as evidenced by a 2-3 fold increase in the yield strength of single crystal alloys. Presumably, alloy strengthening was operative in the hot worked alloys as well. The primary benefit of alloying, however, may be the microstructural stabilization provided by the additions. A number of unalloyed KCl specimens from Honeywell experienced extensive discontinuous grain growth, apparently as a consequence of the mild mechanical working associated with the preparation of optical microscopy specimens. Spontaneous discontinuous grain growth was observed in a press forged sample of unalloyed KCl from ManLabs. In contrast, only one alloy system (5 m/o and 10 m/o RbCl) exhibited any tendency towards discontinuous grain growth and this was

confined to a single specimen of each alloy. All other alloys maintained their "as-forged" microstructure throughout their evaluation.

The monovalent alloying additions, Rb, Cs, and Br, were expected to form continuous solid solutions with KCl because of the similarity of ionic radii. This was confirmed by the x-ray diffraction measurements of precision lattice constants which displayed nearly ideal Vegard's law behavior. It would be reasonable to assume that the strengthening observed in RbCl, CsCl, and KBr modified KCl specimens was achieved by strain due to the slight size mismatch of solute atoms incorporated substitutionally on the KCl lattice.

One penalty associated with RbCl and KBr strengthening is a significant decrease of thermal conductivity. For example, 5 m/o additions of either compound produced more than a two-fold decrease of thermal conductivity.

Divalent additions, in particular Eu^{+2} , produced effective strengthening, at alloying levels of only 500 ppm. While not fully understood, it is presumed that strengthening arises either from lattice rearrangement and the formation of K^+ vacancies to compensate for substitutionally incorporated Eu^{+2} or by the formation of very fine arrays of EuCl_2 precipitates. Since the relative concentration of Eu^{+2} is low in these alloys, there was no measurable change in their thermal conductivity.

Considerable variations in strength were noted, both among specimen groups of the same nominal composition and among specimens taken from a common forging. These variations could be due to extrinsic flaws in the specimens, subtle variations in alloy compositions, or processing variations from forging to forging. The available test data are insufficient to isolate and analyze each of these factors. However, it must be recognized that the basic objective of this evaluation program was to evaluate promising candidate window materials and not necessarily to identify optimum processing

parameters. Table 29 is a compilation of the highest strengths observed with most of the alloy systems evaluated. While these data may not be optimum values, they do represent what can, and has, been achieved. Data such as these are difficult to compare because of differences in both alloy composition and microstructure. If it can be assumed that the alkali halide alloys exhibit Petch-type behavior, then strength data can be normalized with respect to microstructure and the effect of alloying additions can be separately analyzed. The Petch equation is given by

$$\sigma_y = kG^{-1/2} + \sigma_0 \quad (28)$$

where σ_y is the polycrystalline yield strength, σ_0 is the single crystal yield strength, G is the mean grain size, and k is the Petch constant. Alloying additions will affect both k and σ_0 , whereas, strengthening achieved by grain boundary resistance to slip is related to the magnitude of the term $kG^{-1/2}$.

Single crystal yield strength data were obtained from Honeywell* for most of their alkali halide forgings. These data, in conjunction with the values of polycrystalline yield strength and mean grain size obtained by UDRI, were used to calculate values of the Petch constant for several of the Honeywell alloys as summarized in Table 30.

The Petch constant obtained for unalloyed KCl (45.6 psi $\sqrt{\text{in}}$) was in excellent agreement with the value of 44 psi $\sqrt{\text{in}}$ obtained by Becker and Rice.⁽¹⁷⁾ The Petch constants for the KCl alloys were larger, varying from 50.3 to 63.7 psi $\sqrt{\text{in}}$ with relatively large standard deviations.

* Private communication with J. R. Fenter, AFML, Wright-Patterson Air Force Base, Ohio.

(17) P. R. Becker and R. W. Rice, "High Energy Laser Windows," Section 3, Mechanical Properties, Semiannual Report No. 2, ARPA Order 2031, Naval Research Laboratory, 30 June 1973.

TABLE 29. HIGHEST STRENGTHS OBSERVED FOR EACH ALKALI
HALIDE COMPOSITION EVALUATED

Alloy	Strength (ksi)		Knoop Hardness (kg/mm ²) 50 gm load	Mean Grain Size (μm)
	Yield	Ultimate		
Unalloyed KCl (Honeywell KCO75-513-1M)	4.69	6.55	17.8	4*
KCl + 500 ppm Eu ⁺² (Honeywell KCO5EuH27-1B-3-5M)	5.99	10.3	17.8	4.4
KCl+5 m/o KBr (Honeywell KC5KBO-31-4C3S-1M)	5.47	7.29	16.9	7.0
KCl+10 m/o KBr (ManLabs 212H-2)	5.33	7.29	19.3	10
KCl+5 m/o RbCl (Honeywell KC5RCH3C-1B-3S-1M)	5.77	7.71	16.3	6.9
KCl+10 m/o RbCl (Honeywell KC10RCO(86)-2M)	5.93	7.22	21.3	8.2
KCl+20 m/o RbCl (ManLabs 229H-1)	5.88	7.19	21	--
KCl+40 m/o RbCl (ManLabs 234H-1)	3.67	5.46	23	--
Alqloy:33 m/o KCl-67 m/o KBr (ManLabs 180OP-6)	4.51	5.26	21	27
KCl+1 m/o CsCl (Honeywell KC1CCH26-1B-2-2M)	4.34	5.42	17.8	11.3
Unalloyed NaCl (Honeywell NCH26-1K-8M)	6.60	10.18	37.9	7.3
NaCl+10 m/o NaBr (Honeywell NC10NBO33K-1-3M)	5.07	6.01	44.4	48
Unalloyed KBr (Honeywell KBO5-1B-2M)	3.21	4.58	14.3	9.5

* Honeywell data.

The Petch constants of the KCl alloys were statistically compared with that of unalloyed KCl using the "Student t" test. The higher values of the Eu^{+2} doped KCl, the 5 m/o KBr alloy, and the 1 m/o CsCl alloy were significant at a confidence level greater than 95%. The variability of the Petch constants for the other alloys was too large to conclude that alloying had produced an increase.

It would appear, therefore, that some (and perhaps all) alloying additions which elevate the single crystal yield strength of an alkali halide also enhance the strengthening effect of polygonization.

TABLE 30. PETCH CONSTANTS FOR THE ALKALI HALIDES

Alloy	Petch Constant ($\text{psi}\sqrt{\text{in}}$)			Number of Specimens
	Mean	Std. Deviation	COV*	
Unalloyed KCl	45.6	11.1	0.243	19
KCl + 500 ppm Eu^{+2}	54.7	0.8	0.015	2
KCl + 5 m/o KBr	57.6	16.7	0.294	17
KCl + 5 m/o RbCl	56.5	27.1	0.480	15
KCl + 10 m/o RbCl	50.1	14.6	0.290	2
KCl + 1 m/o CsCl	63.7	0.9	0.014	2
Unalloyed KBr	38.6	9.4	0.243	9
Unalloyed NaCl	59.0	7.8	0.133	15
NaCl + 10 m/o NaBr	48.9	---	---	1

* COV = Coefficient of Variation = Standard Deviation \div Mean.

LIST OF REFERENCES

1. W. J. Parker, et al., "Flash Method of Determining Thermal Diffusivity, Heat Capacity, and Thermal Conductivity," J. Appl. Phys., 32 (9) 1679-1687 (1961).
2. W. S. Carslaw and J. C. Jaeger, Condition of Heat in Solids, 2nd Edition, Oxford Press, New York, N. Y., 1959.
3. R. C. Heckman, "Finite Pulse-Time and Heat-Loss Effects in Pulse Thermal Diffusivity Measurements," J. Appl. Phys., 44 (4) 1455-1460 (1973).
4. Thermophysical Properties Research Center Data Book, Purdue University.
5. M. R. Lorentz, et al., "Some Properties of a Double Acceptor Center in CdTe," Phys. Rev. 134, p. 751 (1961).
6. M. Aven and B. Segall, "Carrier Mobility and Shallow Impurity States in ZnSe and ZnTe," Phys. Rev. 130, p. 21 (1963).
7. R. C. Eden and W. H. Zakrzewski, "Semi-Automatic Hall Effect Measurement System," RSI 41, p. 1030, 1970.
8. V. V. Zhdanova and V. P. Sergeev, "Thermal Expansion of ZnSe in the Temperature Range 100-600°K," Soviet Physics-Solid State, Vol. 14, No. 7, January 1973.
9. F. A. Horrigan and R. I. Rudco, "Materials for High Power CO₂ Lasers," Raytheon Company Final Report on Contract DA-AH01-69-C-0038, Sept. 1969.
10. N. A. Weil and I. M. Daniel, "Analysis of Fracture Probabilities in Nonuniformly Stressed Brittle Materials," J. Am. Cer. Soc., 47 (6) 268, June 1964.
11. L. H. Harter and A. H. Moore, "Maximum Likelihood Estimation of the Parameters of Gamma and Weibull Populations from Complete and Censored Samples," Technometrics (7) 639-643 (1965).
12. R. J. Roark, Formulas for Stress and Strain, 3rd Ed., McGraw-Hill, New York, N. Y., 1954.

13. F. A. Horrigan and R. I. Rudco, "Materials for High Power CO₂ Lasers," Raytheon Company Final Report on Contract DA-AH01-69, C-0038, September 1969.
14. Herbert F. Matari, Defect Electronics in Semiconductors, Wiley-Interscience, New York, 1971.
15. A. Eucken and G. Kuhn, "Ergebnissen neuer Messingen der Warmeleitfähigkeit fester krystallisier Stoffe bei 0° und -190° C," Z. Physical Chem., 134, Feb. 26, 1928.
16. W. B. Harrison, et al., "Halide Material Processing for High Power Infrared Laser Windows," Interim Technical Report 2, Contract F33615-72-C-2019, Honeywell, Inc., February 1973.
17. P. R. Becker and R. W. Rice, "High Energy Laser Windows," Section 3, Mechanical Properties, Semiannual Report No. 2, ARPA Order 2031, Naval Research Laboratory, 30 June 1973.